Master Thesis

The Influence of Leaflet Hemodynamics and Stress on Calcification in Modern Biological Aortic Valves: A Fluid-Structural Interaction Simulation Study

carried out for the purpose of obtaining the degree of Diplom-Ingenieur (Dipl.-Ing. or DI), submitted at TU Wien, Faculty of Biomedical Engineering, by

Amir Davood Elmi

Mat.Nr.: 1576069

under the supervision of

Ao.Univ.Prof. Dipl.-Ing. Dr.techn. Heinrich Schima
and Dr.scient.med. Mojgan Ghodrati-Misek, MSc
Center for Medical Physics and Biomedical Engineering, Medical University of
Vienna, AKH 4L
Ludwig Boltzmann Institute for Cardiovascular Research, Vienna

Vienna, November 2023

Contents

List of Tables

List of Figures

Zusammenfassung

Eine chirurgische bioprothetische Herzklappe wird aus biologischem Gewebe hergestellt, das üblicherweise von Tieren wie Rindern oder Schweinen stammt. Trotz der Vorteile, die Bioprothesen bieten, ist ihr bemerkenswerter Nachteil die kürzere Lebensdauer im Vergleich zu mechanischen Klappen. Diese verringerte Lebensdauer ist in erster Linie auf eine strukturelle Verschlechterung der Klappe zurückzuführen, die hauptsächlich durch Probleme wie Verkalkung, Abnutzung der Klappensegel und andere damit zusammenhängende Faktoren verursacht wird. Diese oben genannten Herausforderungen tragen zu Klappenfehlfunktionen bei und machen es erforderlich, dass sich die Patienten anschließenden Operationen zum Klappenersatz unterziehen.

Faktoren, die die Degeneration der Klappe beeinflussen, einschließlich Verkalkung und Abnutzung der Klappensegel, können auf eine erhöhte Belastung der Klappensegel in Verbindung mit der Hämodynamik der Klappe zurückzuführen sein. Ein umfassendes Verständnis der Funktion der Klappe und entscheidender Parameter wie der Spannungsverteilung auf den Klappensegeln kann durch eine Zwei-Wege-Analyse der Fluid-Struktur-Interaktion erreicht werden. Zur Durchführung dieser Simulation wurde das robuste Softwarepaket ANSYS verwendet. ANSYS nutzt ausgefeilte numerische Techniken und Algorithmen, um ein breites Spektrum technischer Probleme zu bewältigen. In dieser Forschung wurde ein Mikro-CT-Scan einer chirurgisch implantierten bioprothetischen Aortenklappe eingesetzt, um genaue Darstellungen der Segel und des Stents der Klappe zu erstellen. Um die Präzision zu erhöhen, wurden eine modifizierte Aortenwurzel und eine aufsteigende Aorta entworfen, um den Auswirkungen der bogenförmigen Geometrie der aufsteigenden Aorta Rechnung zu tragen. Die Studie zielte darauf ab, Schlüsselparameter zu bewerten, darunter Blutströmungsmuster in den Nebenhöhlen und Wandscherspannungen in den Segeln und der aufsteigenden Aorta. Die mechanischen Eigenschaften der Blättchen wurden durch eine Analyse der Hauptspannungs und Dehnungsverteilung untersucht. Von entscheidender Bedeutung für Ärzte ist die Berechnung der effektiven Öffnungsfläche, die Einblicke in die Klappenleistung bietet.

Die Simulationsergebnisse deuten auf eine erhöhte mechanische Belastung in Regionen in der Nähe des Stents und im zentralen Bereich des Segels hin. Darüber hinaus wurden an den linken und rechten Koronarhöckern relativ höhere Wandschubspannungswerte beobachtet als an den nicht-koronaren Höckern, obwohl letztere nahezu vernachlässigbar waren. Bemerkenswerterweise zeigten die Stromlinienmuster des Blutflusses aufgrund der bogenförmigen Geometrie der Aorta eine gewisse Asymmetrie, obwohl diese Unterschiede nicht signifikant waren. Diese Krümmung der Aorta hat einen erheblichen Einfluss auf den stromabwärtigen Blutfluss von der Klappe, beeinflusst die Hämodynamik der Klappe jedoch nur geringfügig. Es ist erwähnenswert, dass die meisten früheren Studien, die sich mit der Hämodynamik von Klappen befassten, die aufsteigende Aorta in ihren Modellen oft weglließen oder von einer einfachen zylindrischen Form ausgingen. Darüber hinaus ist anzuerkennen, dass Koronararterien in dieser Studie nicht berücksichtigt wurden, auch wenn sie möglicherweise einen Einfluss auf die Ergebnisse haben können. Daher empfehlen wir auch, die Koronararterien in zukünftige Forschungsbemühungen einzubeziehen.

Abstract

A surgical bioprosthetic heart valve is crafted from biological tissue, commonly sourced from animals such as bovine or porcine. Despite the advantages offered by bioprostheses, their notable drawback is a shorter lifespan compared to mechanical valves. This reduced longevity primarily stems from structural valve deterioration, predominantly caused by issues such as calcification, wear and tear of the leaflets, and other related factors. These aforementioned challenges contribute to valve malfunction, necessitating patients to undergo subsequent surgeries for valve replacement.

Factors influencing valve degeneration, including calcification, leaflet wear and tear, may originate from heightened stress on the leaflets, coupled with valve hemodynamics. A comprehensive understanding of the valve's functioning and crucial parameters like stress distribution on the leaflets can be achieved through a two-way Fluid-Structure Interaction analysis. To conduct this simulation, the robust software package ANSYS was utilized. ANSYS employs sophisticated numerical techniques and algorithms to tackle a wide spectrum of engineering predicaments.

In this research, a μCT scan of a surgically implanted aortic bioprosthetic valve was employed to generate accurate representations of the valve's leaflets and stent. To enhance precision, a modified aortic root and ascending aorta were designed to account for the impact of the arc-shaped geometry of the ascending aorta. The study aimed to evaluate key parameters, including blood streamline patterns across the sinuses and wall shear stress over the leaflets and ascending aorta. Mechanical attributes of the leaflets were investigated through an analysis of principal stress and strain distribution. Of critical significance to medical practitioners, the effective orifice area was calculated, offering insights into valve performance.

The simulation results indicate increased mechanical stress in regions near the stent and the leaflet's central area. Additionally, there were relatively higher wall shear stress values observed over the left and right coronary cusps compared to the non-coronary cusp, although the latter was nearly negligible. Notably, the streamline patterns of blood flow displayed some asymmetry due to the aorta's arc-shaped geometry, although these differences were not significant. This curvature of the aorta has a notable influence on the downstream blood flow from the valve, although it only marginally affects valve hemodynamics. It's worth noting that most of previous studies addressing valve hemodynamics often omitted the ascending aorta from their models or assumed it to be a simple cylindrical shape. Furthermore, it's worth acknowledging that coronary arteries were not accounted for in this study, even though they can potentially impact the outcomes. Therefore, we also recommend including coronary arteries in future research efforts.

Chapter 1

Introduction and Literature Review

1.1   Anatomy of heart

The heart, which is responsible for pumping blood throughout the body, is a vital component of the circulatory system. It is composed of four chambers, consisting of two upper chambers, called atria, and two lower chambers, called ventricles. Each chamber is equipped with a valve, as shown in Fig. 1.1, that allows blood to flow out while preventing backward flow. The valves consist of cusps located at each end of the two ventricles, acting as one-way inlets and outlets for blood flow (Khalique et al., 2019). Normal valves typically have three cusps, with the exception of the mitral valve, which has two. The four heart valves are as follows:

- **Tricuspid valve:** located between the right atrium and the right ventricle

- **Pulmonary valve:** located between the right ventricle and the pulmonary artery

- **Mitral valve:** located between the left atrium and the left ventricle

- **Aortic valve:** located between the left ventricle and the aorta
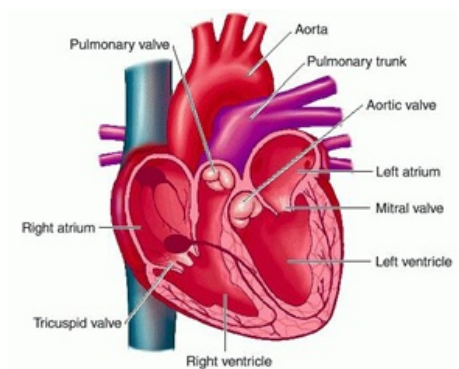
Figure 1.1: *Illustration of heart valves*

1.2 Cardiac Cycle

The heart's cyclic activity, known as the cardiac cycle, involves a sequence of pressure fluctuations (Galvez-Pol et al., 2020). These pressure changes cause blood to move through various heart chambers and the entire body. Electrochemical changes within the myocardium trigger the concentric contraction of cardiac muscles, resulting in pressure changes. Blood flow is directed by valves within the heart, which systematically propel blood to the next chamber. These rhythmic pressure and volume changes are graphically represented by Wiggers diagram (Fig. 1.2) or venous pressure tracings. The cardiac cycle comprises two primary phases: diastole and systole.
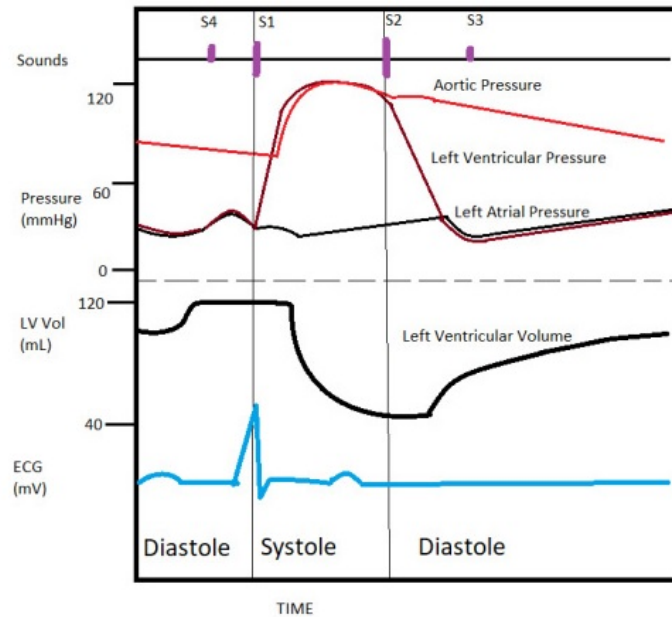
Figure 1.2: *Wiggers Diagram including ECG/EKG, Ventricular pressure, Ventricular Volume, Heart Sounds*

1.2.1 Diastole

The diastole is a phase in which the ventricles of the heart are relaxed and not contracting. During this period, blood flows passively from the left and right atrium to the left and right ventricle, respectively. This flow occurs through the atrioventricular valves (mitral and tricuspid), which act as a barrier between the atria and ventricles. The right atrium receives deoxygenated blood from the body via the superior and inferior vena cava, while the left atrium receives oxygenated blood from the lungs via the four pulmonary veins that enter the left atrium. At the end of diastole, the atria contract, propelling additional blood into the ventricles (Poterucha and Maurer, 2022).

1.2.2 Systole

Systole is the period when the left and right ventricles contract to push blood into the aorta and pulmonary artery respectively. This process is facilitated by the opening of the aortic and pulmonic valves during systole. The atrioventricular valves, on the other hand, remain closed during systole,

so no blood flows into the ventricles. Nevertheless, blood continues to enter the atria through the vena cava and pulmonary veins as usual (Wright et al., 2020).

1.3   The Aorta

With a diameter of 2-3 cm, the aorta is the biggest artery in the body (as shown in Fig. 1.3). It originates from the left ventricle of the heart and includes the aortic valve at its base. The aorta is categorized into two regions: the thoracic aorta and abdominal aorta. The upper portion of the thoracic aorta is further divided into two parts: the ascending aorta and the aortic arch.
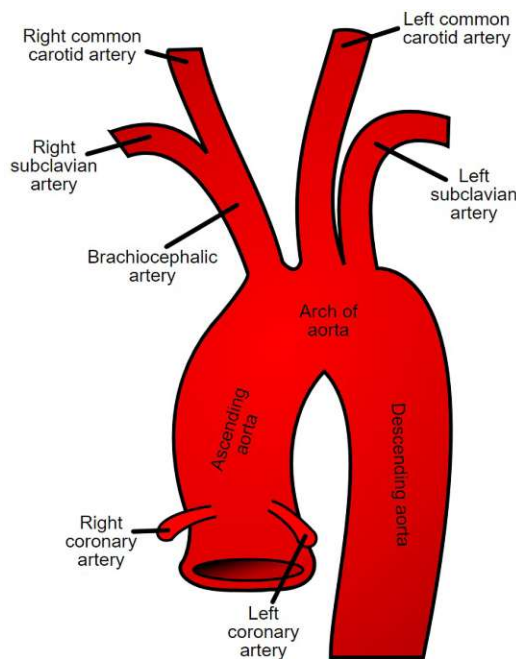
Figure 1.3: *Aortic root and Aorta*

1.4   Aortic Root

The aortic root is located between the left ventricular outflow tract (LVOT) and the ascending aorta (Fig. 1.4). The aortic root (AR) is commonly described in relation to the AV. The AR is made up of several anatomical components, including the annulus, interleaflet triangles, sinus of Valsalva, sinutubular junction, and leaflets.

1.4.1   Annulus

The annulus is a fibrous ring-shaped structure located at the aortic orifice and serves as a transition point between the left ventricle and aortic root. It acts as an anchor point for the valves (Anderson et al., 1991).
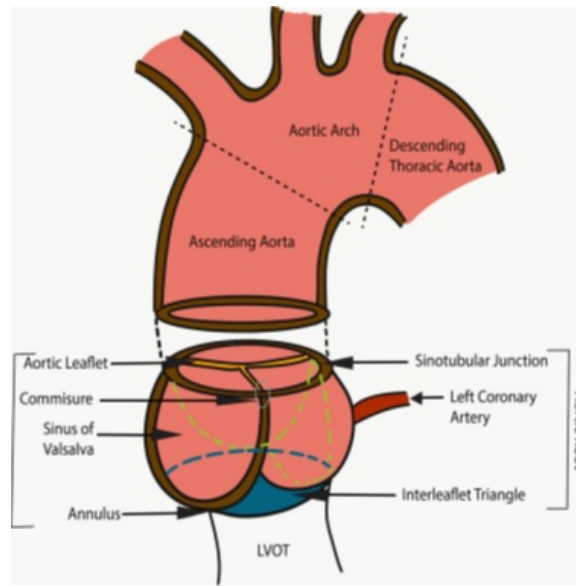
Figure 1.4: *Anatomy of aortic root (Nagpal et al., 2020)*

1.4.2 Interleaflet Fibrous Triangles

The interleaflet fibrous triangles located between the bases of the sinuses and are connected to the left ventricular wall (Dembistky et al., 2017). These triangles are positioned between the left ventricular cavity and the extra cardiac space. In contrast to the hinge-lines and sinus walls, interleaflet triangles have a lower concentration of collagen (Sutton et al., 1995)

1.4.3 Sinus of Valsalva

The sinus of Valsalva[1], also referred to as aortic sinuses, is a dilation of the ascending aorta located above the aortic valve. It comprises three sinuses, with one being anterior and the other two being posterior. The majority of the aortic wall is made up of these sinuses, with two coronary sinuses at the base of the ventricular musculature and a fibrous piece at the base of the non-coronary sinus (Choo et al., 1999).

1.4.4 Commissures

The point where the aortic leaflets are attached to the aortic wall is called the commissure. There are three commissures present in the aortic valve, and they provide support to the base of the leaflets.

1.4.5 Sinotubular Junction

The sinotubular junction is situated at the apex of the sinuses, and it serves as the boundary between the ascending aorta and the aortic root, denoting the exit point of AR and the start of the ascending aorta (Charitos and Sievers, 2013).

---

[1]Sinus of Valsalva is named after the Italian anatomist, Antonio Valsalva

11

1.5 Aortic Valve

Like other heart valves, the aortic valve ensures unidirectional blood flow. It opens during systole and closes during diastole to prevent blood regurgitation. In healthy patients, the peak velocity can reach up to 1.35±0.4 m/s (Hope et al., 2007). Functionally, the aortic valve should be considered a part of the left ventricular outflow track in conjunction with the aortic root (Schoen, 2008). Anatomically, the aortic valve typically consists of three leaflets, although some individuals have a bicuspid valve due to congenital differences. More infrequently, some individuals have a unicuspid valve (Jahanyar et al., 2022). Ultrasound is the typical imaging modality used to visualize the AV. This valve experiences some of the highest pressure differences in the cardiopulmonary system, which can lead to wear and tearing over time (Schneider and Deck, 1981). The leaflets of the AV are connected to the aortic root via the aortic annulus and are supported by commissures, which have a fibrous structure. The names of the leaflets correspond to the sinuses from which the coronary arteries emerge, including the left coronary, right coronary, and non-coronary sinuses (Cohen et al., 1991). In some sources, the left coronary sinus is referred to as the left posterior sinus, and the right coronary and non-coronary sinuses are referred to as the right posterior and anterior sinuses, respectively (Shan et al., 2017).
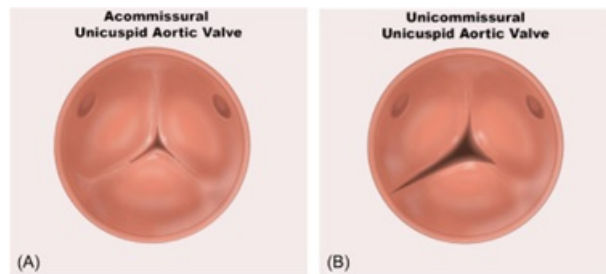
Figure 1.5: *Two unicuspid valve morphologies (Jahanyar et al., 2022)*

1.5.1 Leaflets

The leaflets of the aortic valve have a flexible structure that allows them to come together to close the orifice of the valve during diastole. Due to the thinness of the leaflets, vascularization of the valve is not crucial for the diffusion of oxygen and nutrients, as well as the disposal of waste products between the tissue and the surrounding blood (Weind et al., 2000). The cusps have three functionally specific layers, including the fibrosa, spongiosa, and ventricularis (see Fig. 1.6). The fibrosa, which is a densely packed collagen-rich tissue[2], faces towards the aorta. The fibrosa layer provides strength and stiffness to the leaflets and absorbs stresses during systole and diastole. The ventricularis is composed of radially aligned elastin fibers, which allow it to extend during diastole and recoil in systole. The ventricularis faces towards the left ventricle. The spongiosa, which is made up of glycosaminoglycans, is located between the fibrosa and ventricularis. It absorbs shear forces during the cardiac cycle and enables the two outer layers to slide over each other easily during leaflet motion (Della Rocca et al., 2000).

The whole aortic valve tissue consists of 41% collagen-rich fibrosa, 29% elastin-rich ventricularis, and 30% glycosaminoglycan-rich spongiosa (Gould et al., 2013).

The ventricularis layer faces unidirectional shear stress, which is rapid and pulsatile (Rathan et al.,

---

[2]in circumferential directions
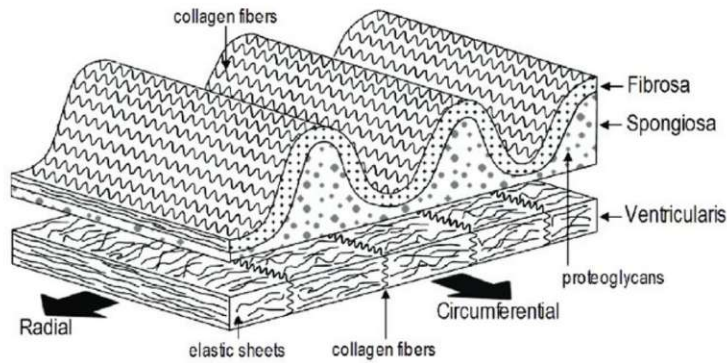
Figure 1.6: *Three layered leaflet structure (Korossis, 2018)*

2016). In contrast, the fibrosa layer is exposed to oscillatory stress (Mahler et al., 2014), which is linked to increased expression of inflammatory receptors and bone morphogenic proteins, as well as decreased expression of fibrosis and calcification inhibitors.
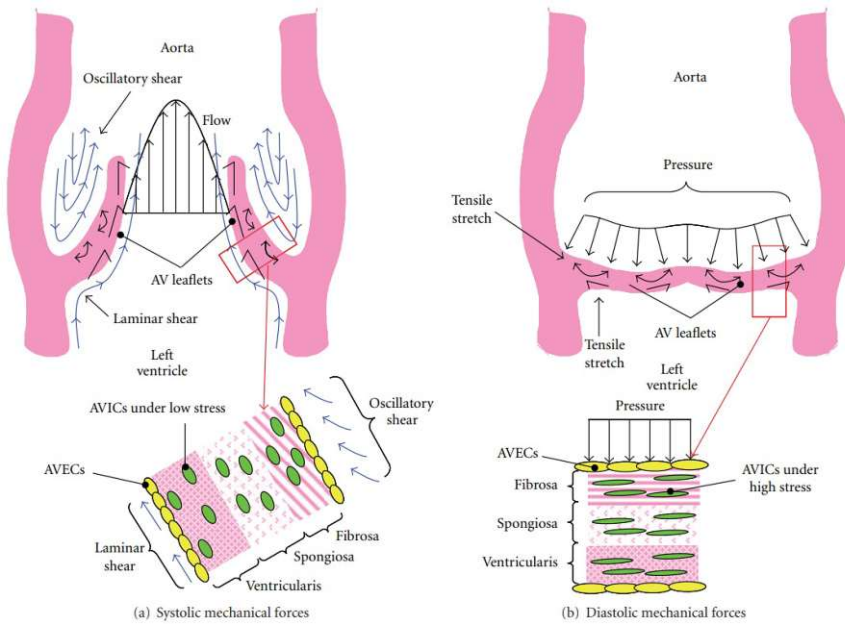
Figure 1.7: *Schematic of mechanical stresses experienced by the aortic valve during (a) peak systole, and (b) peak diastole (Balachandran et al., 2011).*

1.5.2 Aortic Valve Cell Population

The native AV composed of two cell types including valve endothelial cells (VECs), and valve interstitial cells (VICs). The valve endothelial cells, like all other endothelial cells, covers the outer surface of the leaflet, in a single monolayer form. In contrast, the heterogeneous VICs reside within the tissue matrix (Liu et al., 2017).

As aforementioned, VECs form a protective layer for the underlying tissue by regulating permeability, mediating inflammation, and preventing thrombus formation (Mackman, 2012). However, VECs can also exhibit immunogenic epitopes, such as major histocompatibility complex (MHC) class I and class II, or the α-Gal antigen (Caforio et al., 1990). *In vivo* studies show that VECs exhibit significant differences compared to vascular endothelial cells (Deck, 1986). Specifically, valve endothelial cells align circumferentially over the leaflet, perpendicular to the blood flow, while vascular endothelial cells orient parallel to the direction of blood flow (Deb et al., 2021). Furthermore, the hemodynamic stresses applied to the two sides of the leaflet are different. It is hypothesized that the differential transcriptional profiles of valve endothelial cells towards the aorta (fibrosa) may play an important role in the predominant localization of valve calcification.

Unlike the VEC, valve interstitial cells inhabit within the leaflets. The VICs synthesize and maintain the extracellular matrix (ECM) (Taylor et al., 2003). The VICs are composed of 95% fibroblast-like phenotype and 5% myofribloblasts-like and smooth muscle cells (SMC) (Ulloa et al., 2021, Grim et al., 2020). The phenotypes of VICs are assumed to be plastic and reversible, with fibroblasts being the predominant cell type in healthy adults. In case of injury or disease, fibroblasts obtain a secretory myofibroblast-like phenotype (aVIC) (Poggio, 2014, Chester and Taylor, 2007), where the primary indicator of aVIC is α-smooth muscle actin. This process enables secretion and turnover of ECM proteins, which repair micro-damages of the tissue and ensure the long-term durability of leaflet structure (Rabkin et al., 2001). The phenotype and function of VICs are regulated by the surrounding environment (paracrine endothelial-derived signals), inflammatory cytokines (TGF-β1), and mechanical stimuli produced by hemodynamic stresses (Balachandran et al., 2009).

1.6 Heart Valve Malfunction

Heart valves can have one of two malfunctions:

- ***Regurgitation (or leakage of the valve):*** The valve(s) does not close completely, causing the blood to flow backward through the valve (Tan et al., 2021). This results in leakage of blood back into the atria from the ventricles (in the case of the mitral and tricuspid valves) or leakage of blood back into the ventricles (in the case of the aortic and pulmonary valves).

- ***Stenosis (or narrowing of the valve):*** The valve(s) opening becomes narrowed or valves become damaged or scarred (stiff), inhibiting the flow of blood out of the ventricles or atria (Sellers et al., 2021). The heart is forced to pump blood with increased force in order to move blood through the narrowed or stiff (stenotic) valve(s).

It's possible for heart valves to experience both malfunctions at the same time (regurgitation and stenosis), and more than one heart valve can be affected at the same time (Unger and Tribouilloy, 2020). When heart valves fail to open and close properly, it can have serious implications for the heart, potentially compromising its ability to pump blood effectively throughout the body. Heart valve problems are one of the causes of heart failure.

Heart valve surgery is a procedure aimed at treating heart valve disease, which occurs when at least one of the four heart valves fails to function properly. During heart valve surgery, the surgeon repairs or replaces the affected heart valves (Durko et al., 2019). Various surgical approaches can be employed to repair or replace heart valves, such as open-heart surgery or minimally invasive heart surgery.

If a heart valve cannot be repaired, and a catheter-based procedure is not feasible, the valve might need to be replaced. To replace a heart valve, the existing valve is removed and replaced with either a mechanical valve or a valve derived from bovine or porcine tissue (a biological tissue valve). Every

year, more than 300,000 patients undergo cardiac valve replacement surgery to receive prosthetic heart valves, and this number is projected to reach 850,000 by the year 2050 (Fioretta et al., 2021). Currently, for older patients, Bioprosthesis valves are used.

1.7 Aortic Valve Prostheses

The aortic valve can be replaced by either a biological or mechanical valve prosthesis. Mechanical prostheses have high long-term durability but necessitate lifelong anticoagulant therapy with warfarin, whereas biological prostheses do not require the use of anticoagulants but have limited long-term durability (Duraes et al., 2021). Bioprostheses typically last 10–20 years but usually degenerate faster in younger patients. However, treatment with warfarin requires a lifelong commitment to regular tests and increases the risk of bleeding-related complications. Additionally, in the case of major bleeding or subsequent cardiac or non-cardiac surgery, anticoagulation therapy may have to be discontinued, posing a subsequent risk of mechanical valve thrombosis and death (Botsile and Mwita, 2020).

Thus, there is no perfect aortic valve prosthesis, and the selection of the type of prosthesis must be done carefully for each patient. In general, bioprostheses are recommended for older patients with multiple comorbidities (Harky et al., 2019), while mechanical valves are recommended for younger patients with a longer life expectancy (Iribarne et al., 2019). There are various types and brands of aortic valve prostheses available, which primarily differ in terms of structure and material.

1.7.1 Mechanical Valve Prostheses

Mechanical valves come in three types: tilting-disk, bileaflet, or caged-ball valves, although the latter is no longer used in clinical practice. The most commonly used mechanical valve today is the bileaflet prosthesis, which is made from pyrolytic carbon. In cases where aortic root replacement or concomitant aorta ascendens surgery is necessary, a Dacron graft with a mechanical valve sutured into one side can be used.

Although mechanical valves are very durable, they can also be prone to blood clots. To prevent these types of blood clots from forming, people who have these valves should take medication for life. This can be done using warfarin, which is a blood-thinning medication that is not recommended for use in pregnant women (Rahimtoola, 2010).

In addition to the disadvantages of lifelong warfarin use, mechanical valves can also be bothersome to certain individuals. For example, the opening and closing of the valve can sometimes be audibly noticeable outside the body.

1.7.2 History of Biological Heart Valves

In 1923, Cutler and Levine made the first attempt to correct heart valve disease. They performed valvotomy using a knife to treat mitral stenosis, but this procedure resulted in postoperative regurgitation caused by damaged leaflets (Cutler and Levine, 1923). Later, Lillehei and colleagues achieved the first implantation of a foreign valve by attaching polymeric leaflets to a mitral valve (Lillehei et al., 1957). Although this initial implantation failed quickly due to leaflet degeneration, it inspired further study and research into alternative prosthetic valve designs.

Ross was the first to use tissue valves in valve replacement, employing homografts[3] in 1962 and pulmonary autografts[4] in 1967 (Ross, 1967). The availability and preservation of cadaver homo-

---

[3]a graft of tissue taken from a donor of the same species as the recipient
[4]a tissue or organ that is transplanted from one part to another of the same body

grafts posed limitations, prompting exploration of xenografts as an alternative. The first (porcine) xenograft prototypes experienced rapid leaflet calcification and fibrosis due to immune response. Carpentier et al. (1968) introduced glutaraldehyde-treated tissue to enhance cusps' resistance. This pre-treatment extended valve durability; however, calcification tendencies persisted. In 1976, Carpentier and Edwards designed the first porcine valve attached to a stent. While this bioprosthetic valve simplified surgical implantation, it exhibited a poor hemodynamic profile attributed to higher stent stiffness and artificial commissures (Jamieson et al., 1990).

Bovine pericardium was utilized as an alternative material to enhance the durability of valves. The Ionescu-Shiley bovine pericardial biological valves were initially introduced in limited numbers in 1971 and became commercially available from 1976 onwards (Ruel et al., 1985). However, these valves exhibited rapid structural degeneration caused by excessive leaflet movement within the stent, leading to a high risk of valve insufficiency just a few years after implantation. To address this issue, improvements were made to bovine pericardial valves by suturing the leaflets to the stent from the outermost part to decrease impingement[5]. Furthermore, a thinner stent was used to reduce mechanical stress on the leaflets (Vesely, 2003).

David et al. (1988) designed and implanted the first stentless bioprosthetic, nevertheless, it showed worse durability than stented valves. Transcatheter aortic valve implant (TAVI) was introduced in 1990s by Andersen and Cribier. A balloon-expandable technique is required for TAVI (Cribier et al., 2002). Nowadays, there is a rise in the number of patients (who received a surgical aortic valve or medical therapy) are receiving a TAVI (de Jaegere et al., 2020).

1.7.3 Manufacturing of Bioprostheses

The multi-layer connective tissue pericardium sac is composed of collagen fibers, glycoproteins, glycosaminoglycans (GAGs), and cells. The regional variation in collagen fiber orientation within the pericardium makes it anisotropic. Small angle light scattering (SALS) is utilized to determine the regional fiber orientation, as shown in 1.8. A laser light is passed through the tissue, and the resulting scattered light is measured to determine the distribution of structural orientation of the fibers, specifically identifying the preferred-fiber direction (PD) (Whelan et al., 2021; Sacks and Schoen, 2002). This ensures the acquisition of uniform specimens. Following tissue selection (assisted by SALS) and trimming to the size and shape of a leaflet, the obtained tissue is chemically fixed. Subsequently, the fixed tissue is affixed to a stent as a support and sutured into the patient's body.

1.7.4 Bioprosthetic Valve Failure

Fatima et al. (2019) performed a systemic review of 167 studies as well as 12 Food and Drug Administration (FDA) reports, found 11 different definitions for structural valve degeneration (SVD). As an example, Senage et al. (2014) defined SVD as an average gradient of at least 30 mmHg with 1 square cm or less effective orifice area, or at least grade 3 of an intra-prosthetic aortic regurgitation.

1.7.4.1 Modes of Valve Failure

There are different modes of biological valve failure, which can be classified as follows:

- *Structural Dysfunction:* This refers to permanent intrinsic changes in the valve that result in hemodynamic or clinical dysfunction. These changes may include calcification, leaflet tear or wear, fracture, dehiscence, poppet escape, and embolization.

---

[5]a painful condition caused by rubbing or pressure on a tendon, nerve, etc., by adjacent structures.
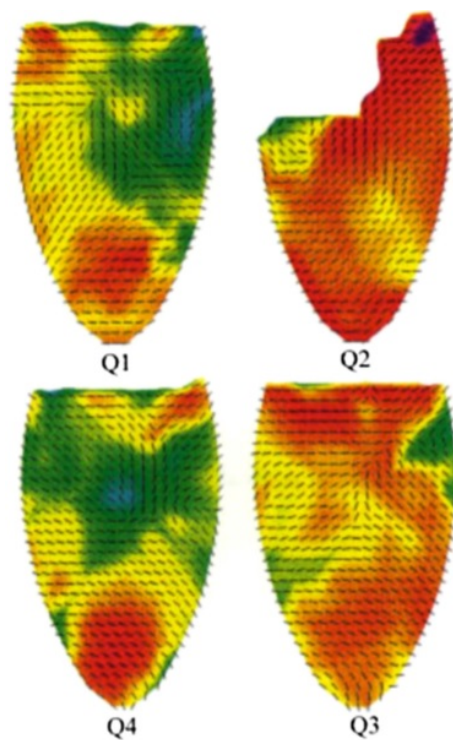
Figure 1.8: *Preferred fiber direction of the bovine pericardial sac displayed as vectors superposed onto color representation orientation index (Heister and Sacks, 1998)*

- *Non-structural Dysfunction:* This category involves non-intrinsic changes in the valve that lead to hemodynamic or clinical dysfunction. Examples of such changes include pannus formation, suture entrapment, paravalvular leak, and disproportion.

- *Thrombosis:* This mode of valve failure involves the formation of a thrombus (blood clot) on any part of the valve.

- *Endocarditis:* This refers to a life-threatening inflammation of the inner lining of the valve, which can lead to complications such as abscess formation, dehiscence, pseudoaneurysm, fistula, vegetation, and leaflet damage.

Structural Valve Deterioration
Structural valve deterioration is a slow process that occurs gradually over the course of several years. It involves calcification, leaflet tears, and fibrosis. Several risk factors have been associated with early structural valve deterioration (SVD), including young patient age, renal failure, hypertension, abnormal calcium metabolism, and prosthesis-patient mismatch (PPM) (Dvir et al., 2018).

Calcification
Heart valve calcification is a complex pathological process characterized by the deposition of calcium on heart valve leaflets, leading to impaired valve function and potentially life-threatening conditions. While calcification can arise from various factors, elevated mechanical stress has emerged as a significant contributor to the progression of this condition (Mohammed et al. 2020). Heart valve calcification is an active process, at which cells originating from valve, blood, and bone-marrow are

17

involved (Leopold, 2012). There exist couple of mechanisms to explain the pathogenesis of heart valve calcification. One mechanism suggests bone morphogenetic proteins stimulate VIC to have osteoblast function to initiate calcification (Song et al., 2017). Another mechanism claims that areas with high concentration of proinflammatory cytokines and macrophages cause degeneration of valve architecture (Kostyunin et al., 2019). Unfortunately, there exist no medical intervention to effectively decrease the progress of valve calcification.

Among all causes of SVD, calcification is contributed predominantly and related to bioprosthetic failure. In biological valves, calcification initiates intracellularly followed by expanding to extracellular matrix. In glutaraldehyde-treated bioprosthetic, *in vitro* studies suggested that glutaraldehyde promotes a dose-dependent and immediate influx of calcium ions from extracellular spaces and a rise of intracellular phosphate ions (Kim, 2001). Calcium ions penetrate glutaraldehyde-treated tissue through store-operated and L-type calcium channels. Since nonviable cells aren't able to hinder the concomitant increase of calcium and phosphate ions, nucleation occurs in the form of calcium-phosphate crystals. However, *in vitro* studies indicate that to delay the calcification by inhibiting the store-operated calcium channels. These calcium channels act as a major portal of calcium ions in glutaraldehyde-treated cells (Schoen and Levy, 1999).

Anti-calcification drugs, local therapy, and improvement of current bioprosthetic materials are the main ways of anti-mineralization. Two medical therapy including Bisphosphonates and Denosumab, are currently proposed to reduce differentiation of VIC into osteoblast-like cells (Furugen et al., 2021). Some techniques have been developed to replace glutaraldehyde-treatment, like epoxy-compounds which render bioprosthetic tissue similar in appearance to human tissue, but they are not clinically used yet (Yu et al., 2021).

Leaflet Tear
Tearing of the leaflets usually occurs in commissural regions and stent posts, where during the opening and closing of the valves face the highest stress. Tear takes place because of calcific nodules, high pressure gradient, or trauma secondary to sutures (Stanova et al., 2022). Flexible or thinner stents demonstrate less pressure gradient at commissures.

Non-structural Degeneration
Non-structural degeneration commonly involves valve abnormalities which are non intrinsic to the valve like pannus formation and paravalvular leak (Schaefer et al., 2019).

Pannus Formation
Growth of abnormal tissue surrounding a prosthetic is termed as pannus formation (Ha et al., 2018). Some cells infiltrate the suture line, such as fibroblasts, myofibroblasts, and capillary endothelial cells. This cell infiltration is a response to minor thrombus and inflammation from surgical implantation. During initiation, pannus formation leads to non-thrombogenic surface which might fasten the sewing ring. Hence, mild pannus decreases the risk of thromboembolism and paravalvular leak.

Paravalvular Leak
One of the most common modes of mechanical valve failure is paravalvular leaks[6], nonetheless, they can also take place in bioprostheses. Paravalvular leak is a leak caused due to a space left between natural heart tissue and the valve replacement from a previous transcatheter aortic or mitral valve replacement. It mostly affects the mitral valve than aortic valve. Paravalvular leak commonly occurs

---

[6]Also known as paravalvular regurgitation

due to suture failure, improper suture spacing, and tissue degradation (Bhushan et al., 2022).

Thrombus Formation
Another mode of failure in both mechanical and bioprosthetic valves is thrombus formation. Mechanical valves are more thrombogenic than the bioprosthetic valves, and patients with biological valves do not need lifelong anticoagulation. Factors related to valve thrombosis are high BMI, female sex, atrial fibrillation, poor cardiac function, and calcium supplements (Tagliari et al., 2022).

Infective Endocarditis
Infective endocarditis[7] is an infection typically with bacteria that enters the blood stream and settle in the heart lining, heart valve or blood vessel (Liesenborghs et al., 2020). Endocarditis usually take place where exist an abnormality in endocardium or the presence of microorganisms in blood stream. Endocarditis risk factors include congenital heart anomalies, rheumatic valve disease, bicuspid aortic valve, hypertrophic cardiomyopathy, and biological valve replacement. To prevent endocarditis, good level of dental hygiene and proper prophylactic antibiotic use (Wilson et al., 2021).

1.7.4.2 Factors Related to Valve Failure

Structural valve degeneration might lead to reoperation or prosthetic related death. Biological valve's durability varies based on the type of tissue used (porcine or bovine pericardial), implantation position (aortic or mitral), and patients' factors.

Bioprosthesis Factors
Bioprosthesis model directly affect the durability of the bioprosthetic valve. In general, porcine valves face more cusp tear with regurgitation (Keshishi et al., 2023), however pericardial valves are more prone to evolve stenosis (Lehmann et al., 2021). In a meta-analysis on 49190 patients who went through aortic valve replacement (AVR), with 66% bovine pericardial, and 34% porcine pericardial, Glaser et al. (2019) found no difference in survival between the two.

Patient Factors
Patient factors play an essential role in bioprosthetic failure. Age of patient is an independent predictor of valve failure. Younger patients, since have higher physiological demands, in comparison with older patients, they experience faster rate of wear and tear due to everyday activities (Marro et al., 2021).

1.7.5 Mechanical Behaviour of Bioprostheses Tissue

Mechanical testing usually consists of applying some sort of stimulus (i.e. forces or stresses) and measuring the response (i.e. displacement, or strain). A constitutive model explains the overall behaviour of the target material to the applied loads under the condition of interest. It is important that without an accurate constitutive model, it is not possible to clearly establish a valid relationship between the stimulus and the response. What is more, it must be kept in mind that no constitutive model can describe well for all ranges of stress and strain, loading cycles, etc.
Continuum mechanics is an attractive framework, by which active responses of a soft tissue at the macroscale can be modeled. Material is studied within each of infinitesimal particles. However, biological materials are inhomogeneous, and a tolerable error is needed to be accepted. Nonetheless, in case that the target tissue has a large enough length scale with respect to the local structural

---

[7]Also known as bacterial endocarditis

details, in a way that it is made up of a large number of infinitesimal particles, the structure can be handled as a continuum. Bovine pericardium composed of a hierarchically organized materials which have several orders of structural organization across multiple length-scales, like fibers or other large-scale structures, so that establishing an appropriate continuum scale might difficult. Overall, an acceptable continuum scale for each one of structures must be acquired. It is needless to say that the simplification in any analysis is expansive, but practicality and applicability of scaling is crucial. To study the BHV, framework of continuum mechanics is divided into two distinct but inter-related levels. As the first level, valve (i.e. biological aortic valve) works as an individual device, and how the hydraulic loads cause deformation of leaflets. With the help of finite element method, it is possible to answer questions like how is the stress distribution on the leaflets like. The second framework[8] (or the second level) is at tissue level. System experiments such as biaxial extension are needed to be performed to determine the mechanical response of material of the valve, to be able to answer question like which model is needed to be applied to describe the material's response. To receive accurate answer form finite element method (the first level), sufficient confidence on the second framework is required.

There exist many studies which evaluate the material properties of BHV leaflets. They are uniaxial tensile data, as well as biaxial tensile testing. Uniaxial data is pretty simple and provides basic assessment of tissue mechanics. On the other hand, most computational models are laid on the biaxial data.

1.7.5.1   Biaxial Tensile Testing

To characterize anisotropic materials (i.e. leaflets) biaxial tensile testing is needed. This type of test provides information about stress-strain relationship. Fiber oriented materials, such as soft tissues, demonstrate anisotropic behavior, and their show orientation dependent mechanical response. To have a better understanding of the biological tissues' response, biaxial tensile testing is more similar to the *in vivo* conditions. Also, development and applying anisotropic constitutive models, biaxial test data is needed. To perform biaxial mechanical test, first target surface must be cut, and then mounted in the loading fixture, by which loads in two orthogonal directions are applied. Loads and displacements are monitored while testing. For the case of pericardium, samples are needed to be placed in a bath of phospho-buffer-saline (PBS, pH 7.4), then undergo tension.

Effect of Cross-Linking

Chemically fixed heterografts, particularly those treated with glutaraldehyde, have shown reduced potential for *in vivo* structural degradation. The crosslinking of amine groups through a Schiff's based reaction with glutaraldehyde is an effective and widely used method for collagen crosslinking and tissue fixation. Although aldehyde fixation can impact the mechanical properties of leaflets, it initially does not elicit an immune response. However, long-term concerns regarding the calcification susceptibility of glutaraldehyde-treated pericardium have raised concerns about its cytotoxicity.

To address these concerns, studies have focused on exploring alternative fixation methods with the goal of reducing calcification potential, preserving the mechanical properties of native tissues, and minimizing cytotoxicity. These investigations aim to find fixation approaches that strike a balance between maintaining tissue integrity and minimizing adverse effects.

In the study by Pereira et al. (1990), polyglycidyl-ether and glutaraldehyde were used as fixatives for bovine pericardium. This fixation method resulted in significant crosslinking, leading to a reduction in stress relaxation and an increase in extensibility of the tissue. On the other hand, Bemacca et al. (1992) employed cyanimide as a fixative for bovine pericardium. Their findings indicated that

---

[8]Characterization of material properties

cyanimide fixation did not effectively crosslink the tissue. They also observed that the ultimate tensile strength and modulus of the specimens increased with heat-drying, but freeze-drying had no significant effect. Genipin and carbodiimide have been studied as alternative fixatives, and they have demonstrated effective crosslinking properties. However, it is important to note that these fixatives can generate distinct crosslinking structures, which can have an impact on other properties of the chemically treated tissue, as shown by Jang et al. (2012). The specific crosslinking structure induced by each fixative can influence the mechanical and biological properties of the treated tissue. In the study conducted by Langdon et al. (1999), a zero-pressure glutaraldehyde fixation technique was employed. The results demonstrated minimal alterations in the functional biomechanics of the tissue. Additionally, the zero-pressure fixed tissue was found to be softer and more extensible compared to tissue treated under normal pressure. Fixation pressure was shown to have an impact on the transvalvular properties of the tissue. Accelerated cyclic-loading tests conducted by Wells and Sacks (2002) revealed that porcine tissue fixed under zero-pressure conditions exhibited conformational changes under long-term cyclic loading. Ultimately, this led to a decline in extensibility to a level comparable to that of specimens fixed under low-pressure conditions.

1.7.6 Constitutive Models

Cataloglu et al. (1977) were the pioneers in attempting to describe the properties of valve tissue. They proposed a linear elastic model based on Hooke's law. Although the assumption of a linear stress-strain relationship can yield acceptable results under small displacements, it does not accurately capture the nonlinear behavior observed in heterografts and the finite large deformations involved in valve function. In order to approximate the nonlinearity of the material, Hamid et al. (1986) introduced a piece-wise linear tangent modulus as an alternative computational method.

The main drawback of the linear elastic framework is its inability to accurately model finite deformations, thus limiting its ability to simulate realistic valve behavior. To address this limitation, hyperelastic models have been employed to describe the behavior of leaflets under finite deformations and simulate valve function (Sun and Sacks, 2005). One of the commonly used hyperelastic material models is the exponential form proposed by Chuong and Fung (1983), which characterizes the mechanical properties of soft biological tissues such as pericardium.

1.7.6.1 Hyperelastic Models

Chemically fixed tissue can be described using an orthotropic Fung-type hyperelastic model. The stress in the tissue can be computed using the second Piola-Kirchhoff stress tensor. This can be expressed mathematically using Equation 1.1.

$$S = \partial W / \partial E \tag{1.1}$$

where S is second Piola-Kirchhoff stress, W is strain energy function, and E is Green-Lagrange strain tensor. The assumption of a 2-dimensional (2D) constitutive law is made for chemically fixed tissue, considering the thin thickness of the leaflet. In this 2D model, the directions 1 and 2 are aligned along and perpendicular to the fiber direction, respectively, while the direction 3 represents the transverse direction.

Although pericardium is not a homogeneous membrane, the in-plane bending response is neglected in this model, likely due to the thinness of the leaflet. However, to account for the neglected bending response and to capture the high in-plane shear behavior, Sun et al. (2003) proposed a more comprehensive constitutive relation. This enhanced model incorporates higher-order terms to better

21

represent the material's behavior under shear deformation. General Fung elastic 2D anisotropic model with plane stress assumption is:

$$W = \frac{c}{2}(e^Q - 1) \tag{1.2}$$

with

$$Q = a_1 E_{11}^2 + a_2 E_{22}^2 + 2a_3 E_{11} E_{22} + a_4 E_{12}^2 + 2a_5 E_{11} E_{12} + 2a_6 E_{12} E_{22} \tag{1.3}$$

where c and ai are material constants. To calculate the energy function Sacks and Chuong (1998) proposed Equation 1.4

$$W = b_0[exp(\frac{1}{2}b_1 E_{PD}^2) + exp((\frac{1}{2}b_1 E_{XD}^2) + exp(b_3 E_{PD} E_{XD}) - 3] \tag{1.4}$$

where PD and XD are aligned direction and perpendicular directions to the direction of fibers, respectively[9].

The implementation of the Fung model in finite element formulations has been limited due to inherent numerical instability and convergence issues. This instability arises from the conditional convexity or ellipticity of the Fung model, as well as the exponential behavior of the model. Small changes in strain can result in significant changes in stress, which can lead to numerical difficulties in solving the equations (Wilber and Walton, 2002).

As a result, alternative models have been proposed to overcome these numerical challenges. One such model is the Mooney-Rivlin model, which is another hyperelastic material model commonly used to describe the mechanical behavior of soft tissues. The Mooney-Rivlin model (Equation 1.5) offers better numerical stability and convergence properties compared to the Fung model. It provides a more robust framework for simulating the mechanical response of tissues under finite deformations in finite element analyses (Rassoli et al., 2022).

$$W = \mu_1(I_1 - 3) + \mu_2(I_2 - 3) \tag{1.5}$$

where I_1 and I_2 are principal invariants of left Cauchy-Green strain tensor, μ_1 and μ_1 are parameters of material.

1.7.7 Mechanical Stress and Valve Degeneration

Heart valve calcification is a degenerative process characterized by the abnormal accumulation of calcium on valve leaflets, leading to stiffening, impaired movement, and valve dysfunction. Among the various factors influencing calcification, elevated mechanical stress has emerged as a significant contributor in recent studies (Kruithof et al., 2021). Valve degeneration can result from repetitive mechanical stress, leading to calcification, wear, and leaflet rupture (Pawade et al, 2019). Low-grade immune rejection can trigger inflammation, but oxidized lipids or thrombosis can also cause calcification of leaflets. Although chemically fixing the valve's tissue reduces antigenicity and ensures chemical stability, it causes calcium influx due to membrane damage. This damage to the membrane, combined with residual phospholipids, creates an environment with a high potential for calcium nucleation (Di Vito et al., 2021). The combination of leaflet mechanical stress and patient factors contributes to calcium crystal formation and, in severe cases, can cause connective tissue disruption. This biochemical process leads to cusp thickening, leaflet stiffness, tears, and perforations (Conte et al., 2021). Systemic hypertension also contributes to stress on the leaflets, resulting in tissue deterioration (Abramov et al., 2023). Smaller bioprostheses generally cause higher mechanical stress,

---

[9]These directions on the tissue can be identified via SALS

increasing the risk of structural valve deterioration (Moskowitz et al., 2022). Comparisons between stented and stentless bioprostheses indicate that stentless bioprostheses experience less mechanical stress (Duncan et al., 2019).

The role of mechanical stress in valve calcification can be categorized into two main criteria including hemodynamic forces and valve leaflet strain. Besides, other physiological and pathological processes can accelerate calcium formation in the leaflets. These include phospho-calcic metabolism disorders (Carrai et al., 2020) associated with conditions such as kidney failure, osteoporosis, and hyperparathyroidism (Le Tourneau et al., 2007).

Immune Process

Biological heart valves, despite being chemically fixed, may not be entirely immunologically inert. Residual animal antigens present in these valves can potentially stimulate both humoral and cellular immune responses, leading to nucleation and disruption of the valve (Human et al., 2022).

Inflammatory Processes

Lipid-mediated inflammation is a contributing factor to structural valve deterioration, not only in native aortic valves but also in biological valves. Inflammatory cells can lead to the production of matrix metalloproteinases, which in turn can cause degradation of collagen fibers and disruption of leaflet tissue (Kostyunin and Glushkova, 2020).

Cahill et al. (2022) conducted a study showing that 15% of patients experienced valve thrombosis after undergoing aortic valve replacement. Valve thrombosis commonly occurs within the first 2 years following the operation, with the highest risk period being the first 3 to 6 months postoperative. Severe hemodynamic valve deterioration is responsible for approximately 10-20% of cases of valve thrombosis. Although anticoagulation therapy can often reverse the thrombosis in biological valves, this complication can still lead to cusp inflammation, which in turn contributes to leaflet fibrosis and calcification. Similarly, even with treatment using antibiotics, infective endocarditis can lead to structural valve deterioration.

1.7.7.1 Mechanisms of Heart Valve Calcification due to Mechanical Stress

Understanding the mechanisms underlying biological heart valve calcification due to mechanical stress is crucial for developing strategies to improve the longevity of these valves. Key mechanisms involved in calcification processes in surgical biological heart valves under elevated mechanical stress are explored.

Hemodynamic Forces and Mechanical Stress

Hemodynamic forces exerted on surgical biological heart valves, such as shear stress and pressure gradients, are critical for their proper functioning. However, surgical implantation can disrupt the natural valve architecture and alter blood flow patterns, leading to changes in mechanical stress. Elevated mechanical stress resulting from altered flow patterns, turbulent flow, or abnormal pressures can trigger a cascade of events leading to heart valve calcification (D'Alessandro et al., 2021).

Valve Leaflet Strain

Surgically implanted biological heart valves experience cyclic mechanical strain during each cardiac cycle. The altered mechanical environment and structural modifications of the valve leaflets can affect their response to strain (Whelan et al., 2021). Prolonged exposure to increased mechanical strain can disrupt the delicate balance of the ECM within the valve leaflets, initiating the calcification process.

23

Inflammatory Response
Elevated mechanical stress within surgically implanted biological heart valves can trigger an inflammatory response. Surgical procedures and the foreign nature of the implanted valve can induce an immune response, leading to the release of inflammatory cytokines and chemokines (Xiong et al., 2022, Teng et al., 2020). This inflammatory environment can stimulate VICs to differentiate into osteoblast-like cells, which play a crucial role in the initiation of heart valve calcification (Grim et al., 2020).

Osteogenic Transdifferentiation of VICs
Under the influence of elevated mechanical stress, VICs within bioprosthetic heart valves can undergo phenotypic changes known as osteogenic transdifferentiation (Gu et al., 2019). Osteogenic transdifferentiation involves the transition of VICs from a quiescent state to a calcifying phenotype, characterized by the expression of bone-related markers and the initiation of calcium deposition. This process is regulated by various signaling pathways, including bone morphogenetic protein (BMP) signaling and Runx2 (Yang et al., 2020).

Imbalance in Calcification Regulatory Factors
Elevated mechanical stress in surgical biological heart valves disrupts the balance between calcification-promoting and calcification-inhibiting factors. Increased mechanical stress upregulates the expression of calcification-promoting factors, such as BMP-2 and Wnt/β-catenin signaling, while inhibiting the expression of calcification-inhibiting factors, such as matrix Gla protein (MGP) and osteopontin. This dysregulation favors the calcification process and inhibits protective mechanisms, leading to accelerated heart valve calcification (Vadana et al., 2020).

Matrix Remodeling and Calcium Deposition
Elevated mechanical stress alters the composition and structure of the ECM within surgical biological heart valves. ECM remodeling involves the degradation of collagen and elastin fibers and the subsequent deposition of calcium salts (Jin et al., 2019). Cellular processes mediated by osteoblast-like cells derived from VICs, including the release of matrix vesicles, contribute to the nucleation and growth of calcium crystals, ultimately leading to calcification within the valve leaflets (Grim et al., 2020).
All in all, heart valve calcification in surgically implanted biological heart valves due to mechanical stress involves complex interactions between hemodynamic forces, cellular responses, and molecular signaling pathways.

Chapter 2

Material and Methods

In this chapter, the methods and materials required for fluid-structural interaction (FSI) simulation are described. The choice of the mathematical method and its application is important in the simulation. Consideration must be given to all aspects that directly impact the accuracy of the results, such as mesh quality.

The Avalus aortic biological heart valve (Medtronic, Minneapolis, MN, USA; 21 mm, Figure 2.1) was scanned with μ-CT, which enabled us to obtain a high-resolution image of the valve. The high resolution directly affects the quality of the design, which in turn affects the accuracy of the results.

2.1 Micro-CT

Computed tomography (CT), also known as computed axial tomography (CAT scanning), was first invented in 1967 by Sir Godfrey Hounsfield (Buchlak et al., 2022). It utilizes X-ray technology to generate detailed images of the body. In its early days, CT machines were slow, taking several hours to collect data for a single slice and days to reconstruct an image. However, with advancements in technology, modern CT machines can scan a sample and reconstruct the image within minutes. CT scanning is widely employed in various fields to examine different parts of the body, and it has numerous applications. It is utilized to visualize and measure brain strokes, diagnose and stage cancer, conduct vascular studies, perform interventional procedures such as biopsies, and assist in both diagnostic and therapeutic settings (Liguori et al., 2015). Recently, CT has also played a significant role in providing information about the evolution and severity of COVID-19 (Li, 2020).

CT is a non-invasive scanning method that keeps the sample intact. It allows visualization of a slice without the need to cut the sample. Micro-CT, introduced in the 1980s, applies the same non-invasive method as CT but offers much higher resolution, down to 1 μm, compared to the limited 1 mm resolution of CT machines commonly used for clinical diagnosis (Li et al., 2020).

In the field of biomedical engineering, micro-CT is commonly employed to study samples with high X-ray beam absorption, like bones, but it lacks the ability to effectively visualize weaker absorbing components such as soft tissues. However, advancements in technology have led to the use of nanometric contrast agents, which enhance the contrast in both CT and MRI imaging modalities (Silva, 2015).

Currently, there are two types of micro-CT scanners: *in vivo* and *in vitro* scanners. In an *in vitro* scanner, the specimen rotates between a stationary X-ray source and detector. In this setup, radiation dose and time are not significant limitations, allowing for higher spatial resolution (up to
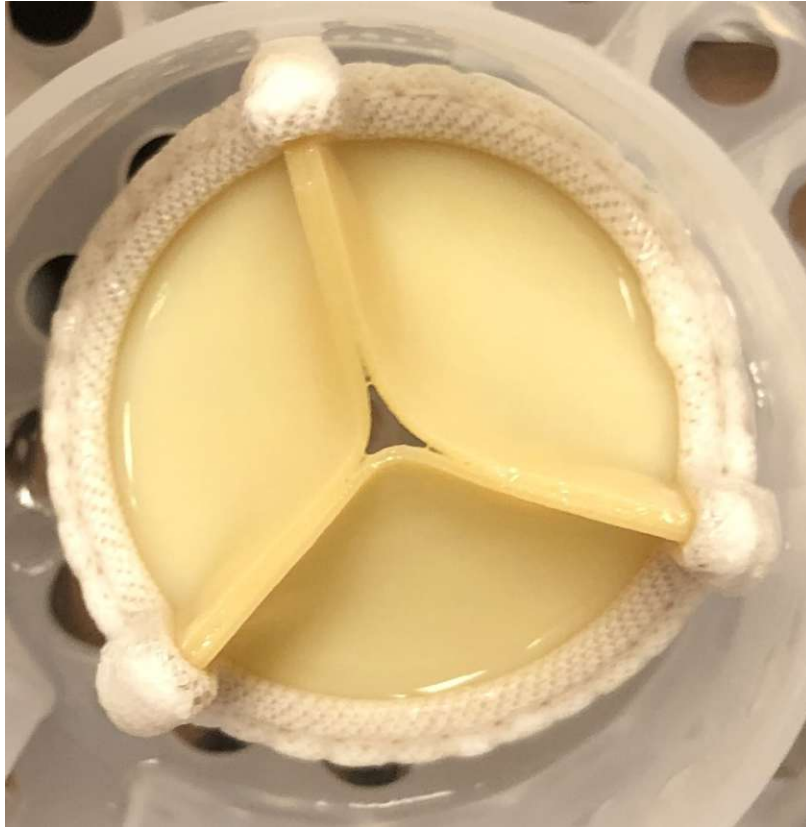
Figure 2.1: *Overview of Avalus Aortic Valve which used for this study.*

1 μm) compared to *in vivo* micro-CT. In *in vivo* scanners, the sample or object remains stationary while the X-ray source and detector rotate around it. These scanners offer spatial resolutions ranging from 100 to 30 μm and can generate images faster compared to *ex vivo* micro-CT (Badea et al., 2008).

2.2   Geometry Reconstruction

The native aortic valve (or biological valve) and its root together constitute a complex geometry, including cusps or leaflets (and for the biological valve, a stent), as well as sinuses connected along the commissures. Following the aortic root is the ascending aorta.

The geometry of interest in this thesis consists of several components, namely the aortic root, ascending aorta, and biological valve. The design of these components can be divided into two parts: the aortic root (AR) and ascending aorta (AAo) as the first part, and the biological valve as the second part.

Since this study is not patient-specific, the design of the aortic root and ascending aorta needs to be generalized. Currently, *in vivo* methods for this purpose are limited, relying on measurements from 2D sections of echocardiograms. However, due to the transient nature of the cardiovascular system, this task is challenging (Cartier et al., 2005). Previous studies, such as Reul et al. (1990), designed the aortic root based on 604 angiographic films. In more recent studies, CT images and

measurements derived from the collected data have been used to design both the aortic root and the aorta (Ovcharenko et al., 2014).

To design the aortic root and ascending aorta, SpaceClaim software was utilized. For the valve reconstruction, both 3-matic and SpaceClaim were employed. The following sections provide a detailed explanation of the design process for both components.

2.2.1 Aortic root and Ascending Aorta

The measurements and dimensions of the AR used in this study (Table 2.1) were obtained from Becsek et al. (2020). In their study, Becsek et al. employed a symmetrical epitrochoid (Fig. 2.2 left) as the midplane of the AR, connected to two cylinders with circular cross-sections. However, it is important to note that the actual geometry of the AR is not symmetrical, and the left ventricular outflow tract does not have a circular cross-section.

Table 2.1: Parameters and values of AR and AAo, used by Bescek et al.

PARAMETER	VALUE [m]	DESCRIPTION
R_A	0.011	Aortic annulus radius
R_{CO}	0.01375	Commissure radius
R_{MC}	0.0050	Mid-circle radius
R_{SP}	0.0121	Sinus-portion radius
R_{AAo}	0.01375	Ascending aorta radius
H_A	0.02	Aortic annulus height
H_S	0.0077	Maximum sinus radius height
H_{STJ}	0.0165	Sinus height
H_{AAo}	0.05	Ascending aorta height
H_{WALL}	0.002	Aortic wall thickness
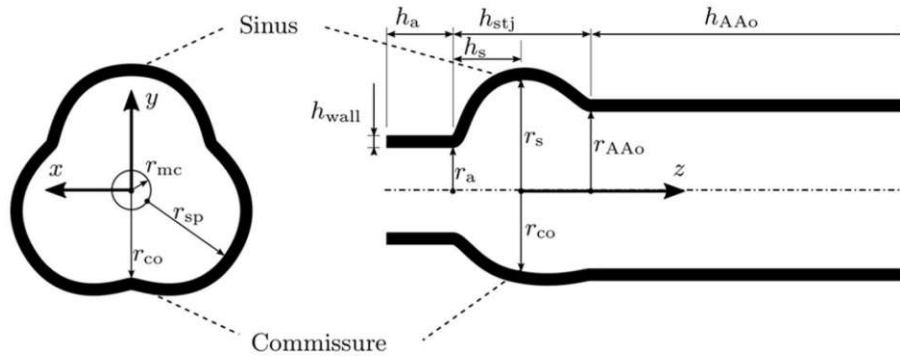
Figure 2.2: *Longitudinal and cross section view of the AR as well as AAo, used by Becsek et al.*

In order to facilitate the development of inlet flow, the length of the cylinder inlet was set to h_a. For the design of the ascending aorta, the radius r_{AAo} was selected. In this study, the ascending aorta was modified, replacing the straight cylinder with an arc-shaped structure. The specific arc and its length were determined based on a patient's CT image of the aorta.

27

2.2.2 Valve Reconstruction

In this study, a biological aortic valve with a diameter of 21 mm (Figure 2.1) was scanned using a μ-CT machine (SCANCO μCT 50, SCANCO Medical AG, Brutistellen, Switzerland). The sample was scanned with a μCT scanner using 70 kVp, 200 μA, a 0.5 mm Al filter, 570 projections, and 150 ms integration time. The resulting image was reconstructed at an isotropic resolution of 31 μm. The reconstructed image was then converted to an "stl" file (Fig. 2.3) for further processing. The valve reconstruction involved capturing the leaflets and stent.
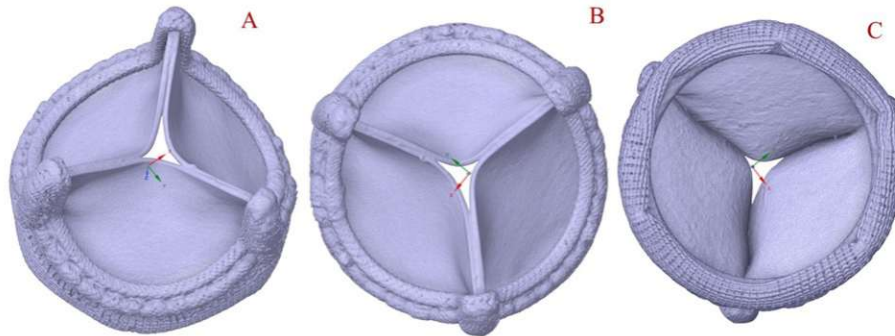
Figure 2.3: *stl file of μ-CT scan of the valve*

2.2.2.1 Leaflets

To reconstruct the leaflets, the software 3-matic was initially utilized. A surface of interest was trimmed, and a thickness of 0.5 mm was assigned to it. This process was repeated for each leaflet individually using 3-matic. Subsequently, the resulting outcome was converted into an "stl" file (Fig. 2.4) for further processing and analysis.
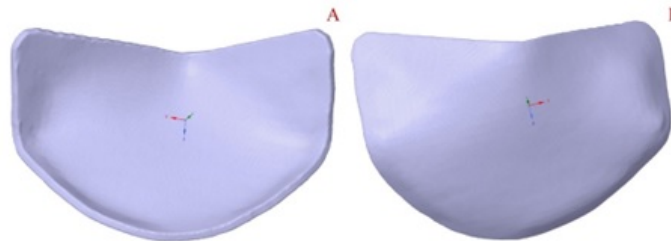
Figure 2.4: *stl file of one of the leaflets*

As the subsequent step, the three obtained leaflets were imported into SpaceClaim. In SpaceClaim, they were initially wrapped with a size of 0.1 mm. The "Shrinkwrap" option in SpaceClaim was utilized to create a smooth surface in the form of an stl file, ensuring the absence of any irregular edges. Following this, each wrapped leaflet was converted into a solid format (STEP) in order to conduct the simulation, which was accomplished using Autoskin (Fig. 2.5).
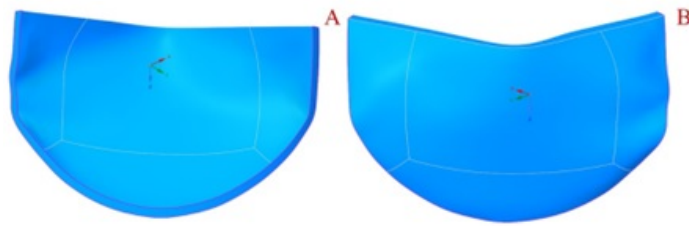
Figure 2.5: *STEP file of one leaflet*

2.2.2.2 Stent

To generate a solid stent for the simulation, the stl image of the valve needs to be opened in SpaceClaim. Similar to the leaflets, it is necessary to apply the wrapping[1] process to the stl image, followed by converting the outcome into a solid format.

2.2.2.3 Multi-Body Part

Once the solid forms of the stent and leaflets are obtained, they should be grouped together as a multi-body part (Fig. 2.6, E and F). Grouping the components in this way offers several advantages, including the ability to define different mechanical properties for each part. In SpaceClaim, the "Share Geometry" option allows for this functionality to be implemented.
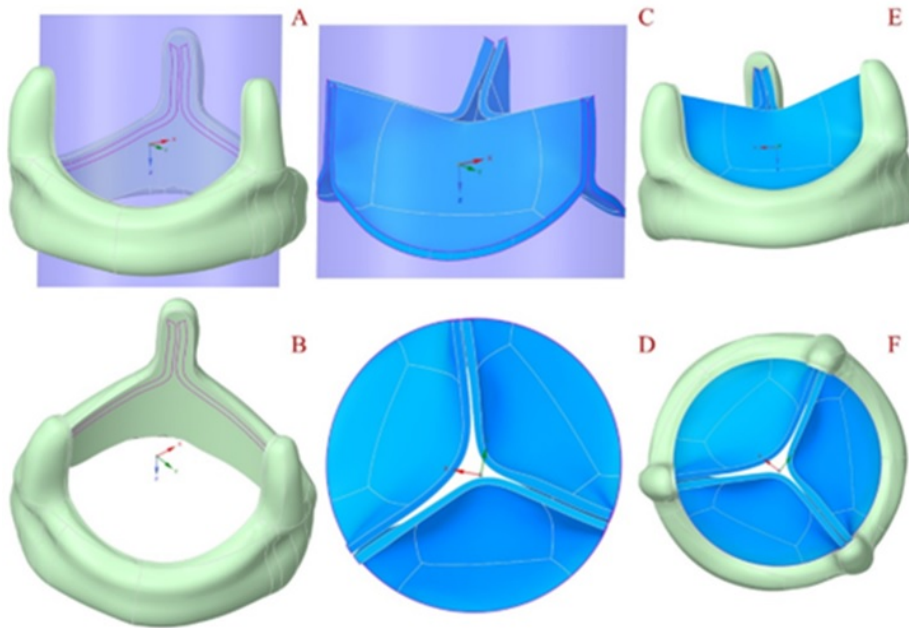
Figure 2.6: *Stent and leaflets, A: stent with the cylinder, B: stent after was cut, C: leaflets with cylinder, D: leaflets after were cut, E, F: multi body of stent and leaflets*

---

[1]With the element size of 0.3 mm

2.2.3 Mesh Metric

In numerical simulations, the accuracy of the results heavily relies on the quality of the mesh. A good mesh can yield more accurate results, whereas a poor mesh can lead to less accurate or even inaccurate results. Thus, evaluating the quality of the mesh is crucial. Various methods exist to assess the acceptability of a model's mesh. In ANSYS, several mesh metrics are available, such as Jacobian ratio and skewness, and so on which can be utilized to verify the quality of the mesh.

2.2.3.1 Skewness

Skewness is an angular measure that indicates the quality of an element in relation to the angles of ideal element types. In finite element analysis, skewness serves as a primary measure of mesh quality, providing insight into how closely a face or cell aligns with the ideal shape (Park et al., 2020).

2.3 Fluid-Structure Interaction

Fluid-Structure Interaction refers to the dynamic interaction between a flowing fluid and a solid body. FSI occurs when a fluid exerts pressure or applies thermal loads on a solid, resulting in significant structural deformation that, in turn, affects the fluid flow (Hami and Radi, 2017). It involves the mutual influence of fluid and solid behavior, where changes in one component affect the behavior of the other component.

FSI can be classified into two main types: one-way FSI and two-way FSI. In one-way FSI (Fig. 2.7), also known as one-directional FSI, physical properties obtained from the fluid domain are transferred to the structural domain without any feedback from the solid. This type of interaction is exemplified in scenarios such as explosions, where the outcome of the fluid domain is imposed as an external load on the solid, without any reciprocal effect on the fluid. In other words, the interaction between the fluid and solid is unidirectional, occurring solely from the fluid to the solid; only one-directional interaction (Chen et al., 2022).
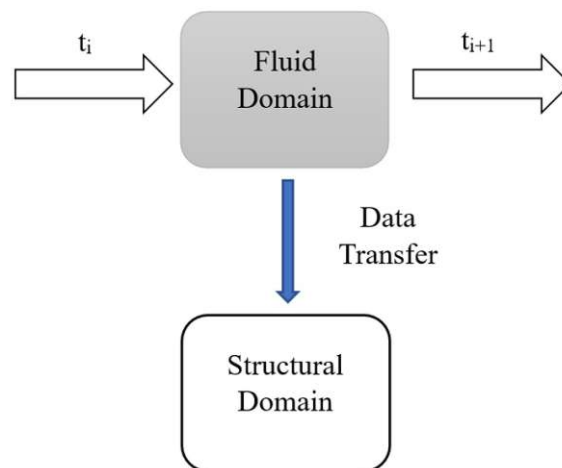
Figure 2.7: *Schematic of one-way FSI*

In two-way FSI, there is a bidirectional interaction between the fluid and solid domains (Fig. 2.8).

The forces or fluid pressure deform the solid, and the deformed solid, in turn, affects the flow field. This necessitates solving both the fluid and solid domains simultaneously, with a two-way data transfer. Forces are exported from the computed fluid dynamics (CFD) analysis to the finite element analysis (FEA) of the structural domain, while deformations are transferred back from FEA to CFD. This iterative process continues until both solutions converge, with each coupling iteration updating the geometry of the fluid field based on the deformation of the solid (Krishna et al., 2022).
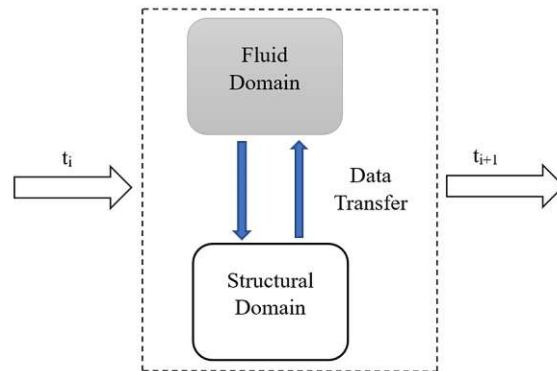
Figure 2.8: *Schematic of two-way FSI*

Prosthetic heart valves can generate turbulent blood flow in the AR and AAo. Turbulent blood flow has the potential to negatively affect blood characteristics, the aortic wall, and valve performance (Obrist and Carrel, 2021). This turbulent flow pattern can be associated with the initiation of thrombus formation and platelet activation. Additionally, the resulting non-physiological wall shear stresses in the AAo may contribute to endothelial damage. It is also important to consider the impact of hypertension on leaflet dynamics and how it may influence valve degeneration.

In order to gain a better understanding of the effects of turbulent flow downstream of the valve, it is necessary to conduct a detailed characterization and accurate assessment of momentum transfer within this flow (Geronzi et al., 2021). This can be achieved through the application of FSI analysis. Such a study can provide insights into shear-induced thrombocyte activation, valve performance in terms of hemodynamics, and the presence of non-physiological wall shear stresses (WSS). By investigating these aspects, a deeper understanding of the impact of turbulent flow on the valve and surrounding environment can be attained.

In a two-way FSI analysis conducted in ANSYS, data exchange between the fluid and solid domains occurs through an intermediate system coupling (Fig. 2.9). Forces are transferred from the fluid domain to the solid domain, and the resulting displacements are transferred back to the fluid domain. This iterative cycle is repeated until a converged solution is achieved for both the fluid and structural governing equations (Ben et al., 2021). This process is performed for each time step to capture the dynamic behavior of the system accurately.
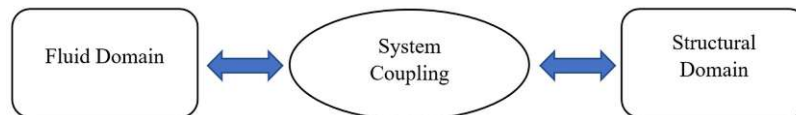
Figure 2.9: *Schematic of two-way FSI in ANSYS*

2.3.1 Reynolds Number

Reynolds number (Re) in the Left Ventricle and Ascending Aorta plays a crucial role, mostly for patients with an artificial heart valve. Applying the appropriate model for studying fluid dynamics is directly dependent on the Re, so it is important to have a better insight into the Re through the target area.

Calculating the Re in the Aorta is not a new topic. Various methods have been applied, and different ranges have been reported, indicating turbulent flow regime. In a study conducted by Stein and Sabbah (1976), Re was calculated in the ascending aorta of 15 individuals (seven normal, seven with aortic valvular disease, and one with a prosthetic aortic valve). Point velocity was measured using a hot-film anemometer probe. The peak Re ranged from 5700 to 8900, and blood flow was highly distributed during peak ejection. Non-invasive techniques such as laser Doppler anemometer (LDA) can also be employed to measure Re, as demonstrated by Leinan et al. (2022). Pinotti and Faria (2006) utilized LDA to measure Re and reported a range between 3300 and 6800 for patients with a bovine pericardium bioprosthesis valve (25 mm).

Stalder et al. (2011) demonstrated that the average Re in the ascending aorta is 4500. In their study, Stalder et al. examined 30 individuals using flow-sensitive MRI to indirectly assess Re.

2.3.2 Various Turbulence Models

The eight RANS[2] turbulence models vary in their approach to modeling the flow near walls, the number of additional variables they solve for, and the interpretation of these variables (Eivazi et al., 2022). These models all enhance the Navier-Stokes equations by incorporating an extra term for turbulence eddy viscosity, but they diverge in their methods of computation.

2.3.2.1 k-ϵ

The k-ϵ model is a turbulence model that solves for two variables: k, representing the turbulence kinetic energy, and ϵ (epsilon), representing the rate of dissipation of turbulence kinetic energy. This model utilizes wall functions, which means that the flow in the buffer region is not simulated (Lasrado et al., 2022). The k-ϵ model has historically been widely used in industrial applications due to its favorable convergence rate and relatively low memory requirements. However, it may not accurately compute flow fields with adverse pressure gradients, strong flow curvature, or jet flow (Rahman et al., 2022). Nonetheless, it performs well in solving external flow problems involving complex geometries. For instance, the k-ϵ model can be employed to study the airflow around a bluff body.

2.3.2.2 k-ω

The k-ω model is similar to the k-ϵ model but differs in that it solves for ω (omega), which represents the specific rate of dissipation of kinetic energy. It is considered a low Reynolds number model and can be used in conjunction with wall functions. Compared to the k-ϵ model, the k-ω model exhibits more nonlinearity, making it more challenging to converge, and it is sensitive to the initial guess of the solution. However, the k-ω model is particularly useful in cases where the k-ϵ model may not provide accurate results, such as internal flows, flows with strong curvature, separated flows, and jets (Onah et al., 2022). An example of an internal flow where the k-ω model can be applied is the flow through a pipe bend.

---

[2]Reynolds-averaged Navier–Stokes equations (RANS equations) are time-averaged equations of motion for fluid flow

2.3.2.3 *SST*

The SST (Shear Stress Transport) model is a hybrid turbulence model that combines the k-ϵ model in the free stream with the k-ω model near the walls (Franke et al., 2022). It is commonly used as a preferred model for industrial applications, particularly in cases involving low Re. The SST model shares similar resolution requirements with the k-ω model and the low Re k-ϵ model. However, its formulation addresses certain limitations observed in the pure k-ω and k-ϵ models, making it a popular choice due to its improved performance.

2.3.3 Governing Equations

As previously mentioned, to gain a deeper understanding of how blood flow can impact a bio-prosthetic valve, a two-way FSI simulation needs to be conducted. This simulation involves solving governing equations in both the Lagrangian and Eulerian systems, using the Arbitrarily Lagrangian-Eulerian (ALE) framework. The governing equations consist of both CFD equations and FEA equations (Xu et al., 2021). The fluid part involves solving the continuity equation and momentum equations, while the structural part requires satisfying the elastodynamics equations.

2.3.3.1 Fluid Field

The equations governing the fluid field consist of the momentum equations, also known as Navier-Stokes equations (Equation 2.1), as well as the continuity equation (Equation 2.2) (Ershkov et al., 2021).

$$\rho_f[\frac{\partial \vec{V}}{\partial t} + ((\vec{V} - \vec{W}) \cdot \nabla)\vec{V}] = \nabla \cdot (\overline{\overline{\tau}}_f) + (\vec{f_f}) \tag{2.1}$$

$$\frac{\partial \rho}{\partial t} + \nabla \cdot (\rho_f \vec{V}) = 0 \tag{2.2}$$

where ρ_f is fluid density, $\overline{\overline{\tau}}_f$ is stress tensor, $\vec{f_f}$ body force per unit volume, $\vec{V}$ velocities, and $\vec{W}$ is the moving grid.

In the simulation conducted using ANSYS Fluent, the transient flow was solved. The fluid domain was divided into discrete elements, and the Finite Volume Method (FVM) was employed to solve the governing equations (Lopes et al., 2021). Once the entire domain was partitioned into cells, the governing equations were integrated across these cells to form algebraic equations through a process called discretization. Subsequently, the algebraic equations were linearized and solved using a pressure-based solver. The iteratively solved equations were utilized to update the fluid pressure and velocity domain.

Discretization of Momentum Equation
The transport equations for a scalar quantity φ, which are unsteady equations, were expressed in integral form to facilitate their discretization within a given cell volume V as:

$$\frac{\partial \rho \varphi}{\partial t}V + \sum_f^N \rho_f \vec{V}_f \varphi_f \cdot \vec{A}_f = \sum_f^N \Gamma_\varphi \nabla \varphi_f \cdot \vec{A}_f + S_\varphi V \tag{2.3}$$

where N is number of faces surrounded the target cell, φ_f is convection component of φ through a face, V_f is vector of face velocity, Γ_φ is the diffusion coefficient of φ, A_f is the face area (in 2D it is $|A|=|A_x\ \hat{i} + A_y\ \hat{j}|$), $\nabla \varphi_f$ is facial gradient, and S_φ is the source of φ per unit volume.

To linearize the non-linear terms of Equation 2.3 (Mohammadi et al., 2021), two different coefficients (α_P,and a_{nb}) were used

$$\alpha_P \varphi = \sum_{nb} a_{nb}\varphi_{nb} + b \tag{2.4}$$

where "nb" stands for neighboring cells, and "P" refers to center of the cell. To gain the linearized algebraic equation, Equation 2.4 was applied to all cells.

To discretize the momentum equation, φ was substituted with velocity in the respective momentum equation. For example, the x-momentum equation was demonstrated by substituting φ with the x-velocity component u, as shown in Equation 2.5 (Zhang et al., 2014).

$$\alpha_P u = \sum_{nb} a_{nb}u_{nb} + \sum \rho_f \vec{A} \cdot \hat{i} + S \tag{2.5}$$

where $\vec{A} \cdot \hat{i}$ is the face area, and S is source. In Equation 2.5 if the pressure and mass flux be known, the velocity field can be calculated. If a scalar quantity (i.e., φ) is represented at the center of a cell, the interpolation is needed to calculate that scalar. For pressure, first order upwind scheme was used. Besides, the governing equations were temporally discretized (Equation 2.6).

$$\partial\varphi/\partial t = \frac{3\varphi_i^{n+1} - 4\varphi_i^n + \varphi_i^{n-1}}{2\Delta t} \tag{2.6}$$

Discretization of Continuity Equation

By integrating the Equation 2.2 over the control volume, the discretized continuity equation can be gained.

$$\sum_f J_f A_f = 0 \tag{2.7}$$

where J_f is mass flux through f. The weighted factors obtained from Equation 2.5 were applied using the momentum-weighted averaging-based interpolation scheme, resulting in the normal face velocity ($\vec{v}$). Thus, the face flux can be expressed as:

$$J_f = \rho_f((\alpha_{P,c_0}v_{n,C_0} + \alpha_{P,c_1}v_{n,C_1})/(\alpha_{P,c_0 + \alpha_{P,c_1}}) + d_f((P_{C_0} + (\nabla P)_{c_0} \cdot \vec{r}_0) - (P_{C_1} + (\nabla P)_{c_1} \cdot \vec{r}_1)) = J_f + d_f(P_{C_0} - P_{c_1}) \tag{2.8}$$

where P_{c_0}, and P_{c_1} are pressure components, and v_{n,c_0}, v_{n,c_1} are normal velocity components. Pressures and velocities were defined at the center of a cell, adjacent to the face. $\vec{r}_0$ and $\vec{r}_1$ represent the distances between the faces and the center of the cell, while d_f represents the average of the coefficients α_P in Equation 2.5.

A pressure-based solver was selected to iteratively solve the discretized governing equations. The corrected continuity equation, which accounts for the added pressure condition, was employed in the pressure-velocity coupling. In ANSYS Fluent, there are three options available for solving FSI simulations: coupled solver (simultaneously solves for pressure and momentum), SIMPLE[3] solver (also known as segregated solver, sequentially solves for pressure correction and momentum), and PISO[4] solver (useful for unsteady flow problems or meshes with cells having higher-than-average

---

[3]Semi-Implicit Method for Pressure-Linked Equations
[4]Pressure-Implicit with Splitting of Operators

skewness).

The PISO pressure-velocity coupling scheme, belonging to the SIMPLE algorithm family, employs a higher degree of approximate correlation between the pressure and velocity corrections. In both the SIMPLE and SIMPLEC methods, there is a limitation where the new velocities and corresponding fluxes, obtained after solving the pressure equation, do not satisfy the momentum balance. To address this limitation and enhance calculation efficiency, the PISO algorithm incorporates two additional corrections: neighbor correction and skewness correction (Giannopapa et al., 2004). These corrections help improve the accuracy and stability of the solution.

Neighbor Correction

The PISO algorithm essentially incorporates the iterative calculations required in the SIMPLE and SIMPLEC methods within the solution stage of the pressure equation (Masoomi and Mosavi, 2021). Through one or more iterations, the corrected velocities in PISO ensure satisfaction of the momentum and continuity equations. This iterative process, often referred to as momentum correction or neighbor correction, forms a loop within the PISO algorithm. While PISO may require more CPU time per solver iteration, it has the advantage of significantly reducing the overall number of iterations, particularly in the case of transient problems (Gatin et al., 2017). This can lead to improved computational efficiency in simulations involving unsteady flow phenomena.

Skewness Correction

When dealing with a mesh that exhibits some degree of skewness, the estimated relationship between the mass flux at the cell faces and the pressure at the adjacent cells becomes relatively rough. This is due to the unknown pressure-correction gradient components along the cell faces. To address this issue, an additional iterative process, similar to the neighbor correction, is required (Ejeh et al., 2020).

Once the initial pressure-correction outcome is obtained, the pressure-correction gradient needs to be recalculated, followed by updating the mass flux corrections. This iterative process is referred to as skewness correction. Skewness correction plays a crucial role in mitigating convergence issues associated with highly distorted meshes. In ANSYS Fluent, the incorporation of skewness correction can facilitate the solution for meshes with a higher degree of skewness, improving the accuracy and reliability of the simulation results.

Skewness-Neighbor Coupling

Coupling the neighbor and skewness corrections for meshes with a high degree of skewness, using the same pressure-correction equation, can sometimes lead to divergence or lack of robustness. To address this issue, an alternative approach is to incorporate at least one iteration of skewness correction for every iteration of neighbor correction within the PISO algorithm. This technique allows for a more accurate adjustment of the face mass flux correction based on the pressure correction gradient. The solver continues iterating until the pressure and velocity reach a specified residual value, in this case, 0.0001, indicating convergence. By combining neighbor and skewness corrections in this manner, the solution process becomes more stable and reliable for highly skewed meshes.

Given the dynamic nature of the fluid mesh, smoothing and remeshing techniques were employed. This is necessary because, without remeshing, deteriorated cells could lead to negative cell volumes and convergence problems. To address this issue, an appropriate remeshing strategy was implemented. Additionally, mesh quality was carefully monitored and controlled, particularly with regard to skewness. Controlling of skewness helps ensure the overall quality and reliability of the mesh. By employing smoothing, remeshing, and skewness control, the issues associated with deteriorated cells and convergence problems can be effectively mitigated in dynamic fluid simulations.

35

Structural Domain

The structural field or domain, specifically the solid part, was governed by the momentum equation in Lagrangian form (Equation 2.9).

$$\rho_s \ddot{\vec{d}}_s = \nabla \cdot \overline{\overline{\tau}}_s + \vec{f}_s \tag{2.9}$$

where ρ_s is density of solid, $\vec{d}_s$ is displacement, $\overline{\overline{\tau}}_s$ is stress tensor, and $\vec{f}_s$ is body force per unit volume.

In ANSYS Structural, the finite element method (FEM) is employed to solve for the displacements of the structural field. FEM is used to spatially discretize the principle of virtual work, resulting in the finite element semi-discrete equation of motion. Equation 2.10 represents this semi-discrete equation of motion, which is derived from the application of FEM in ANSYS Structural.

$$\overline{\overline{M}} \ddot{\vec{u}}(t) + \overline{\overline{C}} \dot{\vec{u}}(t) + \overline{\overline{K}} \vec{u}(t) = \vec{F}(t) \tag{2.10}$$

Where $\overline{\overline{M}}$ is mass of solid, $\overline{\overline{C}}$ is structural damping, $\overline{\overline{K}}$ stiffness matrix, $\ddot{\vec{u}}(t)$ is nodal acceleration, $\dot{\vec{u}}(t)$ is nodal velocity, and u(t) is nodal displacement vector, and $\vec{F}(t)$ is external load.

After time-integrating of Equation 2.10 by Newmark method, it can lead to:

$$\overline{\overline{M}} \ddot{\vec{u}}_{n+1} + \overline{\overline{C}} \dot{\vec{u}}_{n+1} + \overline{\overline{K}} \vec{u}_{n+1} = \vec{F}_{n+1} \tag{2.11}$$

where

$$\dot{\vec{u}}_{n+1} = \dot{\vec{u}}_n + [(1-\delta)\ddot{\vec{u}}_n + \delta\ddot{\vec{u}}_{n+1}]\Delta t \tag{2.12}$$

$$u_{n+1} = u_n + \dot{\vec{u}}_n \Delta t + [(\frac{1}{2} - \alpha)\ddot{\vec{u}}_n + \alpha\ddot{\vec{u}}_{n+1}] \tag{2.13}$$

with substituting Equation 2.12 and Equation 2.13 in Equation 2.11, and replacing the integrating parameters of α and δ with a_0-a_7, Equation 2.14 can be written as:

$$(a_0\overline{\overline{M}} + a_1\overline{\overline{C}} + \overline{\overline{K}})\vec{u}_{n+1} = \vec{F}_{n+1} + \overline{\overline{M}}(a_2\vec{u}_n + a_3\dot{\vec{u}}_n + a_4\ddot{\vec{u}}_n) + \overline{\overline{C}}(a_5\vec{u}_n + a_6\dot{\vec{u}}_n + a_7\ddot{\vec{u}}_n) \tag{2.14}$$

As the first step, u_{n+1} was calculated, and its derivatives (velocity and acceleration) can be calculated via Equation 2.15 and Equation 2.16.

$$\dot{\vec{u}}_{n+1} = a_1(\vec{u}_{n+1} - \vec{u}_n) - a_4\dot{\vec{u}}_n - a_5\ddot{\vec{u}}_n \tag{2.15}$$

$$\ddot{\vec{u}}_{n+1} = a_0(\vec{u}_{n+1} - \vec{u}_n) - a_2\dot{\vec{u}}_n - a_3\ddot{\vec{u}}_n \tag{2.16}$$

In each time step, Equation 2.14 to Equation 2.16 must be solved iteratively by applying Newton-Raphson method (Zhou et al., 2022), to achieve convergence.

2.3.4 System Coupling

In ANSYS, the transfer of data between Fluent and Structural is accomplished through System Coupling. Three coupling conditions are imposed to ensure the continuity of data transfer between the solvers and guarantee the following:

- Displacement $d_s = d_f$

- Velocity $\vec{V} = \dot{\vec{d}}$

- Traction $\bar{\bar{\tau}}_s \cdot \hat{n}_s = \bar{\bar{\tau}}_f \cdot \hat{n}_f$

In addition, convergence was checked at each time step. Convergence was considered achieved when the difference between two successive data transfers for both displacement and force was less than 0.001. The end time step was set to 1.2 seconds, covering two cardiac cycles, while the time step size was set to 0.0001 seconds. This approach ensured accurate and stable simulations by monitoring the convergence of the solution throughout the simulation.
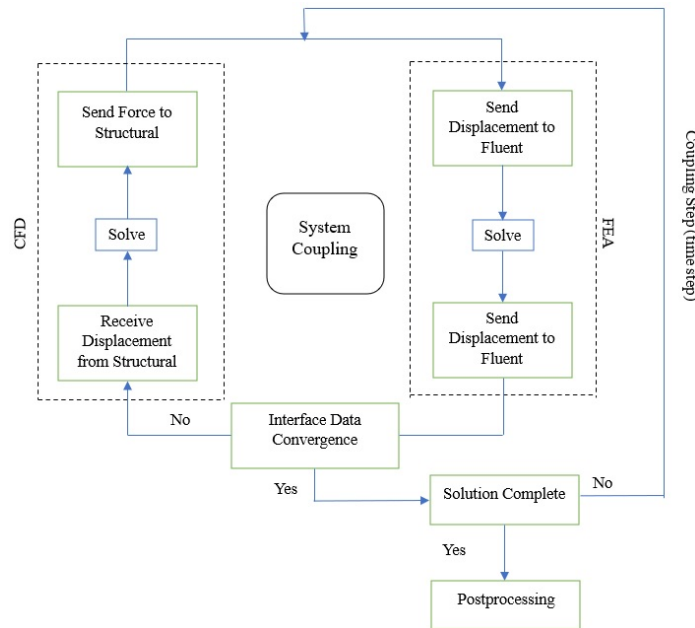
Figure 2.10: *Schematic of two-way FSI in ANSYS*

2.3.5 Hyperelasticity

Hyperelastic or Green elastic materials belong to a special class of materials that exhibit elastic behavior even under large deformations. These materials demonstrate not only nonlinear material behavior but also significant shape changes (Chen et al., 2022). The characteristics that define a hyperelastic material include:

- can undergo large elastic deformations. The initial shape is recovered when the load is removed

- are nearly incompressible, so overall volume remains almost constant

- demonstrate a (highly) nonlinear stress-strain relation

Hyperelastic materials are a class of materials for which a potential function (also known as strain energy density function) exists such that the second Piola-Kirchhoff stress tensor can be defined as the derivative of this potential with respect to the Lagrangian strain tensor.

2.3.5.1 Strain Energy function

To describe the isotropic elastic properties of a hyperelastic material model, strain-energy (stored-energy) function is the best choice. Strain energy function is described as a function of either the invariants of each of the two Cauchy-Green deformation tensors (Areias et al., 2022), or principal stretches . A few different strain-energy formulations exist, having properties and characteristics that make them appropriate for characterizing different hyperelastic material systems. Among the proposed models, for modeling rubber-like materials Ogden, Yeoh, Arruda-Boyce and Gent models have been demonstrated to be quite appropriate (Hackett, 2016).

Ogden Model
The strain energy potential of the Ogden model is based on the principal stretches of the left Cauchy-Green strain tensor. This model serves as a versatile approach for defining rubber, polymer, and biological tissues. Instead of using strain tensor invariants, the principal stretches are employed as the independent variable in this model. The strain energy function is constructed using the principal stretches as independent variables. Mathematically, this model is simple enough for analysis and provides adequate mechanical response for rubber-like solids. Ogden (1972) demonstrated an excellent agreement between the Ogden model and experimental data. In the proposed model, the strain-energy function is a combination of the principal stretches, as Equation 2.17:

$$\Phi = \sum_r \mu_r \Phi(\alpha_r) \tag{2.17}$$

where

$$\Phi(\alpha_r) = (a_1^{\alpha_r} + a_2^{\alpha_r} + a_3^{\alpha_r} - 3)/\alpha_r \tag{2.18}$$

where a_1_a_3 are principal stretches, and μ_r and α_r are material constants. α_r is dimensionless, while μ_r has dimension same as strain (i.e., Pa). If r=1, and $\alpha_1 = 2$, it is equivalent to neo-Hookean model. And if r=2, and $\alpha_1 = 2$, $\alpha_2 = -2$, then the strain energy function can be equal to 2-parameter Mooney-Rivlin model.
In Equation 2.17, the summation is limited to a finite number of terms for practical purposes. However, to ensure consistency with the classical theory, the constants in the equation must satisfy a specific requirement (Equation 2.19, Ogden et al., 2004).

$$\mu_0 = \frac{\sum_{i=1}^N \mu_i \alpha_i}{2} \tag{2.19}$$

where μ_0 is the initial shear moduli. Also, in Equation 2.17 shear bulk modulus is defined as Equation 2.20

$$k_0 = \frac{2}{d_1} \tag{2.20}$$

Curve Fitting
When dealing with experimental data, a challenging issue arises, which involves fitting the data within the framework of elastomer mechanics or thermomechanics. Curve fitting is the process of establishing a mathematical model or curve that best fits the given data points (Shabbir et al., 2020). However, a delicate problem often arises in this process, namely the non-uniqueness of material parameters, which can have a significant impact on the results of boundary-value problems. These issues are inherent to the problem at hand and are generally not dependent on the specific

choice of constitutive law, although in some cases, uniqueness may be achieved.

Furthermore, these issues are not specific to a particular formulation, whether in terms of principal stretches or invariants. For instance, when using polynomial models to obtain a satisfactory fit to data over a wide range of deformations, it becomes crucial to employ high-order polynomials (Esmail et al., 2020). However, this approach can introduce numerical instabilities. Additionally, when the material constants are nonlinear, achieving uniqueness in the optimized set of constants can be challenging unless certain intrinsic properties of the problem are utilized to overcome this non-uniqueness.

For curve fitting of hyperelastic materials, the process typically involves four steps. Firstly, stress-strain data is required as the starting point. Then, an appropriate material model, such as the Ogden 3rd order model, is selected. In the next step, an error criterion is chosen to evaluate the quality of the fit. Finally, a comparison is made between the experimental data and the curve obtained from the fitting process.

The goodness of fit is determined by the fitting method used, which aims to minimize the sum of relative errors. This sum of relative errors is quantified as the residual sum of squares (RSS) and can be calculated as the sum of either relative errors or absolute errors (Equation 2.21 and Equation 2.22, respectively, Ansary-Benam et al., 2021).

$$relative\_RSS = \sum_i (\frac{T^{model} - T^{experimental}}{T^{experimental}})_i^2 \tag{2.21}$$

$$Absolute\_RSS = \sum_i (T^{model} - T^{experimental})_i^2 \tag{2.22}$$

2.3.5.2 Isotropic Hyperelastic Material

Experimental data for a transversely isotropic material typically consists of two curves representing the material response in the 11 and 22 directions. In order to define an isotropic hyperelastic rubber based on this experimental data, Sun and Sacks (2005) proposed the approach of averaging the data from the two perpendicular directions.
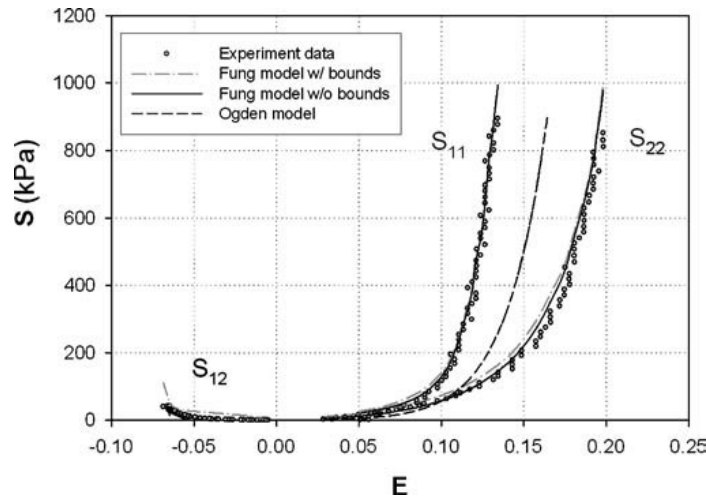

Figure 2.11: *Experimental data, as well as Ogden model of chemically fixed Bovine pericardium (Sun and Sacks, 2005)*

2.4 Summary of Simulation Set up

In summary, the geometry of the valve was reconstructed using μCT image and placed within a designed Aortic Root followed by Ascending Aorta. FSI simulation was conducted using ANSYS.

In ANSYS Fluent, the first step was to generate a mesh throughout the entire fluid domain, representing the main body where blood flows. The mesh size for the main body was set to 8e-4 m to achieve an appropriate balance between computational efficiency and accuracy. To ensure a better-quality mesh, specific face sizings were applied to the contact surfaces with the leaflets. A face sizing of 3e-4 m was used for the leaflet thickness, while a face sizing of 5e-4 m was applied to the walls of the leaflets. To alleviate locking problems, quadratic elements were used.

ANSYS Fluent was used with the k-ω SST model as the viscus model, and the fluid (Blood) was considered as Newtonian. Boundary conditions for this *in silico* study were adopted from Lee et al. (2020), with a defined velocity input and pressure output. The operating pressure was set to 101,325 Pa, equivalent to atmospheric pressure. These boundary conditions ensured the appropriate flow behavior and pressure distribution within the fluid domain during the simulation.
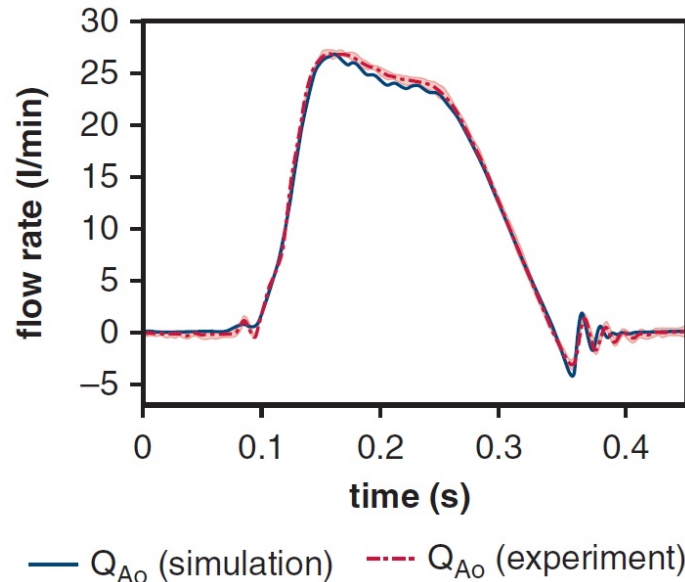
Figure 2.12: *experimental and computational volumetric flowrates of a 21 mm biological aortic valve (Lee et al.)*

Since Lee et al. reported the flow rate in Figure 2.12, the inlet velocity can be calculated using Equation 2.23.

$$Q = A.V \tag{2.23}$$

where Q is the flow rate, A is the cross-section area of the inlet (here assumed cylindrical), and V is the velocity of the flow.

In the normotensive[5] model, the peak systolic velocity was measured to be 0.85 m/s. The duration of one complete cardiac cycle in this study was 0.6 s (Fig. 2.13).

In the context of this study, the faces of the leaflets that face towards the heart are referred to as "in-wall," while the faces that face towards the ascending aorta are referred to as "out-wall."

---

[5]characterized by normal arterial tension or blood pressure

Die approbierte gedruckte Originalversion dieser Diplomarbeit ist an der TU Wien Bibliothek verfügbar

The approved original version of this thesis is available in print at TU Wien Bibliothek.

TU Bibliothek
Your knowledge hub
WIEN
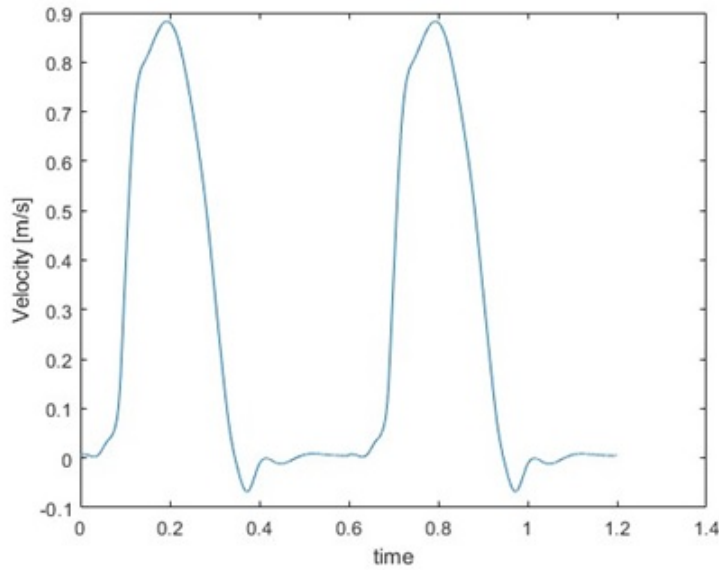
Figure 2.13: *Velocity input in the normotensive model*

Additionally, the thickness of the leaflets is denoted as "thick-wall," as shown in Figure 2.14. These terms are used to distinguish different regions or orientations of the leaflets for analysis and discussion purposes.
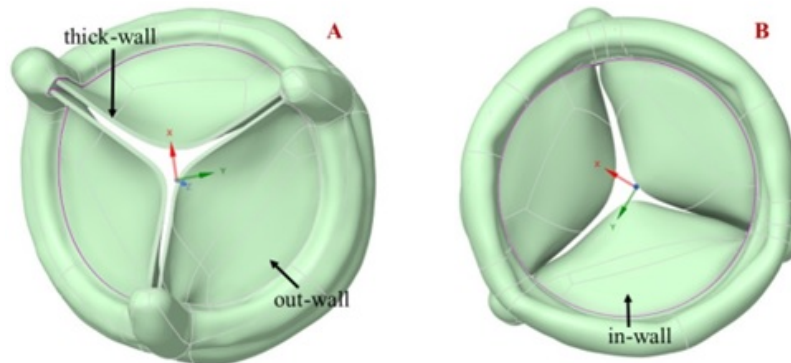
Figure 2.14: *Reconstructed valve for simulation and faces of the leaflets. A) top view, B) bottom view.*

Sinuses in this study were named left-coronary sinus or LC, right-coronary sinus or RC and non-coronary sinus or NC (Figure 2.15).

A deforming mesh and system coupling were set for the contact faces to account for the deformations. The PISO algorithm was chosen as the CFD solver. Residuals were set to 0.0001, which are crucial for achieving convergence. Gravitational forces were neglected as their magnitude is negligible compared to the applied pressure forces.

In Structural two different materials were used for the leaflets and stent. For the leaflets, a transversely isotropic hyperelastic material model based on the Ogden 3rd order formulation was em-

41
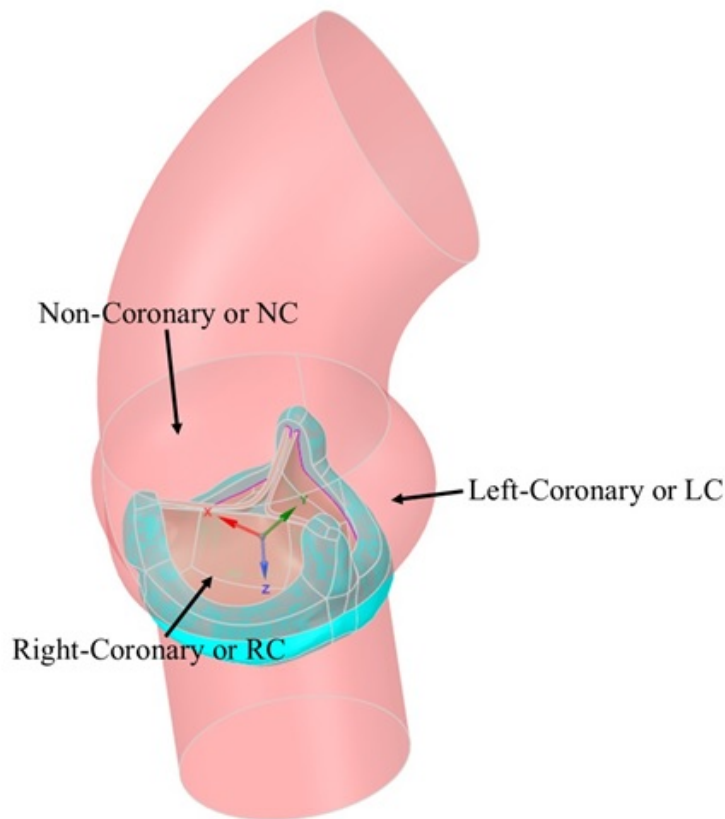
Figure 2.15: *Overall view of the valve, AR and AAo. Sinuses are labeled as LC, RC, and NC.*

ployed, utilizing experimental data from Sun and Sacks (2005). The leaflet material properties were obtained from glutaraldehyde-treated bovine precordium, and the area of interest was determined using SALS. Biaxial mechanical tests were performed, with the x-axis aligned parallel to the direction of fibers and the y-axis perpendicular to it. Stress-strain curves obtained from stretching the bovine fixed pericardium in both x- and y-directions were averaged to define the isotropic hyperelastic material properties (Sun and Sacks, 2005; Wu et al., 2018).

To ensure that the leaflets do not collide during diastole, the internal faces of the leaflets were set as frictionless surfaces with a small offset of 0.0001 m. All the faces of the leaflets in contact with the fluid were defined as system coupling interfaces. Large displacement was enabled due to the hyperelastic nature of the material. The mesh quality in both Fluent and Structural analyses was evaluated using the skewness metric.

In order to facilitate the two-way FSI analysis, System Coupling was employed to transfer the forces from the fluid domain to the structural domain, and the displacements from the structural domain to the fluid domain. This data transfer ensured the necessary coupling between Fluent and Structural solvers. The results obtained from the FSI simulation were then utilized for postprocessing and further analysis.

Chapter 3

Results

The FSI model was simulated for two cardiac cycles. The simulation involved the simultaneous solution of both Fluent and Structural using System Coupling in ANSYS. The solver type used was pressure-based and transient, allowing for accurate representation of the dynamic behavior of the system. Gravitational force was disregarded in the simulation, as it was determined to have a negligible effect compared to the applied pressure forces. The viscous model employed was the k-ω SST model, and the fluid was defined as an incompressible Newtonian fluid with a density of 1060 kg/m^3 and a viscosity of 0.0035 kg/m.s. These settings ensured the accurate representation of the fluid flow and mechanical behavior during the FSI simulation.

In Fluent the total number of elements in the mesh was 449,109, providing a sufficient level of resolution for the simulation. The skewness of the mesh, which indicates the quality of the element shapes, was measured to be 0.828.

In this study, the results were obtained from the second cardiac cycle[1]. Specifically, six target time points were selected for analysis. Three of these points were during the systole, capturing the opening and closing of the valve, including the peak inlet velocity. The remaining three points were during the diastole.

This study, spanning two primary domains, divides its results into two main sections: fluid dynamics and structural analysis.

3.1 Fluid Dynamics

Surgical biological aortic heart valves stand as crucial devices in cardiac interventions due to their durability and hemocompatibility. Understanding the hemodynamics of these valves is essential for assessing their functionality and long-term performance. In this study, particular attention was dedicated to investigating the flow pattern downstream of the surgical biological aortic heart valve. Analyzing the fluid dynamics post-valve deployment sheds light on the intricacies of flow behavior, including factors such as turbulence, shear stress distribution, and recirculation zones. These insights into the flow patterns downstream of the valve contribute significantly to comprehending the hemodynamic characteristics of the prosthetic valve, aiding in optimizing its design for enhanced functionality and minimizing potential complications.

During the systole, the flow at the inlet of the aortic root exhibited a plug flow pattern for the

---

[1]In CFD simulations, the initial conditions can influence the results. By simulating two cardiac cycles, the flow and pressure conditions in the second cycle can be influenced by the state at the end of the first cycle, which provides a better representation of the physiological conditions.

majority of this phase. This means that the flow was relatively uniform and consistent, resembling a plug-like shape as it entered the aortic root. This observation highlights the flow characteristics and behavior during the systolic phase of the cardiac cycle.

3.1.1 Normotensive Valve Hemodynamics

Normotensive valve hemodynamics refer to the flow patterns and dynamics of a healthy heart. These conditions exhibit normal blood flow, with well-coordinated opening and closing of the valve during the cardiac cycle. The velocity profiles and pressure gradients are within the expected range, indicating efficient and smooth functioning of the valve.
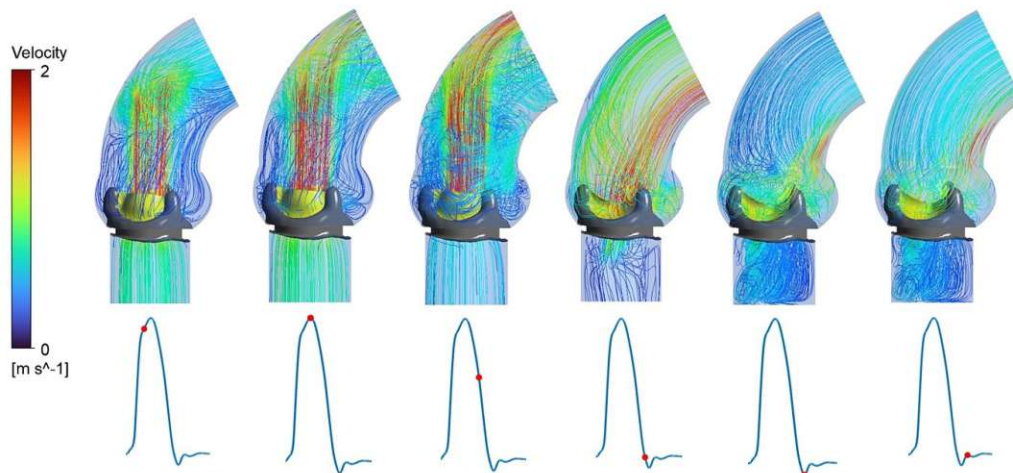
Figure 3.1: *Velocity streamlines during systole and early diastole*

Figure 3.1 depicts the velocity streamlines throughout the cardiac cycle, including systole (both acceleration and deceleration) and early diastole. During the acceleration phase, the transvalvular pressure increased, resulting in the opening of the valve. As the valve opened, the flow velocity through the valve's orifice increased. The maximum opening of the leaflets corresponded to the peak velocity observed during this phase. It is worth noting that during the valve opening, the flow near the sinus region became nearly stagnant. This stagnant flow occurred because the leaflets trapped the flow inside the aortic sinuses.

At the peak velocity, the jet velocity at the orifice of the valve reached 2.6 m/s. This indicates the high-speed flow of blood through the narrowed orifice during the peak flow phase. The measurement of jet velocity provides valuable information about the hemodynamic performance of the valve during systole.

Throughout the acceleration phase, a distinctive plug flow pattern emerged from the valve orifice and persisted for the majority of systole. This pattern indicates that the flow moved cohesively, resembling a coherent mass with a relatively uniform velocity profile. The sustained plug flow signifies the consistent movement of blood with minimal disturbance or mixing, portraying a more uniform velocity distribution within the flow.

The geometry of the AAo exerted a substantial influence on the flow patterns upstream of the valve. The distinctive shape and dimensions of the aorta played a pivotal role in shaping the flow behavior and dynamics near the valve. These geometric characteristics significantly impacted both the stress

distribution on the leaflets and the formation of vorticity within the fluid confined to the AAo. Consequently, the interplay between the AAo geometry and the flow dynamics had discernible effects on the stress experienced by the leaflets and the development of vortices within the aortic environment. The stress distribution on the leaflets pertains to the allocation of forces exerted by the flowing blood across the surface of these structures. The unique geometry of the ascending aorta plays a significant role in influencing these forces, resulting in slight variations in stress distribution across each leaflet. This relationship illustrates how the shape and dimensions of the aorta intricately impact the distribution of forces experienced by the leaflets, leading to nuanced variations in stress distribution throughout the valve structure.

Vorticity denotes the rotational movement exhibited by fluid particles. The geometry of the ascending aorta holds the capacity to exert some influence on the creation and trajectory of vortices within the aortic sinuses. This interaction directly impacts flow characteristics, potentially imparting an influence on the performance of the valve. The manner in which vortices form and maneuver within the aortic sinuses, influenced by the aorta's geometry, becomes a critical factor that can affect the overall fluid dynamics and, consequently, impact the functionality of the valve.

After reaching the peak velocity, during the deceleration phase, a decrease in the orifice jet velocity was observed, which was attributed to the declining transvalvular pressure. The valve closed during diastole as a result of the negative transvalvular pressure and external pressure applied on the leaflets. During systole, a significant increase in the valve's outflow velocity was observed. The axial velocity pattern inside the orifice remained relatively unchanged, indicating a plug flow profile for the jet.

Captured streamlines revealed a pronounced jet flow velocity at the valve orifice and a unidirectional circulatory flow in the sinuses during valve closure. The circulatory flow remained stable and did not reverse direction as the leaflet moved.
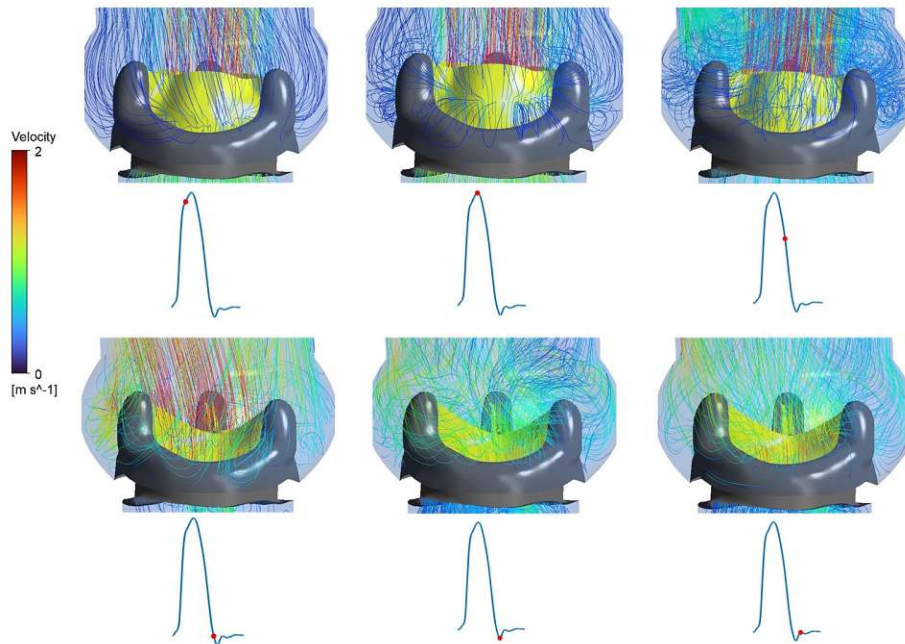
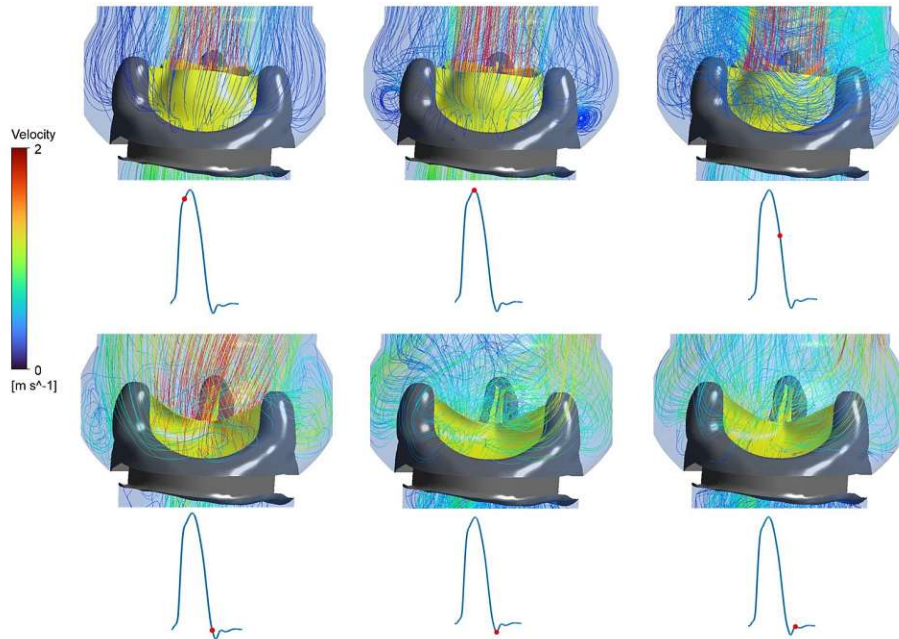Figure 3.2: *Streamlines over Left-Coronary sinus*

Figure 3.3: *Streamlines over Right-Coronary sinus*

Figures 3.2 to 3.4 present streamlines specifically for the LC, RC, and NC regions, respectively. Snapshots were captured during different phases of the cardiac cycle, including acceleration, peak

46
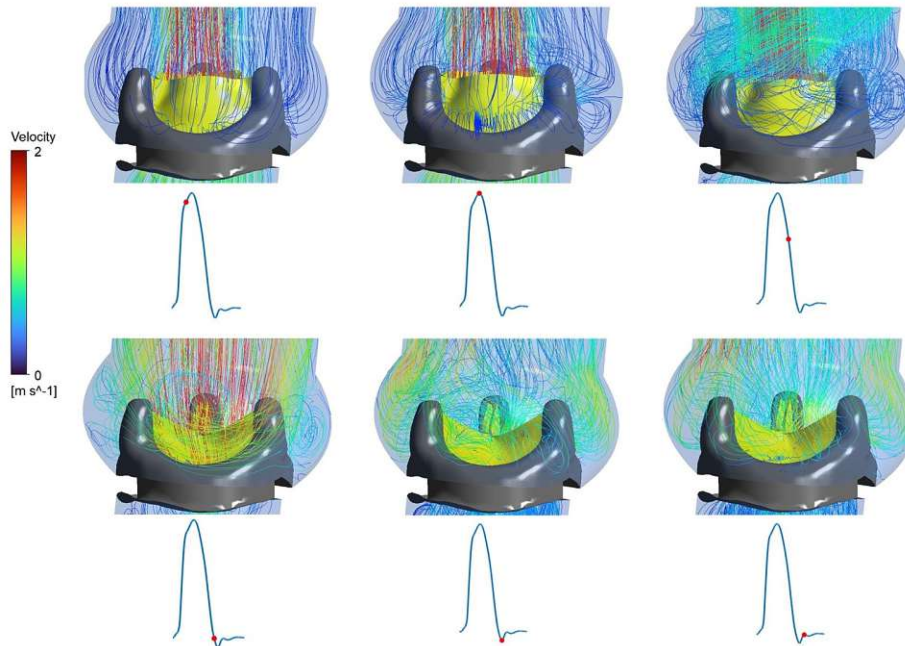
Figure 3.4: *Streamlines over Non-Coronary sinus*

velocity, deceleration, end early diastole. These snapshots provide a detailed visualization of the velocity streamline distribution within each sinus. During early diastole, the velocity increased over the LC, RC, and NC regions and gradually dissipated towards the end of diastole. The highest velocity value, observed on the out-wall, was found over the LC.

3.1.2 Wall Shear Stress

Figures 3.5 to 3.7 present the distribution of wall shear stress (WSS) on the leaflets. Like velocity streamlines, WSS profiles were captured during systole, (acceleration, peak velocity, and deceleration), as well as during diastole. These figures offer valuable insights into the dynamic distribution of wall shear stress experienced by the leaflet surfaces throughout different phases of the cardiac cycle, providing a comprehensive understanding of the mechanical stresses acting on the valve leaflets during the varying hemodynamic conditions.

The bar chart and table in Figure 3.8 show average WSS values for each leaflet at different time points corresponding to the snapshots in Figures 3.5 to 3.7. In the second cardiac cycle, peak inlet velocity occurred at 0.793 S, and end of systole was at 0.946 S, early diastole was 1 S. During acceleration and at peak velocity, regions with highest WSS were tip of (all) leaflets. Besides, at peak velocity there was an increase of WSS in the belly (middle) region too. During deceleration, the highest WSS magnitudes were found at tips and in the middle, while WSS decreased in areas close to the stent. At the beginning of diastole, magnitude of average WSS the highest in all leaflets. Similar to velocity, WSS dissipated during diastole.

At the end of systole (0.946 S) and the beginning of diastole (1 S), the average WSS on LC leaflet was just a bit higher compared to RC and NC leaflets. Moreover, there was a rising trend in the average WSS between 0.946 seconds and 1 second for all three leaflets. The highest magnitude of average WSS was observed at early diastole (1 S), with values of 6.94 Pa, 6.64 Pa, and 2.89 Pa for
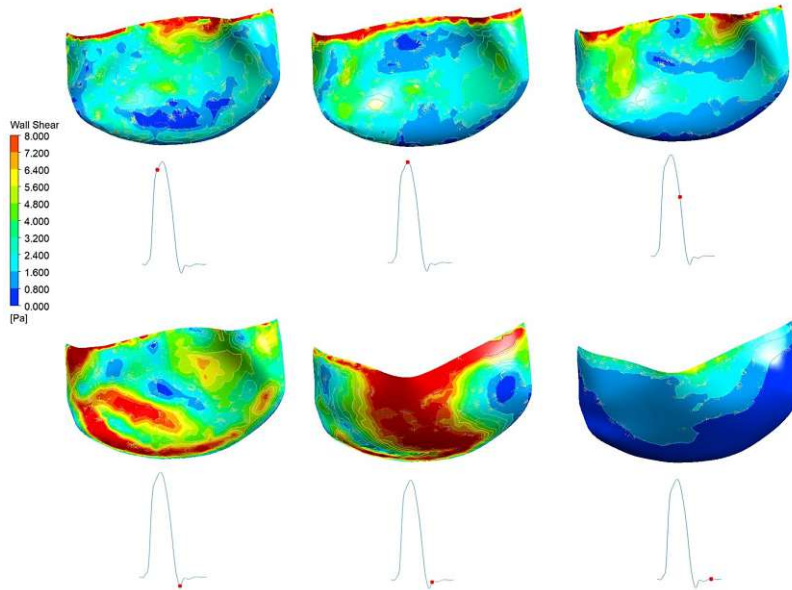
Figure 3.5: *Wall shear stress distribution on the out-wall of the LC*
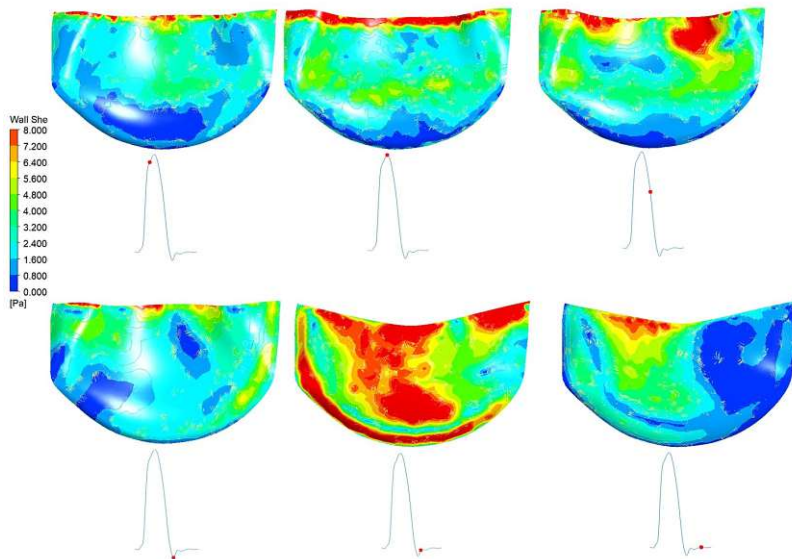
Figure 3.6: *Wall shear stress distribution on the out-wall of the RC*

the LC, RC, and NC leaflets, respectively.

Figures 3.9 to 3.11 illustrate the WSS distribution on the ascending aorta, specifically on the medial and lateral faces, respectively. These figures indicate changes in WSS magnitude in ascending aorta during different phases of the cardiac cycle. During acceleration, WSS values show an increasing trend, starting from the end of the AAo and progressing towards the AR. In the deceleration phase, WSS continues to increase towards the AR. However, during diastole, WSS gradually diminished
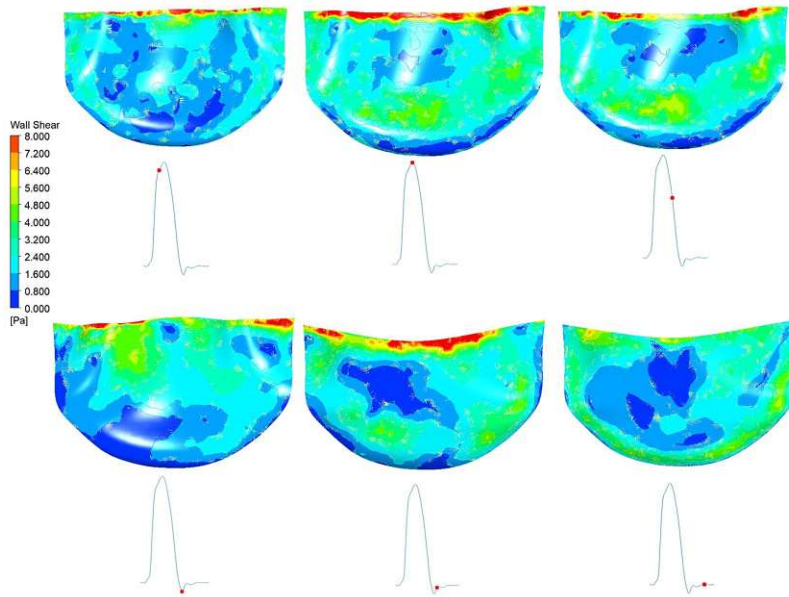
Figure 3.7: *Wall shear stress distribution on the out-wall of the NC*

TIME [S]	LC	RC	NC
0.75	2.97958	2.35553	2.24554
0.793	3.30035	3.87022	3.23303
0.88	3.08939	3.6745	2.83105
0.946	4.94839	2.60845	2.44099
1	6.94458	6.64501	2.89859
1.12	1.23037	2.48315	2.37321
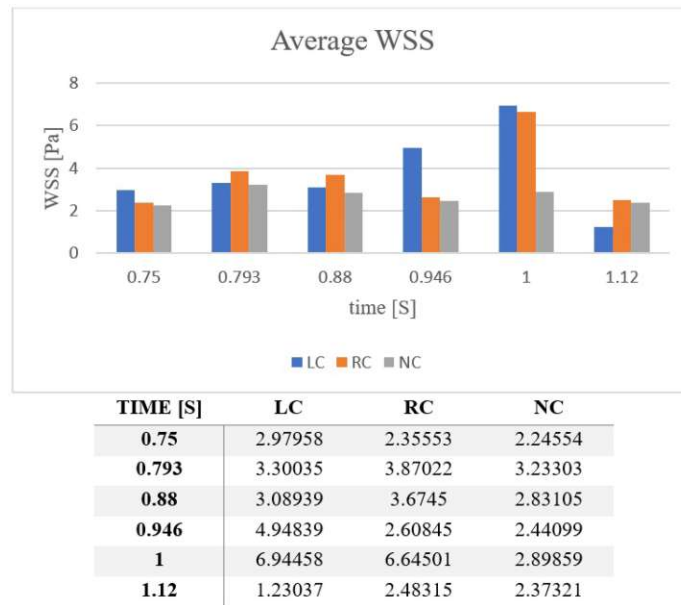
Figure 3.8: *Bar chart and associated data of average WSS [Pa] over out-wall of leaflets*

until it disappeared.
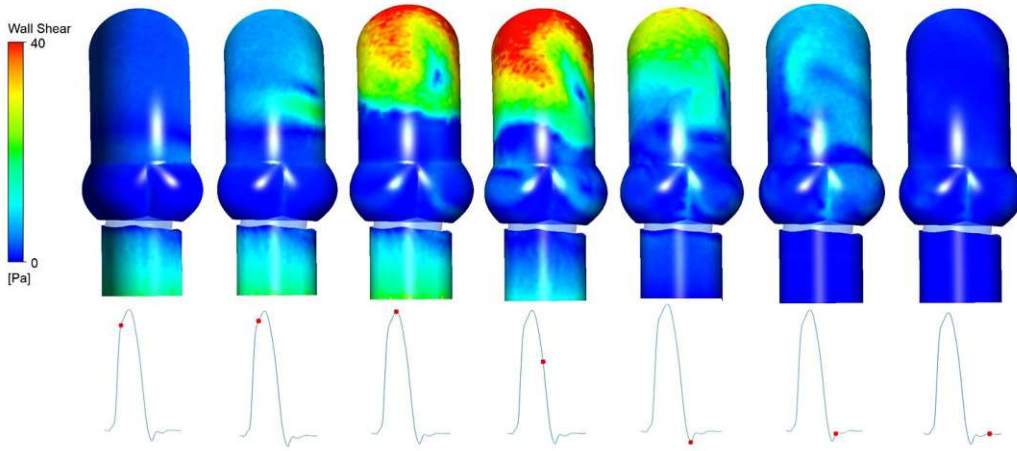
Figure 3.9: *Wall shear stress distribution on the ascending aorta. View, on the medial face.*
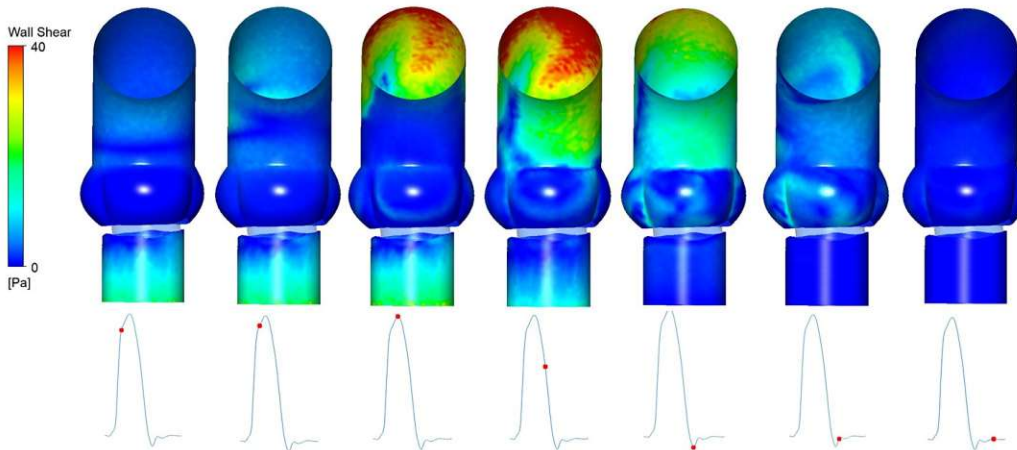
Figure 3.10: *Wall shear stress distribution on the ascending aorta. View, on the lateral face.*

3.1.3 Turbulence Eddy Frequency

The concept of turbulent eddy frequency can be applied to blood flow in the ascending aorta, especially in the context of cardiovascular physiology and biomechanics. Fig.3.12 depicted turbulence eddy frequency in AAo during acceleration, peak inlet velocity, and deceleration. The recorded data revealed turbulent fluid motion with momentary shear strain rates exceeding 2,000 s^{-1}. Shear rates in the AAo reached their highest levels during mid-systole, especially at the moment of peak inlet velocity.
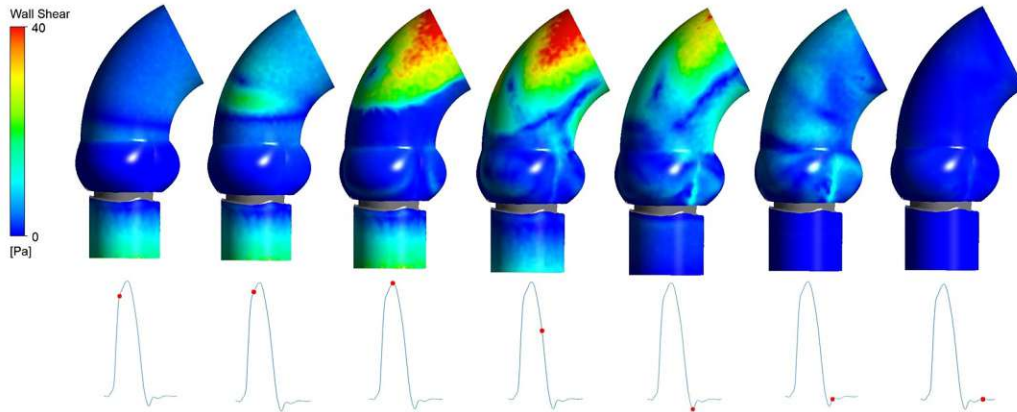
Figure 3.11: *Wall shear stress distribution on the ascending aorta. Side View.*
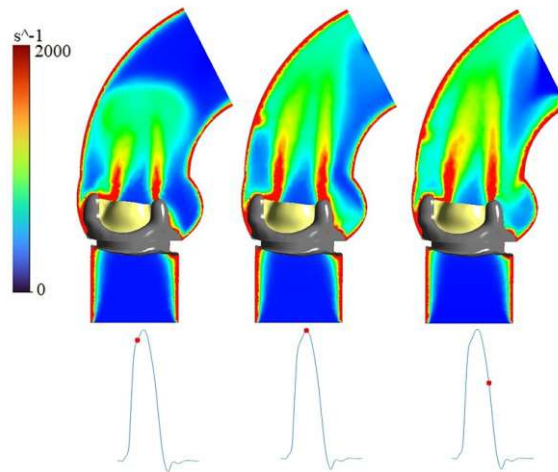
Figure 3.12: *Shear rates in the systolic flow downstream of the biological aortic valve*

3.2 Stress Distribution in Solid Domain

In structural mechanics and material science, stress criteria are pivotal in evaluating the failure or yielding of materials under various loading conditions. Two widely employed stress criteria are the Von Mises criterion and the Maximum Principal Stress criterion, each offering unique perspectives on material failure.

The Von Mises criterion, formulated by Austrian physicist and mathematician Richard von Mises, is extensively used to predict yielding in ductile materials. This criterion is based on the concept that yielding occurs when a specific combination of principal stresses causes the distortion energy to reach a critical value. It suggests that yielding initiates when the Von Mises stress, calculated from the combination of principal stresses, reaches a threshold value for the material. This criterion is especially valuable in scenarios where materials undergo plastic deformation rather than brittle failure. Engineers and researchers often apply the Von Mises criterion in design and analysis to de-

termine the onset of yielding and structural failure in components subjected to complex multiaxial stress states.

On the other hand, the Maximum Principal Stress criterion focuses on identifying failure by comparing the magnitudes of individual principal stresses in a material. According to this criterion, failure occurs when the magnitude of the maximum principal stress reaches or surpasses the material's ultimate strength or yield strength. This criterion is particularly useful in cases where brittle materials or situations involving high stress concentrations need evaluation. While straightforward to apply and interpret, the Maximum Principal Stress criterion may not capture the complete stress state and deformation characteristics, especially in scenarios involving multiaxial loading or complex stress distributions, where the Von Mises criterion tends to provide more accurate failure predictions. Combining these criteria or employing them based on the material behavior and loading conditions allows for a more comprehensive assessment of potential failure mechanisms and aids in designing robust and reliable structures or components.

3.2.1 Von Mises Stress Criterion

As above mentioned, the Von Mises stress criterion is widely used for materials that experience plastic deformation (i.e. heart valve leaflets). It provides a measure of the equivalent stress that would cause yielding in a material. If the material behaves in a plastic or viscoelastic manner, this criterion might be more appropriate (Rassoli et al., 2020).

Distribution of von Mises stress on the leaflets was captured using ANSYS "Transient Structural" and is illustrated in Figure 3.13. The highest magnitude of von Mises stress on the leaflets was recorded at 1.4e+6 Pa, indicating a significant stress level experienced by the leaflet tissue during the simulation.

During both acceleration and deceleration, areas with stress of 2e+5 Pa or higher observed in areas close to the stent, while the lowest stress magnitude was found in areas close to the tip of the leaflets. The highest magnitude of stress occured at the beginning of diastole (at 0.996 S) with the magnitude of 1.4e+6 Pa.

As depicted in Fig. 3.13, the magnitude of the von Mises stress increases during acceleration until reaching the peak inlet velocity. Subsequently, it remains relatively constant until the end of systole. At the onset of diastole, the magnitude of the von Mises stress reaches its maximum. Specifically, at the beginning of diastole (0.96 s) when the input velocity is nearly zero, the von Mises stress intensifies in regions proximal to the stent. It then extends into the belly of the leaflet, resulting in a simultaneous increase in stress magnitude in areas adjacent to the stent. Consequently, larger areas are subjected to this heightened stress level.

These findings provide valuable insights into the stress distribution and mechanical response of the leaflets, shedding light on the dynamic behavior of the valve during the cardiac cycle.

3.2.2 Von Mises Stress on the Leaflets

Figures 3.14 to 3.16 depict the distribution of principal stresses on the LC, RC, and NC leaflets, respectively. While discernible variations in stress patterns are observable across the leaflets, the disparities observed were not deemed significant. Upon qualitative analysis, it is evident that the LC leaflet exhibits the most extensive area characterized by principal stress values of 2e+5 Pa or higher compared to the other two cusps. Following closely, the RC leaflet displays the second-largest region featuring principal stress values exceeding 2e+5 Pa.
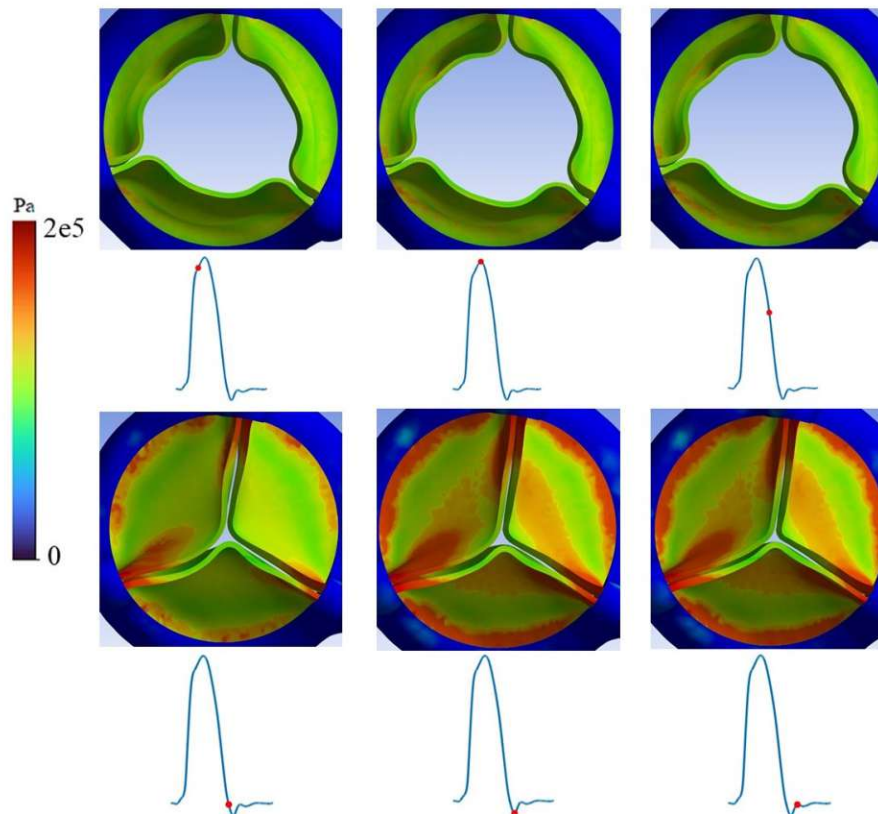
Figure 3.13: *von Mises stress distribution on the leaflets, top view of the valve.*

3.2.3 Maximum Principal Stress Criterion

The maximum principal stress denotes the highest stress value experienced by a material point within a structure. This criterion serves as a valuable tool for pinpointing potential failure areas within a biological valve, especially in regions exhibiting concentrated stress (Abbasi et al., 2016). Similar to the von Mises stress, the maximum principal stress was recorded during acceleration, peak inlet velocity, deceleration, and early diastole.
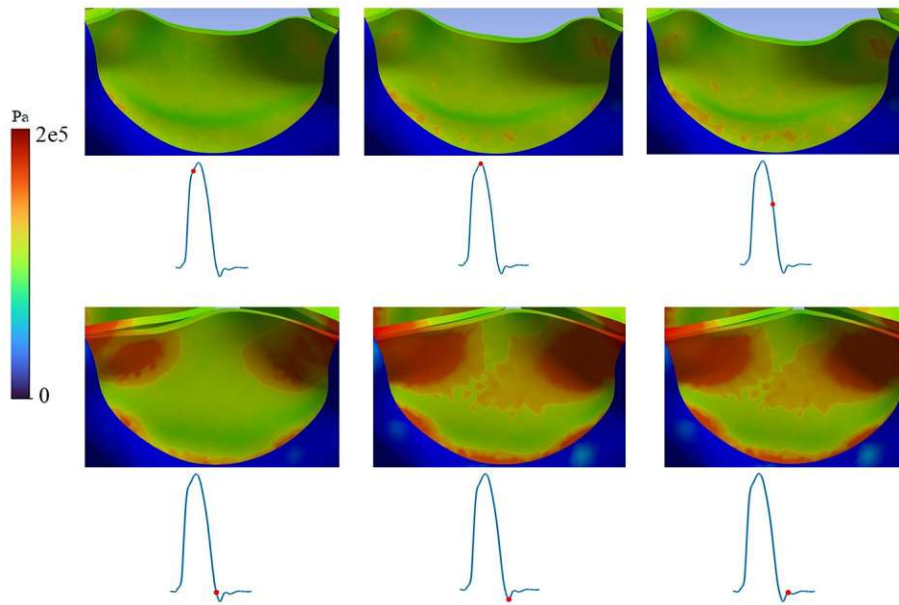
Figure 3.14: *von Mises stress distribution on the LC leaflet*
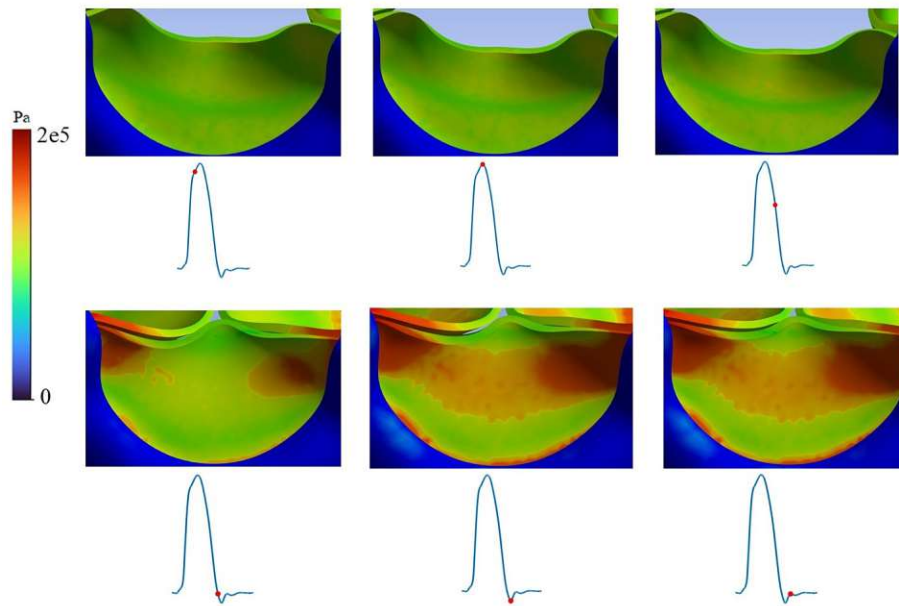
Figure 3.15: *von Mises stress distribution on the RC leaflet*

During both acceleration and deceleration phases, regions experiencing stress levels of 2e+5 Pa or higher, alongside areas encountering stress levels of -1e+5 Pa or lower, were observed in proximity to the stent. Conversely, areas adjacent to the tip of the leaflets exhibited minimal stress. The highest stress magnitude, reaching +3.2e+6 Pa, was notably observed at the onset of diastole (0.996
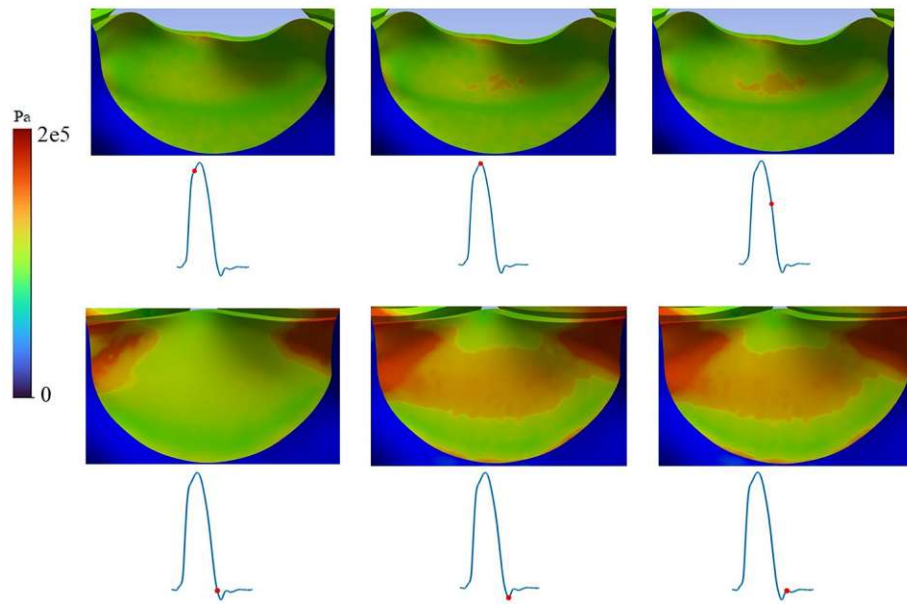
Figure 3.16: *von Mises stress distribution on the NC leaflet*

seconds). This substantial stress magnitude underscores the dynamic stress variations experienced within the valve, particularly at different phases of the cardiac cycle, reflecting the critical stress fluctuations occurring during the diastolic phase.

As illustrated in Figure 3.17, the max. principal stress escalates during the acceleration phase until it reaches its peak at the inlet velocity. Subsequently, it maintains a relatively stable level throughout systole. At the beginning of diastole (0.96 s), when the input velocity approaches zero, the max. principal stress intensifies in regions near the stent and extends into the leaflet's central area. This expansion leads to a simultaneous rise in stress levels in neighboring regions close to the stent, affecting larger areas with heightened stress.

These discoveries offer crucial insights into how stress is distributed across the leaflets and their mechanical response, contributing to a deeper understanding of how the valve dynamically functions during each phase of the cardiac cycle.
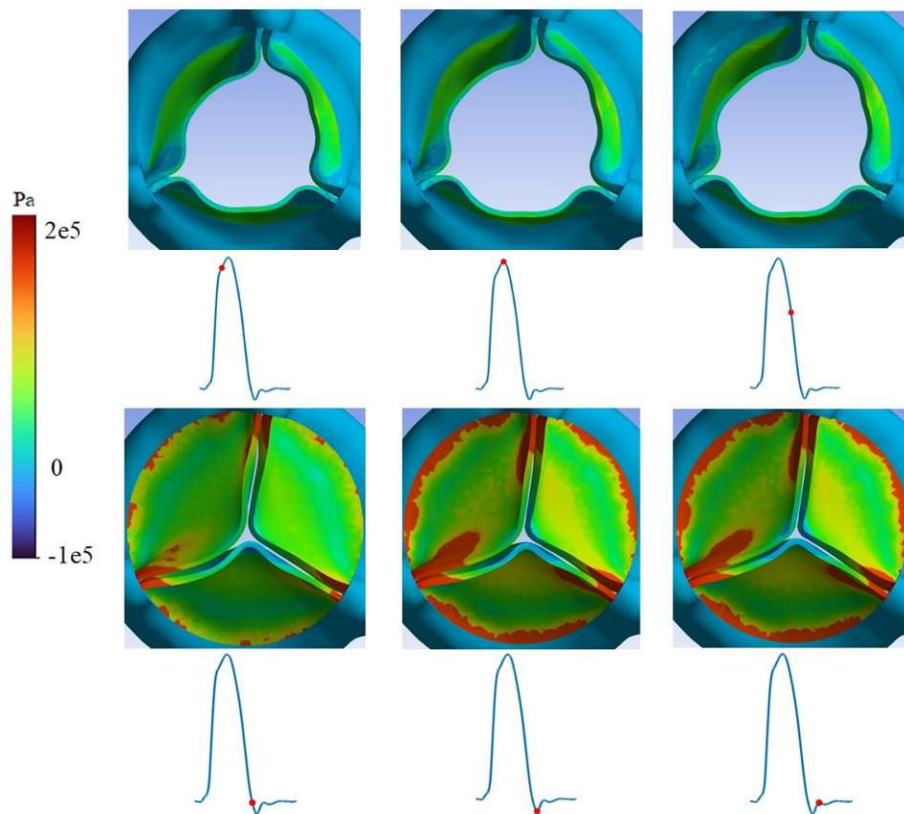
Figure 3.17: *Max. Principal stress distribution on the leaflets, top view*

3.2.4   Max. Principal Stress on the Leaflets

Figures 3.18 to 3.20 showcase the distribution of maximum principal stresses across the LC, RC, and NC leaflets (respectively). While noticeable variations exist in stress patterns among the leaflets, these differences were not deemed statistically significant upon qualitative analysis. Notably, the LC leaflet displays the most extensive area with maximum principal stress values of 2e+5 Pa or higher and -1e+5 Pa or lower compared to the other two cusps. Following this, the RC leaflet demonstrates the second-largest region experiencing the highest stress magnitudes.
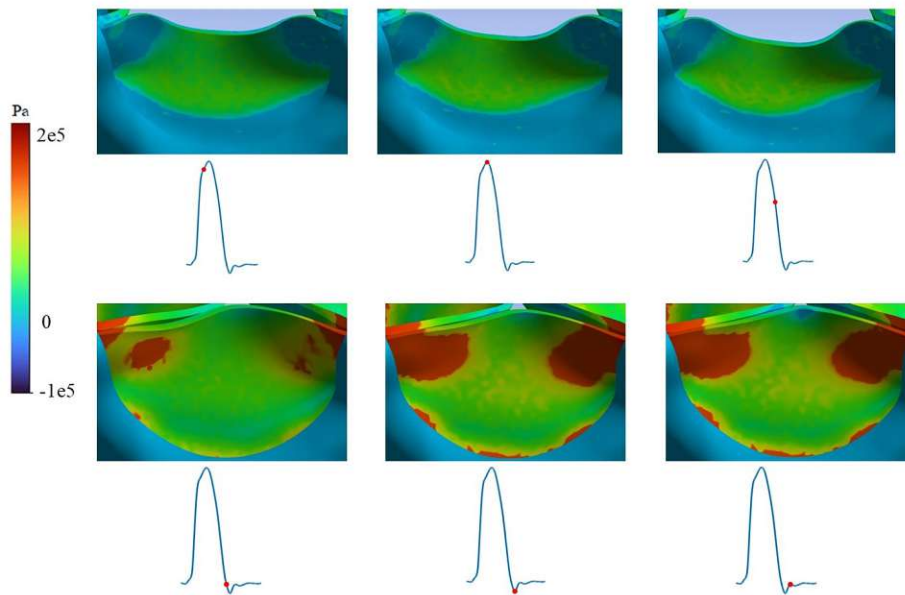
Figure 3.18: *Max. principal stress distribution on the LC leaflet*
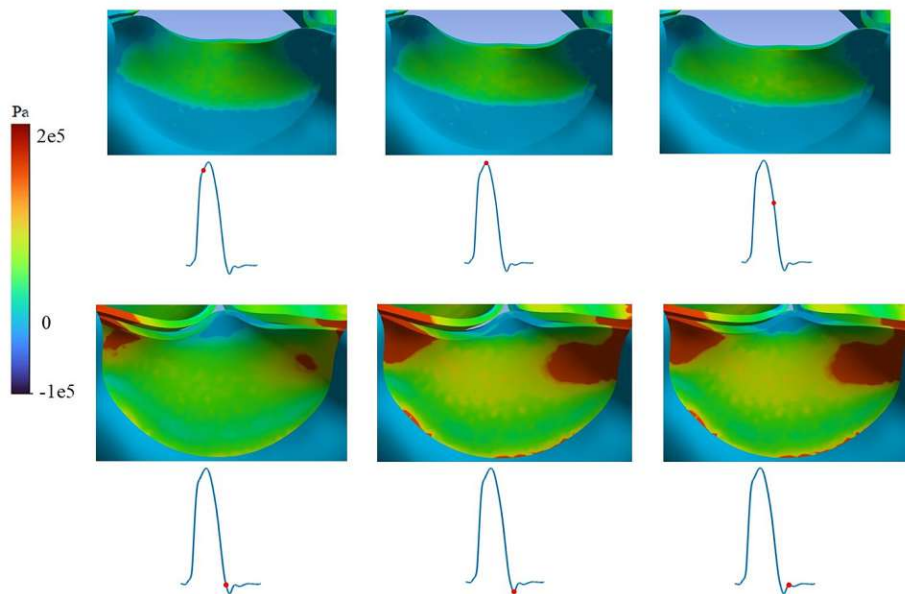
Figure 3.19: *Max. principal stress distribution on the RC leaflet*
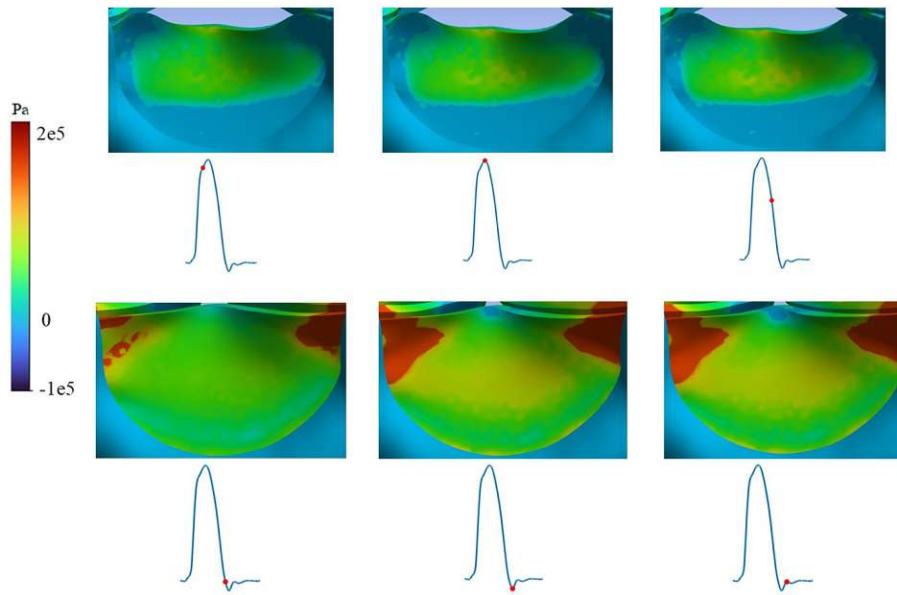
Figure 3.20: *Max. principal stress distribution on the NC leaflet*

3.3 Strain Distribution

Apart from stress, strain is an equally important mechanical factor that offers valuable understanding of the valve's behavior, especially in systole. The strain distribution (von Mises) on the leaflets is depicted in Figure 3.21. In systole when the valve is open, the leaflets undergo intricate movements and fluttering, resulting in stretching.
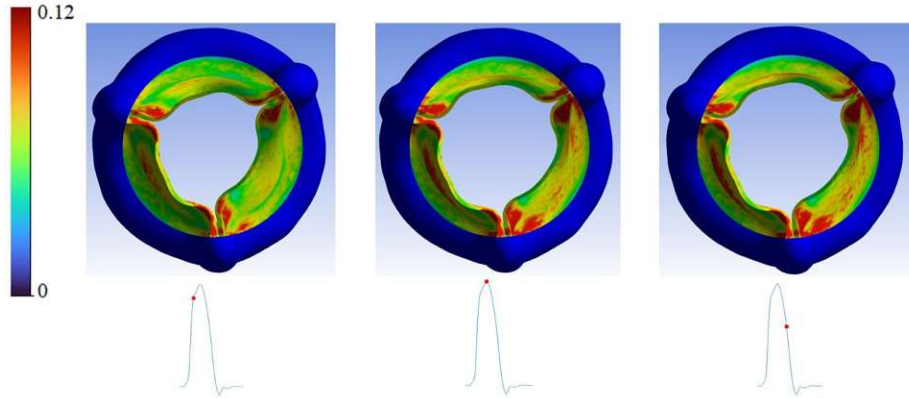
Figure 3.21: *von Mises strain distribution on the leaflets, top view*

3.3.1 Strain Distribution on the Leaflets

Figures 3.22 to 3.24 illustrate the von Mises strain distribution across each leaflet during systole, revealing heightened strain levels near the leaflet tips. Specifically, the belly region and areas proximal to both the tip and stent exhibited significant strain. Strain peaked when the valve was nearly fully opened. Despite minor differences, the LC leaflet displayed the largest high-strain areas, followed closely by the RC leaflet. These findings highlight regions undergoing notable stretching and deformation during the valve's opening and closing cycles, providing valuable insights into the mechanical behavior and potential vulnerability of the valve structure.
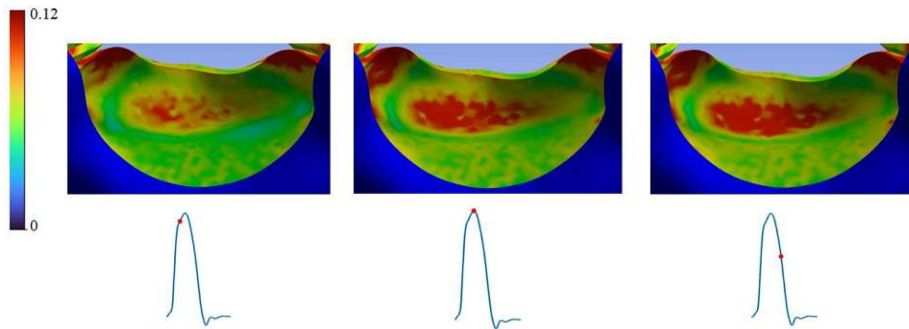
Figure 3.22: *von Mises strain distribution on the LC leaflet*

59
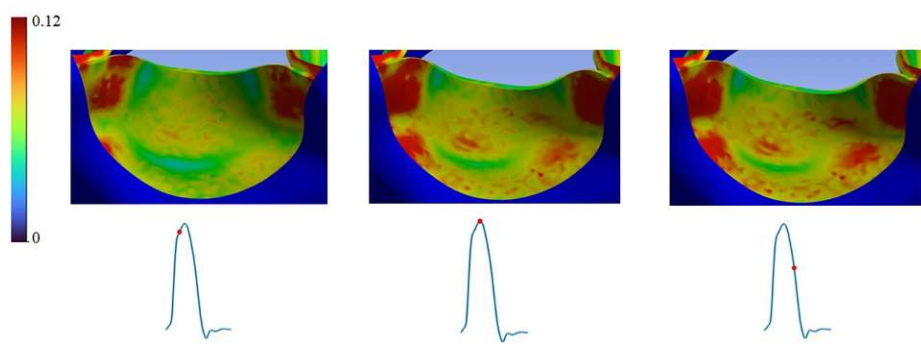
Figure 3.23: *von Mises strain distribution on the RC leaflet*
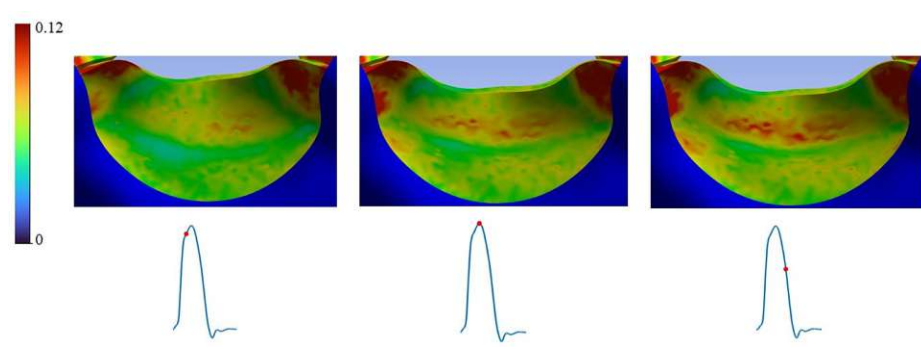
Figure 3.24: *von Mises strain distribution on the NC leaflet*

Chapter 4

Discussion and Conclusion

In this section, the research outcomes encompassing flow characteristics, WSS, and leaflet mechanics are scrutinized alongside pertinent literature to authenticate and place them within context. This comparative analysis aims to thoroughly assess the study's findings, facilitating a more profound comprehension of the valve's behavior. Additionally, the chapter addresses the study's limitations, recognizing any constraints or influencing factors that may have impacted the results. Furthermore, potential avenues for future research and enhancements are proposed, paving the path for further progress in this particular field of investigation.

4.1 Model

The main aim of this research was to create a dependable and thoroughly validated computational model of a surgical aortic valve functioning under normotensive conditions. The purpose behind developing this model was to establish a benchmark for comprehending the mechanical behavior of the valve. To achieve this objective, a two-way FSI simulation was performed, allowing the investigation of both fluid flow characteristics and leaflet dynamics concurrently. By successfully conducting and analyzing the FSI simulation, the study sought to advance the understanding of valvular mechanics in a normotensive state.

4.2 Validation of the Model

To validate the leaflet mechanics in the computational model, several key parameters were utilized, including the effective orifice area (EOA), maximum jet velocity, and maximum strain. These parameters served as important indicators of the mechanical performance and behavior of the valve. By comparing the simulated results with experimental or clinical data, the accuracy and reliability of the computational model were assessed. The EOA provided insights into the extent of valve opening and closing, while the maximum jet velocity reflected the flow characteristics through the valve. Additionally, the maximum strain measurements allowed for the evaluation of the leaflet's deformation and potential for structural damage. Validating these parameters ensured the fidelity of the computational model in capturing the leaflet mechanics of the surgical aortic valve.

The effective orifice area, as depicted in Figure 4.1, holds paramount importance in the assessment of surgical aortic valve replacements' performance. It plays a crucial role in reducing pressure gradients across bioprosthetic valves, thereby contributing to improved clinical outcomes. EOA is defined as

the smallest cross-sectional area of the downstream jet (Garcia and Kadem, 2006).

In this simulation, the EOA was determined by calculating the area formed by the leaflet tips at maximum inlet velocity. CFD-Post was utilized for this purpose. The geometry of the open valve was converted to a 'stl' file format and subsequently processed using SpaceClaim to compute the aforementioned area. The resulting calculated EOA in this study was determined to be 141.54 mm^2. This numerical value holds significant implications for evaluating the valve's functional capacity, signifying its capability to facilitate proper blood flow.
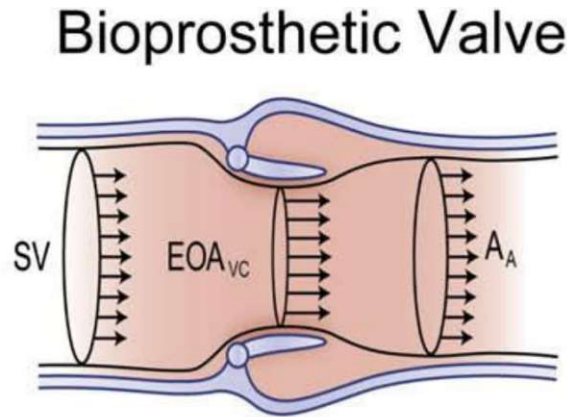
Figure 4.1: *Schematic of EOA*

The comparison of the results obtained in this simulation with findings from previous studies provides strong evidence for the validity of the computational model. Kim et al. (2020) reported an EOA range of 1-2 cm^2 for 21 mm bioprosthetic valves, which closely aligns with the EOA value of 141.54 mm^2 obtained in this study. Similarly, Marx et al. (2019) observed a maximum jet velocity of 2.5 m/s for a 21 mm bioprosthesis, and our simulation demonstrated a slightly higher value of 2.6 m/s.

Regarding wall shear stress, Franke et al. (2022) and Becsek et al. (2020) reported maximum values ranging from 3.57-20.12 Pa, respectively, which closely matches the maximum wall shear stress of 40 Pa obtained in our study. Additionally, Wu et al. (2018) studied strain distribution on surgical aortic valve leaflets and reported a maximum magnitude of 0.444 $[m/m]$, while our study found a similar value of 0.4.

These compelling comparisons demonstrate that the computational model accurately captures essential characteristics of leaflet mechanics and blood flow under normotensive conditions. The model's ability to replicate key parameters validates its reliability and allows for further analysis of leaflet deformation and physiological flow, enhancing our understanding of the valve's behavior and performance.

4.3 Valve Hemodynamics

The investigation of blood flow through the aortic valve, referred to as the hemodynamics of the valve, encompasses the analysis of several crucial parameters. Among these, velocity and EOA are of particular importance. Velocity measurements, such as jet velocity and flow streamlines (as demonstrated in Figure 3.1), offer valuable insights into the flow patterns and the generation of vortices during the acceleration phase.

These parameters play a pivotal role in understanding the dynamics and behavior of blood flow through the aortic valve throughout various phases of the cardiac cycle. By studying velocity profiles and flow patterns, we can gain a comprehensive understanding of how blood moves through the valve, how it accelerates, and how it interacts with the valve leaflets.

The analysis of these critical parameters is instrumental for both researchers and clinicians to gain a comprehensive understanding of the hemodynamics associated with the aortic valve. This analysis yields valuable insights into the valve's performance, efficiency, and potential issues such as turbulence, regurgitation, or stenosis. Moreover, this enhanced understanding significantly contributes to advancing cardiovascular research and plays a pivotal role in guiding the design and evaluation of medical interventions aimed at addressing valvular disorders in patients.

This study's characterization of diastole involved the observation of specific phenomena, including a reduction in valvular flow and the migration of vortices to the sinuses and ascending aorta, followed by their dissipation. These findings are consistent with results reported by Toninato et al. (2016) from an *in vivo* study, which highlighted the downstream migration of vortices within the valve. Similarly, computational studies conducted by Cao et al. (2016) and de Hart et al. (2003) also demonstrated analogous flow characteristics within the valve.

The incorporation of the (more) realistic geometry in our computational model enhances the understanding of diastolic flow behavior, contributing to a more comprehensive analysis of aortic valve hemodynamics. These findings further emphasize the importance of accounting for anatomical nuances in computational simulations to obtain a faithful representation of blood flow patterns in complex cardiovascular systems.
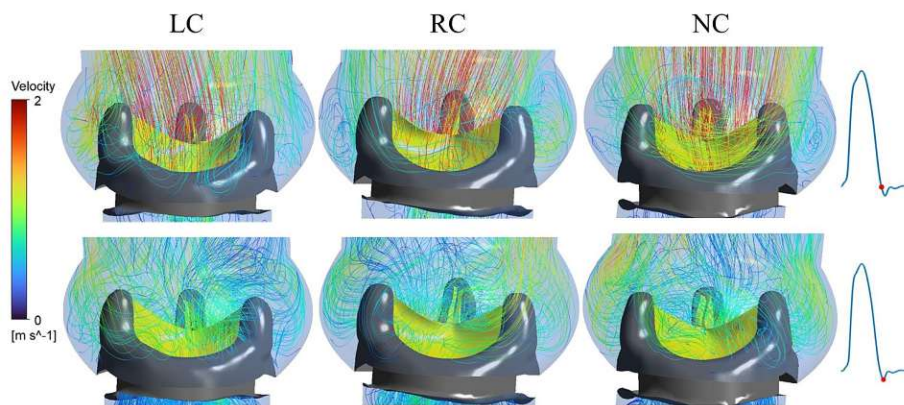
Figure 4.2: *Streamlines over LC, RC, and NC sinuses during early diastole*

Figure 4.2 shows the streamlines over LC, RC, and NC sinuses at early diastole. The observed streamlines in this study reveal a circulatory flow pattern in the sinuses during valve closure. Importantly, this circulatory flow in the sinuses exhibits unidirectional movement and does not exhibit backward motion as the leaflet closes (Figure 4.2). Consequently, the wall shear stress on the leaflets is also unidirectional, lacking oscillatory behavior.

These findings are in line with the results reported by Yep et al. (2012) and Cao et al. (2016), further strengthening the agreement between this study and previous research regarding the unidirectional nature of wall shear stress during valve closure. The consistency between these studies provides robust evidence and enhances the reliability of the present investigation's outcomes.

Understanding the unidirectional flow patterns and wall shear stress during valve closure contributes significantly to the understanding of aortic valve hemodynamics. These insights have implications
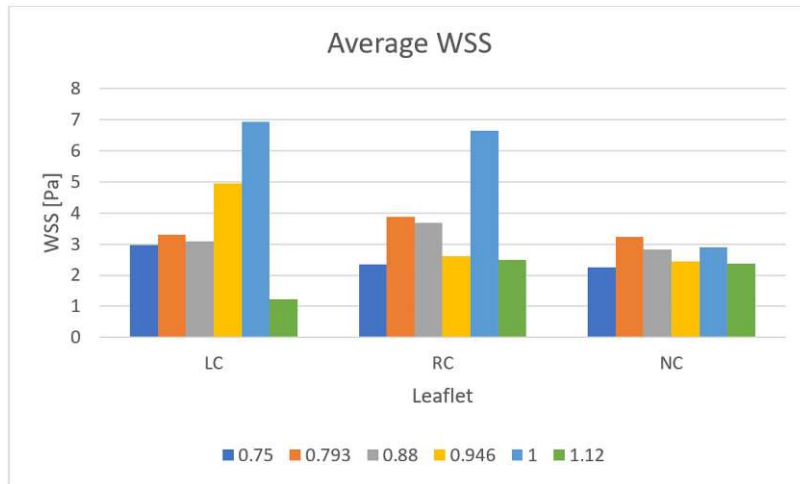
Figure 4.3: *Average WSS over three leaflets before peak velocity (0.75 S), at peak velocity (0.793 S), during deceleration (0.88 S), end of systole (0.946 S), and during diastole (1 S and 1.12 S)*

for the broader field of cardiovascular research, potentially influencing the development of innovative treatment strategies and the design of prosthetic valves for patients with aortic valve-related conditions.

As illustrated in Figure 4.3, the highest magnitude of average wall shear stress is observed at the beginning of diastole (1 S). During this early diastole phase, there is a backward flow around the ascending aorta, and since the valve is fully closed, there is ample space for the fluid to move with less resistance in the sinuses. As a consequence, the average WSS reaches its peak magnitude during early diastole.

Conversely, during late diastole (1.12 S), the blood backflow exhibits a lower velocity magnitude compared to early diastole, leading to the lowest magnitude of average WSS during this period. At the peak inlet velocity (0.793 S), although the velocity magnitude in the ascending aorta is high, the fully open valve restricts the smooth flow of blood into the sinuses. Consequently, the average WSS on the leaflets during this time exhibits a relatively lower magnitude, as depicted in Figure 4.3.

These observations provide valuable insights into the temporal variations of average WSS during different phases of the cardiac cycle. The understanding of WSS patterns is essential in comprehending the mechanical forces acting on the valve leaflets, which can have significant implications for valve function and long-term durability. Such knowledge is valuable for advancing our understanding of aortic valve dynamics and improving the design and performance of prosthetic valves.

During early diastole, the velocity within the sinuses increases and gradually dissipates towards the end of diastole. The highest velocity value is observed on the outer wall, specifically over the LC sinus, as shown in Figure 4.2. However, the difference in velocity between the LC sinus and its counterparts is not notably significant.

This behavior can be attributed to the curvature of the aorta and the influence of the geometric configuration on the flow pattern. The unique shape and orientation of the LC sinus contribute to the slightly higher velocity observed in that region compared to the other sinuses. Nevertheless, the overall velocity distribution among the sinuses exhibits relatively minor variations, indicating that the geometry of the aorta plays a crucial yet subtle role in shaping the flow characteristics.

Understanding these slight variations in velocity distribution is essential for assessing the hemodynamics within the aortic valve and its adjacent structures. The impact of aortic geometry on flow

patterns shed light into the behavior of the valve and its surrounding structures, contributing to a deeper understanding of aortic valve dynamics and potential implications for clinical management. During the acceleration phase, the vorticity of the captured contours downstream of the leaflets exhibited mostly similar patterns. This phase comprised two subphases: the first subphase extended from the beginning of systole until the valve was fully open, while the second subphase occurred when the valve was (almost) fully open.

In the first subphase, as the flow developed downstream, the magnitude of vortices in the sinuses was low. The leaflets were in motion during this phase, gradually opening the valve, and the formation of significant vortices was limited.

In the second subphase, the leaflets blocked most of the inlet area from the ascending aorta to the root of the aorta, resulting in a relatively low magnitude of vortices. Consequently, similar vortices were observed across all sinuses during this phase.

However, during the deceleration phase, the vorticity of the captured contours varied significantly. This variation was due to factors such as leaflet bending and fluttering, flow deceleration, and the geometry effect of the ascending aorta. These vortices played a role in assisting the closure of the valve, contributing to the mechanics of valve closure.

The understanding of vorticity and its dynamics during different phases of the cardiac cycle is crucial for comprehending the hemodynamics of the aortic valve. The work by Moore and Dasi (2014) is relevant in this context and supports the significance of vortices in valve closure dynamics.

The study conducted by Marx et al. (2019) explored the vorticity of streamlines over the aortic valve and the aorta using a design that featured a symmetrical valve, with the root of the aorta assumed to be a sphere. Similar to the current study, the geometry of the ascending aorta and the arc of the aorta in Marx et al.'s research were based on CT data.

An interesting observation made by Marx et al. was that the vortices over the LC sinus were a little higher compared to the other sinuses, a finding that aligns with the results obtained in the present study. This consistency in the findings across both studies suggests a certain level of reliability and agreement regarding the flow dynamics and vorticity patterns in the aortic valve region.

The parallel outcomes between the current study and the work by Marx et al. reinforce the importance of considering realistic anatomical features in computational simulations to accurately depict the flow behavior within the aortic valve and the aorta. Such insights contribute to a deeper understanding of the hemodynamics involved and can potentially influence the development of advanced treatment approaches and prosthetic valve designs.

In this study, the observed wall shear stress on the outer walls of the leaflets was generally of low magnitude. Previous research by Chandra et al. (2012) and Yep et al. (2012) demonstrated that the WSS on the outer wall of the leaflets typically ranged from 0 to 5 Pa. Present study revealed a slightly broader range of WSS values, spanning from 0 to 8 Pa (as shown in Figure 4.3).

It is interesting to note that Chandra et al. also reported an increase in the magnitude of WSS from the base to the tip of the leaflet (from the beginning of systole until early diastole), a trend that is consistent with the findings of this study (as depicted in Figure 3.5 to 3.7). This observation suggests that the distribution of WSS on the leaflets is influenced by their anatomical configuration, which can be critical in understanding the mechanical forces acting on the valve during blood flow. Furthermore, the design of the ascending aorta had to a small degree effect on the distribution of WSS over the leaflets. This effect resulted in a larger area of the LC leaflet experiencing the highest WSS compared to the other leaflets. This finding underscores the significance of considering the realistic geometry of the aorta in computational simulations to more accurately portray the WSS patterns and their implications for valve mechanics.

These results highlight the complex interplay between fluid dynamics and valve geometry in determining the WSS distribution on the leaflets. A deeper understanding of these factors contributes to

advancing our knowledge of aortic valve hemodynamics, with potential implications for diagnosing and managing valvular conditions, as well as guiding the development of novel therapeutic interventions.

The assumption of the ascending aorta as a straight cylinder in the study conducted by Becsek et al. (2020) can indeed lead to differences in the observed WSS distribution compared to the results of the present study. The geometry of the ascending aorta plays a crucial role in shaping blood flow patterns and distribution of WSS. The aorta's actual shape is not a perfect straight cylinder; rather, it has a complex curved and tapering structure. Such anatomical nuances can significantly influence the flow behavior and the distribution of WSS in the aortic region.

By considering a more realistic geometry for the ascending aorta, as done in the current study, the simulation captures more accurately the flow dynamics and the mechanical forces acting on the aortic valve and the surrounding structures. This, in turn, provides more reliable and relevant insights into the hemodynamics of the valve and its physiological implications.

Therefore, it is essential to acknowledge and consider the differences in assumptions regarding the aortic geometry when comparing the results of different studies on WSS distribution. These variations in assumptions can lead to divergent findings and highlight the importance of using patient-specific or realistic anatomical models in computational simulations for a more comprehensive understanding of aortic hemodynamics.

When blood flows through the aorta, it can exhibit turbulent characteristics under certain conditions or in the presence of specific pathologies (Li et al., 2011). Understanding turbulent eddy frequency in the ascending aorta is valuable for assessing its impact on cardiovascular health.

Turbulent Blood Flow: Blood flow in large arteries, including the ascending aorta, is typically laminar, meaning the blood flows smoothly in parallel layers. However, various factors can disrupt this laminar flow, leading to turbulence (Manchester et al., 2022). These factors can include aortic valve diseases (such as aortic stenosis or regurgitation), aortic aneurysms, aortic dissections, or other cardiovascular conditions. Biological valves are recognized for producing turbulent flow within the ascending aorta.

Turbulent Eddy Frequency: In the context of blood flow, turbulent eddy frequency represents the characteristic frequency at which vortices or eddies form and interact within the turbulent flow. This frequency can vary depending on the specific conditions of the flow, such as the severity of valve disease, the geometry of the aorta, and the velocity of blood flow (Katz et al., 2023).

Clinical Significance: The presence of turbulence in the ascending aorta can have clinical significance. For example, turbulent flow can increase the risk of aortic wall damage, promote the formation of atherosclerotic plaques, and lead to elevated shear stresses on the vessel walls (Qiao et al., 2022). Understanding turbulent eddy frequency can provide insights into the forces acting on the aortic wall and help assess the potential for vascular complications.

A turbulent shear layer is created between the outlet velocity of the jet and the slower moving fluid near the vessel wall, as illustrated in Figure 4.4. In their experimental investigations, Hasler et al. (2016) and Hasler and Obrist (2018) utilized three-dimensional particle image velocimetry to examine the flow dynamics around a biological heart valve. The data they collected revealed turbulent flow with instantaneous shear strain rates exceeding 2,000 s^{-1}. It's worth noting that due to the limited resolution of these particle image velocimetry measurements, it's likely that the actual strain rates were even higher than what was recorded. Consequently, these findings suggest that turbulent flow behind biological heart valves may also be a potential trigger for platelet activation.

While Figure 4.4 presents intriguing results, the experimental data from Hasler and Obrist (2018) has its limitations in fully characterizing the turbulent flow field during systolic flow downstream of the biological heart valve. The restricted spatial resolution of the measurements essentially acts as a filter, hindering the precise calculation of turbulent viscous dissipation and wall shear stresses.
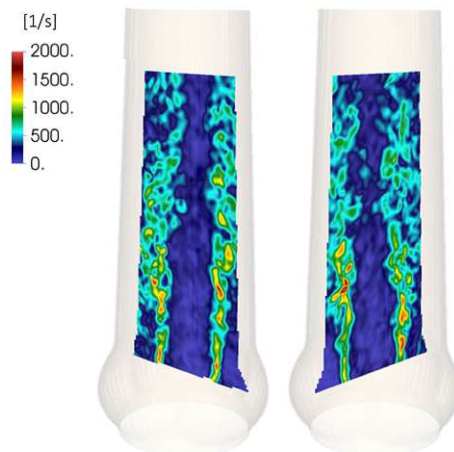
Figure 4.4: *Shear rates in the systolic flow downstream a biological aortic valve (Hasler and Obrist, 2018).*

Additionally, the data's phase-averaged nature makes it challenging to conduct a detailed temporal analysis of flow phenomena. Hence, the current study is focused on offering a more comprehensive understanding of turbulent systolic flow through the use of a computational model.

The results of this study align with the findings of Hasler and Obrist (2018).The results obtained in the current study, as illustrated in Figure 3.12, indicate that turbulent flow in the region downstream of the biological aortic heart valve may have the potential to initiate platelet activation.

4.4 Mechanical Properties

The heart valve's mechanical characteristics play a vital role in its effective functioning, ensuring proper blood flow regulation and prevention of backflow. For the biological heart valve, several essential mechanical properties are noteworthy, such as tensile strength, resistance to fatigue, and tear resistance. Additionally, these mechanical attributes are crucial in guarding against cardiovascular disease.

The main focus of this simulation is to analyze the distribution of von Mises and max. principal stress as well as von Mises strain on the leaflets. Whelan et al. (2021) established a clear link between high strain levels on the leaflets and calcification. Similarly, Stanova et al. (2022) demonstrated that increased mechanical stress on the leaflets can lead to decreased durability of the bioprosthetic valve, although their simulations were based on a porcine biological heart valve.
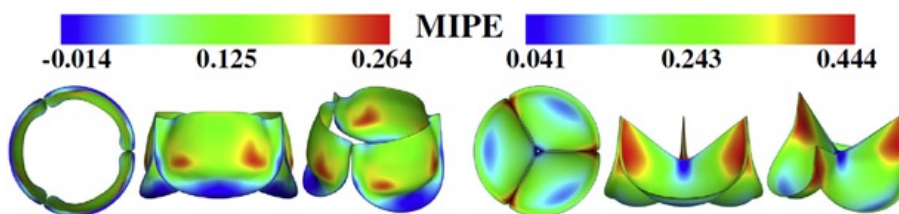
Figure 4.5: *Strain distribution over leaflets in both fully opened and fully closed valve (Wu et al., 2018)*

Wu et al. (2018) conducted a study involving a two-way FSI simulation, where the Aortic Root was
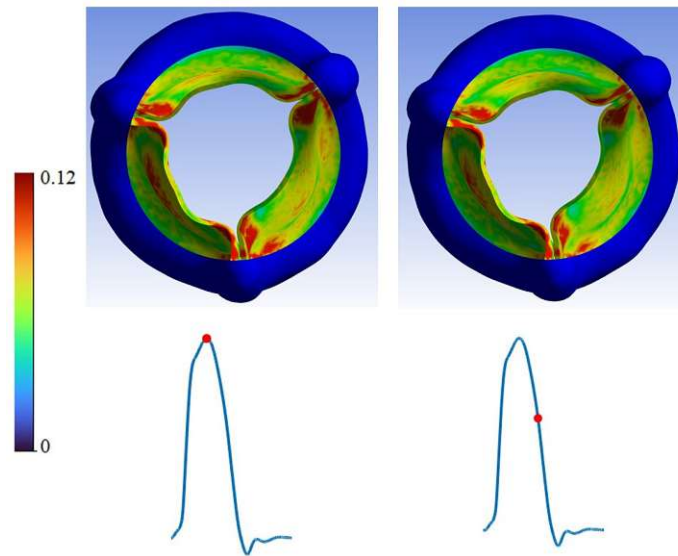
Figure 4.6: *Strain distribution during fully opening of the valve, top view*

represented as a sphere, and the Ascending Aorta as a straight cylinder. The simulation covered the entire domain and focused on analyzing the strain distribution over the leaflets. Because of the symmetrical geometry used in their research, they observed that the strain distribution over the three leaflets also exhibited symmetry, as shown in Figure 4.5.
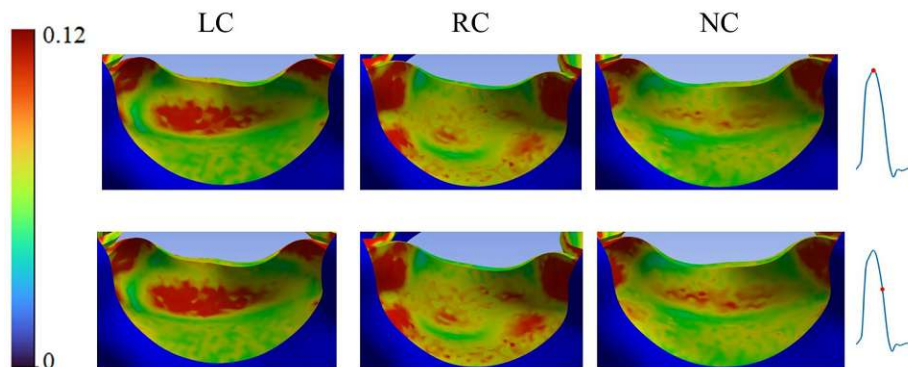
Figure 4.7: *Strain distribution over leaflets while valve is fully open*

This study examined the strain distribution during the fully opening of the valve and discovered (slight) differences across the three leaflets (see Figures 4.6 and 4.7). Nevertheless, it is important to highlight that the strain distribution over cusps exhibited similarity to the results reported by Wu et al., as shown in Figure 4.7.

Alongside strain, the distribution of stress on the leaflets plays a crucial role. Excessive stress imposed on the valve leaflets can lead to damage or deformation, which may contribute to the development of valvular heart disease. Examining the von Mises and maximum principal stress distribution offers valuable information about the mechanical forces acting on the leaflets and allows the identification of regions prone to stress-related damage. This understanding and analysis of stress

distribution empower us and clinicians to gain insights into the mechanical behavior of the leaflets, facilitating the development of strategies to alleviate stress concentrations, enhance durability, and optimize the functioning of biological heart valves.
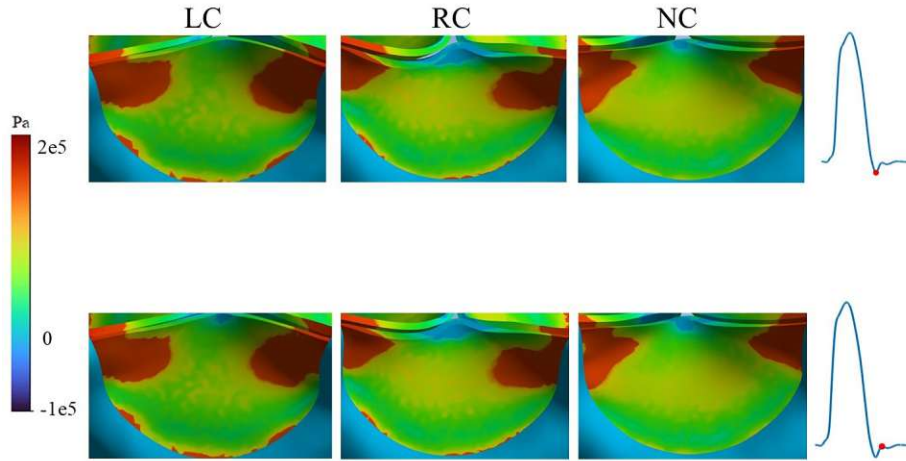
Figure 4.8: *Principal stress distribution over leaflets during early diastole*

Abbasi and Azadani (2020) demonstrated that principal stress near the stent was higher in comparison to the rest of the leaflet. They reported that the highest magnitude of maximum principal stress on the leaflets reached 1.44e+6 Pa, a range similar to the findings reported by Xuan et al. (2020). Particularly, when examining snapshots of the principal stress distribution during peak velocity and deceleration (Figure 4.8), all leaflets exhibited elevated stress levels in areas adjacent to the stent. These observations align with the findings presented by Ghosh et al.
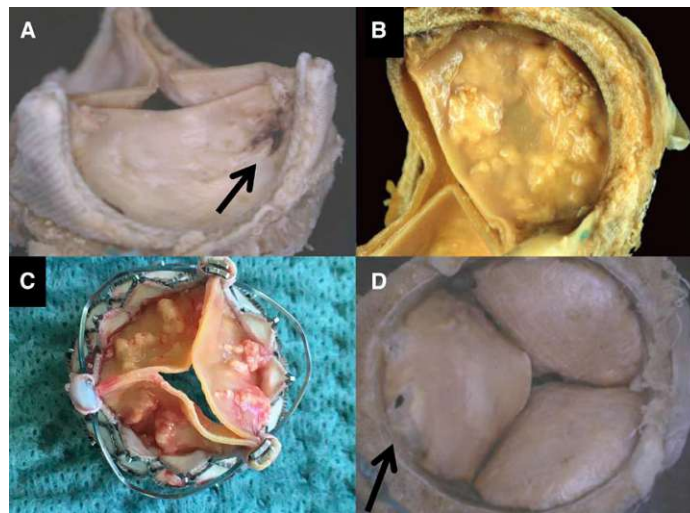
Figure 4.9: *various forms of degeneration that can occur in bioprosthetic heart valves, such as tears and calcification of the leaflets. A, Carpentier-Edwards Perimount valve: leaflet tear. B, Carpentier-Edwards Magna Ease valve: leaflet calcification. C, Engager THV (Medtronic): leaflet restriction and calcification. D, Carpentier-Edwards Perimoun valve: leaflet tear (ventricular side). (Dvir et al., 2018).*

In the study conducted by Dvir et al. (2018), they found that areas in close proximity to the stent of the Carpentier-Edwards Perimount valve were susceptible to tearing (as shown in Figure 4.9). The research highlighted that certain regions near the stent in this valve design were more prone to experiencing tearing or structural damage, which is an important consideration for understanding the durability and performance of such bioprosthetic heart valves.

Figure 4.10: *Photographs of explanted Trifecta valves (Abbott Vascular, Santa Clara, CA) are presented as follows: (A) A 4-year-old Trifecta (27-mm) valve was removed from a 70-year-old man and exhibited severe regurgitation. Notably, a detached cusp with a large tear (indicated by an arrow) was observed at the stent post, between the noncoronary cusp and the right coronary cusp. (B) A 5 1/2-year-old Trifecta (21 mm) valve was explanted from a 58-year-old woman, showing mixed disease. A longitudinal tear (arrow) between the noncoronary and right coronary cusps, accompanied by diffuse cusp fibrosis, was evident. (C) A 6-year-old Trifecta (25 mm) valve was removed from an 80-year-old woman due to severe stenosis (Fukuhara et al., 2020).*

Fukuhara et al. (2020) conducted a dedicated study examining the deterioration of Trifecta aortic valves. According to their results, regions near the stent and the belly of the valve were notably prone to structural valve deterioration (see Figure 4.10). These findings imply that the mechanical stresses and forces acting on these specific areas could play a significant role in contributing to the degradation and deterioration of the Trifecta aortic valve.

Yongue et al. (2021) investigated the failure modes of the Trifecta aortic valve prosthesis, which is a bovine pericardial valve manufactured by Abbott Laboratories (Abbott Park, IL). Their study findings unveiled two significant failure modes: tears in the region surrounding the stent and calcification covering the entire surface of the leaflets. These observations shed light on potential issues that could impact the performance and durability of the Trifecta aortic valve.

The stress distribution analysis in this study demonstrates that the regions adjacent to the stent and the belly of the leaflets encounter the most significant levels of stress. As a result, these specific areas are more vulnerable to tear and calcification. These findings are in complete agreement with previous studies carried out on deteriorated bioprostheses, as evidenced by the works of Dvir et al. (Fig. 4.9), Fukuhara et al. (Fig. 4.10), and Yongue et al. (Fig. 4.11) Together, these studies provide compelling evidence supporting the idea that regions exposed to heightened stress levels are more susceptible to structural damage and calcification in bioprosthetic valves.

Biological heart valves are subjected to cyclic mechanical loading due to the continuous functioning of the heart. Elevated strain and stress magnitudes can induce microstructural damage in the form
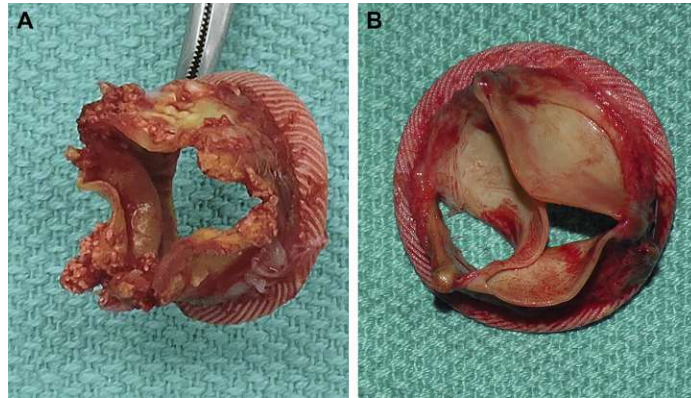
Figure 4.11: *Explanted Trifecta valve (Abbott Laboratories, Abbott Park, IL) demonstrating (A) calcific degeneration and (B) cusp tear (Yongue et al., 2021).*

of micro cracks within the leaflet tissue. Gunning and Murphy (2015) and Qin et al. (2020) have highlighted that the accumulation of micro cracks in the valve leaflets could compromise their structural integrity. These micro cracks may initiate a cascade of events leading to valve dysfunction, characterized by stenosis.

4.5 Model Improvements

The geometry employed in this study was initially derived from Becseck et al. (2020). However, certain modifications were introduced in this study to improve the design's accuracy. While Becseck et al. assumed the ascending aorta to be a straight cylinder, this study utilized a patient's CT image to modify the geometry. As a result, the valve's design in this study achieved a more realistic and precise representation. To conduct the simulation, a μCT scan of the valve was utilized to reconstruct its structure, ensuring a detailed and accurate analysis.
These modifications lead to the following variations:

- Flow streamlines in the AAo were different from the results of Besceck et al, while there was no significant difference in the sinuses.

- During the deceleration, when the leaflets start closing, on the out-wall, vorticity on the leaflets increases, also the average WSS.

- Since the jet flow hits the top portion of AAo, the WSS reaches its highest magnitude in that region followed by developing towards the AR. In deceleration a larger area than the peak velocity has the highest WSS. Like velocity, WSS also dissipated during the diastole.

4.6 Limitations

- The primary constraint of this study pertains to the predefined leaflet material characteristics, which are modeled as isotropic, hyperelastic. However, a limitation arises due to the inherent nature of the pericardial leaflets being transversely isotropic in material properties. The orientation of fibers within these leaflets significantly influences the simulation outcomes, as

highlighted by Wu et al. (2018). Therefore, the exclusion of this transverse isotropy in the model might affect the accuracy and comprehensiveness of the simulation's findings.

- A key limitation inherent in this study pertains to the utilization of a rigid aorta and aortic root. Despite the inherent compliance of these structures, their motion is relatively constrained when contrasted with the markedly dynamic leaflets. Consequently, their influence on sinus hemodynamics is anticipated to be comparatively minor. It's important to acknowledge that this simplified representation might not fully encapsulate the intricate interplay between the aorta, aortic root, and leaflets in terms of their collective impact on the hemodynamic behavior within the sinus.

- Another limitation of this study involves the assumption of symmetrical geometry for the aortic root, disregarding the anatomical reality where the left coronary sinus predominates in size, followed by the right coronary sinus. This simplification, particularly during valve closure, has the potential to directly influence vorticity patterns within the sinuses. As a consequence, the need for future investigations to address and enhance the aortic root design becomes evident.This could lead to inaccuracies in flow patterns and stress distributions. Subsequent studies should delve into refining the representation of aortic root asymmetry to better capture the intricate hemodynamic nuances associated with differing sinus sizes during the cardiac cycle.

- While this study has made significant contributions to our understanding of cardiovascular dynamics, it is essential to acknowledge a notable limitation in our research. Throughout our investigation, the coronary arteries were not included in the scope of our analysis. The coronary arteries play a crucial role in supplying blood to the heart muscle, and their hemodynamic characteristics are of paramount importance. Neglecting this significant component of the circulatory system may result in an incomplete picture of overall cardiovascular function. The blood flow through these arteries is vital, and future studies should strongly consider incorporating them into their analyses. A comprehensive examination of coronary artery hemodynamics would undoubtedly yield valuable insights into the broader context of cardiovascular health and function.

- An inherent limitation of this study pertains to the simplification made regarding the geometry of the ascending aorta. In our analysis, we approximated the ascending aorta as a straight arc-shaped cylinder. However, it is crucial to acknowledge that the actual anatomical structure of the ascending aorta is more complex, exhibiting a three-dimensional curvature in the longitudinal direction. This simplification, while necessary for the scope of our current investigation, does not fully capture the intricacies of the aortic geometry. In future studies, it is imperative to account for this complexity by incorporating a more accurate representation of the ascending aorta's 3D structure. This consideration will lead to a more precise assessment of aortic hemodynamics and contribute to a deeper understanding of the cardiovascular system's behavior.

- While ANSYS is capable of FSI simulations, the coupling between fluid dynamics and structural mechanics introduces additional complexities. The assumption of rigid or simplified valve behavior might not capture the realistic deformation and interactions between the valve leaflets and the blood flow.

- Without experimental data for direct comparison, validating the simulation results becomes difficult. Comparisons with idealized or simplified experimental data might not fully capture the complexity of in vivo conditions.

- Every individual's heart anatomy and valve characteristics vary. Using a generic model might not account for patient-specific variations, potentially limiting the generalizability of the findings to diverse populations.

- The exclusion of gravitational force constitutes a limitation in this study. Nonetheless, it's worth noting that the magnitude of gravitational force, when juxtaposed with the hemodynamic forces stemming from the input blood flow, is inconsequential. While this omission could potentially affect simulations involving certain scenarios, it is rationalized by the relatively minor influence exerted by gravitational forces in comparison to the dominant hemodynamic dynamics within the system.

- Simulating pulsatile blood flow is crucial for mimicking the dynamic behavior of the heart valve. However, replicating the entire cardiac cycle accurately can be challenging due to the complexity of heart mechanics and hemodynamics.

- While simulation studies provide valuable insights, direct clinical translation requires rigorous validation against clinical outcomes. Simulation results might not directly correlate with real-world physiological responses or long-term valve performance.

4.7   Conclusion

In summary, this investigation leveraged a two-way FSI simulation using ANSYS to delve into the intricate hemodynamic and mechanical dynamics of an Avalus bioprosthetic aortic heart valve. The outcomes underscored the nuanced distribution of WSS within the ascending aorta, attributing its asymmetry to the distinctive geometry. Notably, the medial surface of the AAo emerged as a hotspot for heightened WSS values, peaking during acceleration towards the aortic root and tapering during deceleration and diastole. Additionally, the vortical patterns over the sinuses exhibited notable disparities.

From these discernments, it is imperative that future inquiries seeking a comprehensive grasp of the hemodynamic and mechanical attributes of biological heart valves heed the bow-shaped configuration of the AAo, with a bending in the longitudinal direction (a complex 3D structure). It's crucial to bear in mind that for future research, it is strongly advised to include the coronary arteries in the geometric model.

Moreover, this study cast a spotlight on the shortcomings intrinsic to past assumptions of a straight cylindrical AAo in research endeavors. The necessity of accommodating its arc-shaped form to sidestep consequential errors in results was underscored. The indication of backflow at the outlet flagged the aorta's impact on the aortic root, amplifying the call for holistic aortic inclusion: encompassing the ascending aorta, aortic arc, and descending aorta, to veritably encapsulate its influence. In extending insights into the hemodynamics of the left and right coronary arteries, the prescription goes beyond simply embracing the entirety of aortic design; it mandates an overhaul of aortic root representation. Furthermore, an entreaty to scrutinize leaflet fluttering across diverse valve sizes emerges, as it promises richer insights into the complexities of turbulent blood flow. This study, while unveiling key dimensions of valve hemodynamics, beckons the research community to journey deeper into these nuanced intricacies to better inform cardiovascular health and innovation.

Chapter 5

Sources

Abbasi, M., and Azadani, A. N. (2020). A geometry optimization framework for transcatheter heart valve leaflet design. Journal of the mechanical behavior of biomedical materials, 102, 103491.

Abbasi, M., Barakat, M. S., Vahidkhah, K., and Azadani, A. N. (2016). Characterization of three-dimensional anisotropic heart valve tissue mechanical properties using inverse finite element analysis. Journal of the mechanical behavior of biomedical materials, 62, 33-44.

Abramov, A., Xue, Y., Zakharchenko, A., Kurade, M., Soni, R. K., Levy, R. J., and Ferrari, G. (2023). Bioprosthetic heart valve structural degeneration associated with metabolic syndrome: Mitigation with polyoxazoline modification. Proceedings of the National Academy of Sciences, 120(1), e2219054120.

Anderson, R. H., Devine, W. A., Ho, S. Y., Smith, A., and McKay, R. (1991). The myth of the aortic annulus: the anatomy of the subaortic outflow tract. The Annals of thoracic surgery, 52(3), 640-646.

Anssari-Benam, A., Bucchi, A., and Saccomandi, G. (2021). On the central role of the invariant I2 in nonlinear elasticity. International Journal of Engineering Science, 163, 103486.

Areias, P., de Melo, F. Q., and Sikta, J. N. (2022). Anisotropic hyperelastic/plastic behavior on stress-constrained thin structures by iterating on the elastic Cauchy–Green tensor. Thin-Walled Structures, 170, 108512.

Badea CT, Drangova M, Holdsworth DW, Johnson GA. In vivo small-animal imaging using micro-CT and digital subtraction angiography. Phys Med Biol. 2008 Oct 7;53(19):R319-50. doi: 10.1088/0031-9155/53/19/R01. Epub 2008 Aug 29. PMID: 18758005; PMCID: PMC2663796.

Balachandran, K., Sucosky, P., Jo, H., and Yoganathan, A. P. (2009). Elevated cyclic stretch alters matrix remodeling in aortic valve cusps: implications for degenerative aortic valve disease. American Journal of Physiology-Heart and Circulatory Physiology, 296(3), H756-H764.

Balachandran, K., Sucosky, P., and Yoganathan, A. P. (2011). Hemodynamics and mechanobiology of aortic valve inflammation and calcification. International journal of inflammation, 2011.

Becsek B, Pietrasanta L and Obrist D (2020) Turbulent Systolic Flow Downstream of a Bioprosthetic Aortic Valve: Velocity Spectra, Wall Shear Stresses, and Turbulent Dissipation Rates. Front. Physiol. 11:577188. doi: 10.3389/fphys.2020.577188.

Beg, O. A., Beg, T. A., Pattison, J., Inam, O., Kuharat, S., Kadir, A., and Jouri, W. S. (2020, April). Two-way fluid-structure interaction hydroelastic simulation of vibrating membranes with applications in marine engineering using ANSYS fluent FSI. In ICMEAMT 2021: 15th International Conference on Mechanical Engineering, Applied Mechanics and Technology. World Academy of Science, Engineering and Technology (WASET).

Bhushan, S., Huang, X., Li, Y., He, S., Mao, L., Hong, W., and Xiao, Z. (2022). Paravalvular leak after transcatheter aortic valve implantation its incidence, diagnosis, clinical implications, prevention, management, and future perspectives: a review article. Current Problems in Cardiology, 47(10), 100957.

Botsile, E., and Mwita, J. C. (2020). Incidence and risk factors for thromboembolism and major bleeding in patients with mechanical heart valves: a tertiary hospital-based study in Botswana. Cardiovascular Journal of Africa, 31(4), 185-189

Buchlak, Q. D., Milne, M. R., Seah, J., Johnson, A., Samarasinghe, G., Hachey, B., ... and Brotchie, P. (2022). Charting the potential of brain computed tomography deep learning systems. Journal of Clinical Neuroscience, 99, 217-223.

Caforio, A. L., Stewart, J. T., Bonifacio, E., Burke, M., Davies, M. J., McKenna, W. J., and Bottazzo, G. F. (1990). Inappropriate major histocompatibility complex expression on cardiac tissue in dilated cardiomyopathy. Relevance for autoimmunity?. Journal of autoimmunity, 3(2), 187-200.

Cahill, T. J., Khalique, O. K., George, I., and Kodali, S. (2022). Valve thrombosis after transcatheter and surgical aortic valve replacement: incidence and outcomes. The Journal of Thoracic and Cardiovascular Surgery, 163(4), 1309-1315.

Cao, K., Bukač, M., and Sucosky, P. (2016). Three-dimensional macro-scale assessment of regional and temporal wall shear stress characteristics on aortic valve leaflets. Computer methods in biomechanics and biomedical engineering, 19(6), 603-613.

Carpentier A, Lemaigre G, Robert L, et al. Biological factors affecting longterm results of valvular heterografts. J Thorac Cardiovasc Surg 1969; 38:467.

Carrai, P., Camarri, S., Pondrelli, C. R., Gonnelli, S., and Caffarelli, C. (2020). Calcification of cardiac valves in metabolic bone disease: an updated review of clinical studies. Clinical Interventions in Aging, 1085-1095.

Cartier, R., Ranga, A., and Mongrain, R. (2005). Aortic root reconstruction: from principles to numerical modeling. The Canadian journal of cardiology, 21(12), 1071-1076.

Charitos, E. I., and Sievers, H. H. (2013). Anatomy of the aortic root: implications for valve-sparing surgery. Annals of cardiothoracic surgery, 2(1), 53.

Chen, Z., Wang, Y., Wang, S., Huang, H., Tse, K. T., Li, C. Y., and Lin, C. (2022). Decoupling bi-directional fluid–structure interactions by the Koopman theory: Actualizing one-way subcases and the role of crosswind structure motion. Physics of Fluids, 34(9), 095103.

Chester AH, Taylor PM. Molecular and functional characteristics of heart-valve interstitial cells. Philos Trans R Soc Lond B Biol Sci. 2007;362(1484):1437-43.

Choo, S. J., McRae, G., Olomon, J. P., St George, G., Davis, W., Burleson-Bowles, C. L., ... and Duran, C. M. (1999). Aortic root geometry: pattern of differences between leaflets and sinuses of Valsalva. The Journal of Heart Valve Disease, 8(4), 407-415.

Chuong, C. J., and Fung, Y. C. (1983). Three-dimensional stress distribution in arteries.

Cohen, D. J., Kim, D., and Baim, D. S. (1991). Origin of the left main coronary artery from the "non-coronary" sinus of Valsalva. Catheterization and cardiovascular diagnosis, 22(3), 190-192.

Conte, M., Petraglia, L., Campana, P., Gerundo, G., Caruso, A., Grimaldi, M. G., ... and Parisi, V. (2021). The role of inflammation and metabolic risk factors in the pathogenesis of calcific aortic valve stenosis. Aging Clinical and Experimental Research, 33, 1765-1770.

Cribier, A., Eltchaninoff, H., Bash, A., Borenstein, N., Tron, C., Bauer, F., ... and Leon, M. B. (2002). Percutaneous transcatheter implantation of an aortic valve prosthesis for calcific aortic stenosis: first human case description. Circulation, 106(24), 3006-3008.

Cutler EC, Levine SA. Cardiotomy and valvulotomy for mitral stenosis; experimental observations and clinical notes concerning an operated case with recovery. N Engl J Med 1923; 188:1023–1027.

D'Alessandro, C. C., Dimopoulos, A., Andriopoulou, S., Messaris, G. A., Korossis, S., Koutsoukos, P., and Mavrilas, D. (2021). In vitro calcification studies on bioprosthetic and decellularized heart valves under quasi-physiological flow conditions. Bio-Design and Manufacturing, 4(1), 10-21.

DAVID, T. E., ROPCHAN, G. C., and BUTANY, J. W. (1988). Aortic valve replacement with stentless porcine bioprostheses. Journal of Cardiac Surgery, 3(4), 501-505.

de Jaegere, P., de Ronde, M., den Heijer, P., Weger, A., and Baan, J. (2020). The history of transcatheter aortic valve implantation: The role and contribution of an early believer and adopter, the Netherlands. Netherlands Heart Journal, 28(1), 128-135.

Deb, N., Ali, M. S., Mathews, A., Chang, Y. W., and Lacerda, C. M. (2021). Shear type and magnitude affect aortic valve endothelial cell morphology, orientation, and differentiation. Experimental Biology and Medicine, 246(21), 2278-2289.

Deck, J. D. Endothelial cell orientation on aortic valve leaflets. Cardiovascular Research 20, 760–767 (1986).

Della Rocca, F., Sartore, S., Guidolin, D., Bertiplaglia, B., Gerosa, G., Casarotto, D., and Pauletto, P. (2000). Cell composition of the human pulmonary valve: a comparative study with the aortic valve–the VESALIO project. The Annals of thoracic surgery, 70(5), 1594-1600.

Dembistky, W. P., Limmer, K. K., and Adamson, R. M. (2017). Concomitant Cardiac Surgery During VAD Placement: When Is It Too Much?. In Mechanical Circulatory Support in End-Stage Heart Failure (pp. 337-348). Springer, Cham.

Di Vito, A., Donato, A., Presta, I., Mancuso, T., Brunetti, F. S., Mastroroberto, P., ... and Donato, G. (2021). Extracellular matrix in calcific aortic valve disease: architecture, dynamic and perspectives. International Journal of Molecular Sciences, 22(2), 913.

Du, Z., Hu, Y., Ali Buttar, N., and Mahmood, A. (2019). X-ray computed tomography for quality inspection of agricultural products: A review. Food science and nutrition, 7(10), 3146-3160.

Duncan, A., Moat, N., Simonato, M., de Weger, A., Kempfert, J., Eggebrecht, H., ... and Dvir, D. (2019). Outcomes following transcatheter aortic valve replacement for degenerative stentless versus stented bioprostheses. JACC: Cardiovascular Interventions, 12(13), 1256-1263.

Duraes, A. R., de Souza Lima Bitar, Y., Schonhofen, I. S., Travassos, K. S. O., Pereira, L. V., Filho, J. A. L., ... and Roever, L. (2021). Rivaroxaban versus warfarin in patients with mechanical heart valves: open-label, proof-of-concept trial—the RIWA study. American Journal of Cardiovascular Drugs, 21, 363-371.

Durko, A. P., Head, S. J., Pibarot, P., Atluri, P., Bapat, V., Cameron, D. E., ... and De Paulis, R. (2019). Characteristics of surgical prosthetic heart valves and problems around labeling: a document from the European Association for Cardio-Thoracic Surgery (EACTS)—the Society of Thoracic Surgeons (STS)—American Association for Thoracic Surgery (AATS) valve labelling task force. The Journal of thoracic and cardiovascular surgery, 158(4), 1041-1054.

Dvir D, Bourguignon T, Otto CM, Hahn RT, Rosenhek R, Webb JG, Treede H, Sarano ME, Feldman T, Wijeysundera HC, Topilsky Y, Aupart M, Reardon MJ, Mackensen GB, Szeto WY, Kornowski R, Gammie JS, Yoganathan AP, Arbel Y, Borger MA, Simonato M, Reisman M, Makkar RR, Abizaid A, McCabe JM, Dahle G, Aldea GS, Leipsic J, Pibarot P, Moat NE, Mack MJ, Kappetein AP, Leon MB; VIVID (Valve in Valve International Data) Investigators. Standardized Definition of Structural Valve Degeneration for Surgical and Transcatheter Bioprosthetic Aortic Valves. Circulation. 2018 Jan 23;137(4):388-399. doi: 10.1161/CIRCULATIONAHA.117.030729. PMID: 29358344.

Eivazi, H., Tahani, M., Schlatter, P., and Vinuesa, R. (2022). Physics-informed neural networks for solving Reynolds-averaged Navier–Stokes equations. Physics of Fluids, 34(7), 075117.

Ejeh, C., Afgan, I., AlMansob, H., Brantson, E., Fekala, J., Odiator, M., ... and Boah, E. (2020). Computational fluid dynamics for ameliorating oil recovery using silicon-based nanofluids

and ethanol in oil-wet reservoirs. Energy Reports, 6, 3023-3035.

El Hami, A., and Radi, B. (2017). Fluid-structure interactions and uncertainties: ansys and fluent tools (Vol. 6). John Wiley and Sons. PP: 2_5.

Ershkov, S. V., Prosviryakov, E. Y., Burmasheva, N. V., and Christianto, V. (2021). Towards understanding the algorithms for solving the Navier–Stokes equations. Fluid Dynamics Research, 53(4), 044501.

Esmail, J. F., Mohamedmeki, M. Z., and Ajeel, A. E. (2020, July). Using the uniaxial tension test to satisfy the hyperelastic material simulation in ABAQUS. In IOP Conference Series: Materials Science and Engineering (Vol. 888, No. 1, p. 012065). IOP Publishing.

Fatima, B., Mohananey, D., Khan, F. W., Jobanputra, Y., Tummala, R., Banerjee, K., ... and Kapadia, S. (2019). Durability data for bioprosthetic surgical aortic valve: a systematic review. JAMA cardiology, 4(1), 71-80.

Fioretta, E. S., Motta, S. E., Lintas, V., Loerakker, S., Parker, K. K., Baaijens, F. P., ... and Emmert, M. Y. (2021). Next-generation tissue-engineered heart valves with repair, remodelling and regeneration capacity. Nature Reviews Cardiology, 18(2), 92-116.

Franke, B., Schlief, A., Walczak, L., Sündermann, S., Unbehaun, A., Kempfert, J., ... and Goubergrits, L. (2022). Comparison of hemodynamics in biological surgical aortic valve replacement and transcatheter aortic valve implantation—An in-silico study. Artificial Organs.

Fukuhara, S., Shiomi, S., Yang, B., Kim, K., Bolling, S. F., Haft, J., ... and Deeb, G. M. (2020). Early structural valve degeneration of Trifecta bioprosthesis. The Annals of Thoracic Surgery, 109(3), 720-727.

Furugen, M., Watanabe, N., Nishino, S., Kimura, T., Ashikaga, K., Kuriyama, N., and Shibata, Y. (2021). Impact of osteogenic activity on degenerative aortic valve disease in patients with osteoporotic hip fracture. Journal of Cardiology, 78(5), 423-430.

Galvez-Pol, A., McConnell, R., and Kilner, J. M. (2020). Active sampling in visual search is coupled to the cardiac cycle. Cognition, 196, 104149.

Garcia D, Kadem L. What do you mean by aortic valve area: geometric orifice area, effective orifice area, or gorlin area? J Heart Valve Dis. 2006 Sep;15(5):601-8. PMID: 17044363.

Gatin, Inno, Vuko Vukčević, Hrvoje Jasak, and Henrik Rusche. "Enhanced coupling of solid body motion and fluid flow in finite volume framework." Ocean engineering 143 (2017): 295-304.

Geronzi, L., Gasparotti, E., Capellini, K., Cella, U., Groth, C., Porziani, S., ... and Biancolini, M. E. (2021). High fidelity fluid-structure interaction by radial basis functions mesh adaption of moving walls: a workflow applied to an aortic valve. Journal of Computational Science, 51, 101327.

Ghosh, R. P., Marom, G., Rotman, O. M., Slepian, M. J., Prabhakar, S., Horner, M., and Bluestein, D. (2018). Comparative Fluid–Structure Interaction Analysis of Polymeric Transcatheter and Surgical Aortic Valves' Hemodynamics and Structural Mechanics. Journal of biomechanical engineering, 140(12).

Giannopapa, C. G., and Papadakis, G. (2004, January). A new formulation for solids suitable for a unified solution method for fluid-structure interaction problems. In ASME Pressure Vessels and Piping Conference (Vol. 46865, pp. 111-117).

Glaser, N., Jackson, V., Franco-Cereceda, A., and Sartipy, U. (2019). Survival after aortic valve replacement with bovine or porcine valve prostheses: a systematic review and meta-analysis. The Thoracic and Cardiovascular Surgeon, 67(04), 282-290.

Gould, S. T., Srigunapalan, S., Simmons, C. A., and Anseth, K. S. (2013). Hemodynamic and cellular response feedback in calcific aortic valve disease. Circulation research, 113(2), 186-197.

Grim, J. C., Aguado, B. A., Vogt, B. J., Batan, D., Andrichik, C. L., Schroeder, M. E., ... and Anseth, K. S. (2020). Secreted factors from proinflammatory macrophages promote an osteoblast-like phenotype in valvular interstitial cells. Arteriosclerosis, thrombosis, and vascular

biology, 40(11), e296-e308.

Gu, J., Lu, Y., Deng, M., Qiu, M., Tian, Y., Ji, Y., ... and Kong, X. (2019). Inhibition of acetylation of histones 3 and 4 attenuates aortic valve calcification. Experimental and Molecular Medicine, 51(7), 1-14.

Gunning, G. M., and Murphy, B. P. (2015). Characterisation of the fatigue life, dynamic creep and modes of damage accumulation within mitral valve chordae tendineae. Acta Biomaterialia, 24, 193-200.

Ha H, Koo HJ, Huh HK, Kim GB, Kweon J, Kim N, Kim YH, Kang JW, Lim TH, Song JK, Lee SJ, Yang DH. Effect of pannus formation on the prosthetic heart valve: In vitro demonstration using particle image velocimetry. PLoS One. 2018 Jun28;13(6):e0199792. doi: 10.1371/journal.pone.0199792. PMID: 29953485; PMCID: PMC6023143.

Hackett, R.M. (2016). Strain-Energy Functions. In: Hyperelasticity Primer. Springer, Cham. pp 19–25 https://doi.org/10.1007/978-3-319-23273-7_4

Harky, A., Suen, M. M. Y., Wong, C. H. M., Maaliki, A. R., and Bashir, M. (2019). Bioprosthetic Aortic Valve Replacement in¡ 50 Years Old Patients–Where is the Evidence?. Brazilian Journal of Cardiovascular Surgery, 34, 729-738.

Hasler, D., Landolt, A., and Obrist, D. (2016). Tomographic PIV behind a prosthetic heart valve. Experiments in Fluids, 57, 1-13.

Hasler, D., and Obrist, D. (2018). Three-dimensional flow structures past a bio-prosthetic valve in an in-vitro model of the aortic root. PloS one, 13(3), e0194384.

Hatoum, H., Mo, X. M., Crestanello, J. A., and Dasi, L. P. (2019). Modeling of the instantaneous transvalvular pressure gradient in aortic stenosis. Annals of biomedical engineering, 47, 1748-1763.

Hiester ED, Sacks MS. Optimal bovine pericardial tissue selection sites. II. Cartographic analysis. J Biomed Mater Res. 1998 Feb;39(2):215-21. doi: 10.1002/(sici)1097-4636(199802)39:2¡215::aid-jbm7¿3.0.co;2-s. PMID: 9457550.

Hope, T. A., Markl, M., Wigström, L., Alley, M. T., Miller, D. C., and Herfkens, R. J. (2007). Comparison of flow patterns in ascending aortic aneurysms and volunteers using four-dimensional magnetic resonance velocity mapping. Journal of Magnetic Resonance Imaging: An Official Journal of the International Society for Magnetic Resonance in Medicine, 26(6), 1471-1479.

Human, P., Bezuidenhout, D., Aikawa, E., and Zilla, P. (2022). Residual bioprosthetic valve immunogenicity: Forgotten, not lost. Frontiers in Cardiovascular Medicine, 8, 760635.

Iribarne, A., Leavitt, B. J., Robich, M. P., Sardella, G. L., Gelb, D. J., Baribeau, Y. R., ... and Northern New England Cardiovascular Disease Study Group. (2019). Tissue versus mechanical aortic valve replacement in younger patients: a multicenter analysis. The Journal of thoracic and cardiovascular surgery, 158(6), 1529-1538.

Jahanyar J, Aphram G, Munoz DE, et al. Congenital unicuspid aortic valve repair without cusp patch augmentation. J Card Surg. 2022;37:2477-2480. doi:10.1111/jocs.16622

Jamieson WR, Allen P, Miyagishima RT, Gerein AN, Munro AI, Burr LH, Tyers GF. The Carpentier-Edwards standard porcine bioprosthesis. A first-generation tissue valve with excellent long-term clinical performance. J Thorac Cardiovasc Surg. 1990 Mar;99(3):543-61. PMID: 2308373.

Jang, W., Choi, S., Kim, S. H., Yoon, E., Lim, H. G., and Kim, Y. J. (2012). A comparative study on mechanical and biochemical properties of bovine pericardium after single or double crosslinking treatment. Korean circulation journal, 42(3), 154-163.

Jin, L., Guo, G., Jin, W., Lei, Y., and Wang, Y. (2019). Cross-linking methacrylated porcine pericardium by radical polymerization confers enhanced extracellular matrix stability, reduced calcification, and mitigated immune response to bioprosthetic heart valves. ACS biomaterials science and engineering, 5(4), 1822-1832.

78

Johnson, E. L., Wu, M. C., Xu, F., Wiese, N. M., Rajanna, M. R., Herrema, A. J., ... and Hsu, M. C. (2020). Thinner biological tissues induce leaflet flutter in aortic heart valve replacements. Proceedings of the National Academy of Sciences, 117(32), 19007-19016.

Jyothi P, Kamishetty S, Reddy S, Chandra CR. Micro Computed Tomography – Potential Research and Diagnostic Tool in Dentistry. Arch of Dent and Med Res 2016;2(3):43-49.

Karl Degenhardt et al. Rapid 3D Phenotyping of Cardiovascular Development in Mouse Embryos by Micro-CT With Iodine Staining.

Katsi, V., Magkas, N., Antonopoulos, A., Trantalis, G., Toutouzas, K., and Tousoulis, D. (2021). Aortic valve: Anatomy and structure and the role of vasculature in the degenerative process. Acta Cardiologica, 76(4), 335-348.

Katz, S., Caiazzo, A., Moreau, B., Wilbrandt, U., Brüning, J., Goubergrits, L., and John, V. (2023). Impact of turbulence modeling on the simulation of blood flow in aortic coarctation. International Journal for Numerical Methods in Biomedical Engineering, 39(5), e3695.

Keklikoglou, K., Arvanitidis, C., Chatzigeorgiou, G., Chatzinikolaou, E., Karagiannidis, E., Koletsa, T., ... and Vogiatzi, A. (2021). Micro-CT for biological and biomedical studies: a comparison of imaging techniques. Journal of Imaging, 7(9), 172.

Keshishi, M., Fatima, R., Seidman, M. A., Butany, J., Ouzounian, M., and Chung, J. (2023). Comparison of Modes of Failure and Clinical Outcomes Between Explanted Porcine and Bovine Pericardial Bioprosthetic Valves. Cardiovascular Pathology, 107516.

Khalique, O. K., Cavalcante, J. L., Shah, D., Guta, A. C., Zhan, Y., Piazza, N., and Muraru, D. (2019). Multimodality imaging of the tricuspid valve and right heart anatomy. JACC: Cardiovascular Imaging, 12(3), 516-531.

Khoury BM, Bigelow EM, Smith LM, Schlecht SH, Scheller EL, Andarawis-Puri N, Jepsen KJ. The use of nano-computed tomography to enhance musculoskeletal research. Connect Tissue Res. 2015 Apr;56(2):106-19.   Kim, K. M. (2001). Cellular mechanism of calcification and its prevention in glutaraldehyde treated vascular tissue. Zeitschrift für Kardiologie, 90(3), 99-105.

Kim, H. J., Park, S. J., Koo, H. J., Kang, J. W., Yang, D. H., Jung, S. H., ... and Kim, J. B. (2020). Determinants of effective orifice area in aortic valve replacement: anatomic and clinical factors. Journal of Thoracic Disease, 12(5), 1942.

Korossis, S. (2018). Structure-function relationship of heart valves in health and disease. IntechOpen. P 17.

Kostyunin, A. E., Yuzhalin, A. E., Ovcharenko, E. A., and Kutikhin, A. G. (2019). Development of calcific aortic valve disease: do we know enough for new clinical trials?. Journal of molecular and cellular cardiology, 132, 189-209.

Kostyunin, A. E., and Glushkova, T. V. (2020). Expression of matrix metalloproteinases 1, 2, 9, 12 in xenogenic tissues of epoxy-crosslinked bioprosthetic heart valves explanted due to dysfunction. Rossijskij kardiologiceskij zurnal, 25(10), 3978.

Krishna, V. R., Sanaka, S. P., Pardhasaradhi, N., and Rao, B. R. (2022). Hydro-elastic computational analysis of a marine propeller using two-way fluid structure interaction. Journal of Ocean Engineering and Science, 7(3), 280-291.

Kruithof, B. P., van Wijngaarden, A. L., Mousavi Gourabi, B., Hjortnaes, J., Palmen, M., and Ajmone Marsan, N. (2021). Superimposed Tissue Formation in Human Aortic Valve Disease: Differences between Regurgitant and Stenotic Valves. Journal of Cardiovascular Development and Disease, 8(7), 79.

Langdon, S. E., Chernecky, R., Pereira, C. A., Abdulla, D., and Lee, J. M. (1999). Biaxial mechanical/structural effects of equibiaxial strain during crosslinking of bovine pericardial xenograft materials. Biomaterials, 20(2), 137-153.

Lasrado, S. B., Vinoth, R., and Balaji, S. (2022, March). Analysis of Turbulence Impact on

generic 3D Aneurysm models with smooth expansion and contraction for Steady flow conditions. In 2022 Second International Conference on Power, Control and Computing Technologies (ICPC2T) (pp. 1-6). IEEE.

Le Tourneau T, Marechaux S, Vincentelli A, Ennezat PV, Modine T, Polge AS, Fayad G, Prat A, Warembourg H, Deklunder G. Cardiovascular risk factors as predictors of early and late survival after bioprosthetic valve replacement for aortic stenosis. J Heart Valve Dis. 2007 Sep;16(5):483-8.

Lee, J. H., Rygg, A. D., Kolahdouz, E. M., Rossi, S., Retta, S. M., Duraiswamy, N., ... and Griffith, B. E. (2020). Fluid–structure interaction models of bioprosthetic heart valve dynamics in an experimental pulse duplicator. Annals of biomedical engineering, 48, 1475-1490.

Lehmann, S., Jawad, K., Dieterlen, M. T., Hoyer, A., Garbade, J., Davierwala, P., and Borger, M. A. (2021). Durability and clinical experience using a bovine pericardial prosthetic aortic valve. The Journal of Thoracic and Cardiovascular Surgery, 161(5), 1742-1749.

Leinan, P. R., Grønli, T., Skjetne, P., Wigen, M. S., Urheim, S., Lovstakken, L., and Dahl, S. K. (2022). Comparison of ultrasound vector flow imaging and CFD simulations with PIV measurements of flow in a left ventricular outflow trackt phantom-Implications for clinical use and in silico studies. Computers in Biology and Medicine, 146, 105358.

Lenchik, L., Heacock, L., Weaver, A. A., Boutin, R. D., Cook, T. S., Itri, J., ... and Narayana, P. A. (2019). Automated segmentation of tissues using CT and MRI: a systematic review. Academic radiology, 26(12), 1695-1706.

Leopold, J. A. (2012). Cellular mechanisms of aortic valve calcification. Circulation: Cardiovascular Interventions, 5(4), 605-614.

Li, C. P., Chen, S. F., Lo, C. W., and Lu, P. C. (2011). Turbulence characteristics downstream of a new trileaflet mechanical heart valve. ASAIO Journal, 57(3), 188-196.

Li M. (2020). Chest CT features and their role in COVID-19. Radiology of infectious diseases (Beijing, China), 10.1016/j.jrid.2020.04.001. Advance online publication.

Li, T., Liu, C., and Wang, D. (2020). Applying micro-computed tomography (micro-CT) and Raman spectroscopy for non-invasive characterization of coating and coating pigments on ancient Chinese papers. Heritage Science, 8(1), 1-16.

Liesenborghs, L., Meyers, S., Vanassche, T., and Verhamme, P. (2020). Coagulation: At the heart of infective endocarditis. Journal of Thrombosis and Haemostasis, 18(5), 995-1008.

Liguori, C., Frauenfelder, G., Massaroni, C., Saccomandi, P., Giurazza, F., Pitocco, F., Marano, R., and Schena, E. (2015). Emerging clinical applications of computed tomography. Medical devices (Auckland, N.Z.), 8, 265–278.

Lillehei CW, Gott VL, Dewall RA, Varco RL. Surgical correction of pure mitral valve insufficiency by annuloplasty under direct vision. Lancet 1957; 77:446–449.

Liu, A. C., Joag, V. R., and Gotlieb, A. I. (2007). The emerging role of valve interstitial cell phenotypes in regulating heart valve pathobiology. The American journal of pathology, 171(5), 1407-1418.

Lopes, D., Agujetas, R., Puga, H., Teixeira, J., Lima, R., Alejo, J. P., and Ferrera, C. (2021). Analysis of finite element and finite volume methods for fluid-structure interaction simulation of blood flow in a real stenosed artery. International Journal of Mechanical Sciences, 207, 106650.

Lucy A. Walton et al. Morphological Characterisation of Unstained and Intact Tissue Microarchitecture by X-ray Computed Micro- and Nano-Tomography. Nature. DOI: 10.1038/srep10074 (2015).

Mackman, N. (2012). New insights into the mechanisms of venous thrombosis. The Journal of clinical investigation, 122(7), 2331-2336.

Mahjoub H, Mathieu P, Larose E, Dahou A, Sénéchal M, Dumesnil JG, Després JP, Pibarot P. Determinants of aortic bioprosthetic valve calcification assessed by multidetector CT. Heart. 2015

Mar;101(6):472-7. doi: 10.1136/heartjnl-2014-306445.

Mahler, G. J., Frendl, C. M., Cao, Q., and Butcher, J. T. (2014). Effects of shear stress pattern and magnitude on mesenchymal transformation and invasion of aortic valve endothelial cells. Biotechnology and bioengineering, 111(11), 2326-2337.

Manchester, E. L., Pirola, S., Salmasi, M. Y., O'Regan, D. P., Athanasiou, T., and Xu, X. Y. (2022). Evaluation of computational methodologies for accurate prediction of wall shear stress and turbulence parameters in a patient-specific aorta. Frontiers in Bioengineering and Biotechnology, 10, 836611.

Marro, M., Kossar, A. P., Xue, Y., Frasca, A., Levy, R. J., and Ferrari, G. (2021). Noncalcific mechanisms of bioprosthetic structural valve degeneration. Journal of the American Heart Association, 10(3), e018921.

Marx, P., Kowalczyk, W., Demircioglu, A., Shehada, S. E., Wendta, H., Mourad, F., ... and Wendt, D. (2020). An in vitro comparison of flow dynamics of the Magna Ease and the Trifecta prostheses. Minimally Invasive Therapy and Allied Technologies, 29(2), 78-85.

Masoomi, M., and Mosavi, A. (2021). The One-Way FSI Method Based on RANS-FEM for the Open Water Test of a Marine Propeller at the Different Loading Conditions. Journal of Marine Science and Engineering, 9(4), 351.

Meyer, S., Windisch, T., Perl, A., Dzibela, D., Marzilger, R., Witt, N., ... and Mutschler, C. (2021). Contact tracing with the exposure notification framework in the german corona-warn-app. In 2021 International Conference on Indoor Positioning and Indoor Navigation (IPIN) (pp. 1-8). IEEE.

Mohammadi, M., Vakilipour, S., and Ormiston, S. (2021). Newton linearization of the Navier–Stokes equations for flow computations using a fully coupled finite volume method. Applied Mathematics and Computation, 397, 125916.

Mohammed, A. M., Ariane, M., and Alexiadis, A. (2020). Using discrete multiphysics modelling to assess the effect of calcification on hemodynamic and mechanical deformation of aortic valve. ChemEngineering, 4(3), 48.

Moskowitz, W. B., and Ebeid, M. R. (2022). Percutaneous management of challenging complex resistive targets in interventional pediatric cardiology. In Debulking in Cardiovascular Interventions and Revascularization Strategies (pp. 805-907). Academic Press.

Nagpal, P., Agrawal, M. D., Saboo, S. S., Hedgire, S., Priya, S., and Steigner, M. L. (2020). Imaging of the aortic root on high-pitch non-gated and ECG-gated CT: awareness is the key!. Insights into Imaging, 11(1), 1-14.

Obrist, D., and Carrel, T. P. (2021). Commentary: Leaflet fluttering of bioprosthetic valve—Does it matter?. JTCVS Open, 6, 82-83.

Ogden RW. 1972 Large deformation isotropic elasticity-on the correlation of theoryand experiment for compressible rubberlike solids.Proc. R. Soc. Lond. A328, 567–583.

Ogden, R. W., Saccomandi, G., and Sgura, I. (2004). Fitting hyperelastic models to experimental data. Computational Mechanics, 34(6), 484-502.

Onah, O. T., Nnaji, I. A., and Nwankwo, A. M. (2022). Evaluation of axial velocity and wall pressure models for nozzle bench mark using computational fluid dynamics. GSC Advanced Engineering and Technology, 4(1), 012-024.

Ovcharenko, E. A., Klyshnikov, K. U., Vlad, A. R., Sizova, I. N., Kokov, A. N., Nushtaev, D. V., ... and Zhuravleva, I. U. (2014). Computer-aided design of the human aortic root. Computers in biology and medicine, 54, 109-115.

Park, G., Kim, C., Lee, M., and Choi, C. (2020). Building geometry simplification for improving mesh quality of numerical analysis model. Applied Sciences, 10(16), 5425.

Pawade, T., Sheth, T., Guzzetti, E., Dweck, M. R., and Clavel, M. A. (2019). Why and how

to measure aortic valve calcification in patients with aortic stenosis. JACC: Cardiovascular Imaging, 12(9), 1835-1848.

Peng, Y., Bi, L., Guo, Y., Feng, D., Fulham, M., and Kim, J. (2019, July). Deep multi-modality collaborative learning for distant metastases predication in PET-CT soft-tissue sarcoma studies. In 2019 41st Annual International Conference of the IEEE Engineering in Medicine and Biology Society (EMBC) (pp. 3658-3688). IEEE.

Pinotti, Marcos and Faria, Edna M. de. Critical flow regions in tissue artificial heart valve assessed by laser doppler anemometer in continuous flow. Journal of the Brazilian Society of Mechanical Sciences and Engineering [online]. 2006, v. 28, n. 3 [Accessed 13 January 2023], pp. 259-263. Available from: ¡https://doi.org/10.1590/S1678-58782006000300002¿. Epub 18 Aug 2006. ISSN 1806-3691. https://doi.org/10.1590/S1678-58782006000300002.

Poggio, P. (2014). THE ROLE OF VALVE INTERSTITIAL CELLS IN THE PATHOGENESIS OF CALCIFIC AORTIC VALVE DISEASE.

Poterucha, T. J., and Maurer, M. S. (2022). Too stiff but still got rhythm: left atrial myopathy and transthyretin cardiac amyloidosis. Cardiovascular Imaging, 15(1), 30-32.

Qin, T., Caballero, A., Mao, W., Barrett, B., Kamioka, N., Lerakis, S., and Sun, W. (2020). The role of stress concentration in calcified bicuspid aortic valve. Journal of the Royal Society Interface, 17(167), 20190893.

Rabkin, E., Aikawa, M., Stone, J. R., Fukumoto, Y., Libby, P., and Schoen, F. J. (2001). Activated interstitial myofibroblasts express catabolic enzymes and mediate matrix remodeling in myxomatous heart valves. Circulation, 104(21), 2525-2532.

Qiao, Y., Luo, K., and Fan, J. (2022). Component quantification of aortic blood flow energy loss using computational fluid-structure interaction hemodynamics. Computer Methods and Programs in Biomedicine, 221, 106826.

Rahman, M. M., Hasan, K., and Zhu, Z. (2022). Development of a One Equation Eddy Viscosity Model based on k-epsilon and RAS Turbulence Models. In AIAA SCITECH 2022 Forum (p. 0485).

Rassoli, A., Fatouraee, N., Guidoin, R., and Zhang, Z. (2020). Comparison of tensile properties of xenopericardium from three animal species and finite element analysis for bioprosthetic heart valve tissue. Artificial Organs, 44(3), 278-287.

Rassoli, A., Fatouraee, N., Guidoin, R., Zhang, Z., and Ravaghi, S. (2022). A comparative study of different tissue materials for bioprosthetic aortic valves using experimental assays and finite element analysis. Computer Methods and Programs in Biomedicine, 220, 106813.

Rathan, S., Ankeny, C. J., Arjunon, S., Ferdous, Z., Kumar, S., Fernandez Esmerats, J., ... and Jo, H. (2016). Identification of side-and shear-dependent microRNAs regulating porcine aortic valve pathogenesis. Scientific reports, 6(1), 1-16.

Reul Jr, G. J., Cooley, D. A., Duncan, J. M., Frazier, O. H., Hallman, G. L., Livesay, J. J., ... and Walker, W. E. (1985). Valve failure with the Ionescu-Shiley bovine pericardial bioprosthesis: analysis of 2680 patients. Journal of Vascular Surgery, 2(1), 192-204.

Reul, H., Vahlbruch, A., Giersiepen, M., Schmitz-Rode, T., Hirtz, V., and Effert, S. (1990). The geometry of the aortic root in health, at valve disease and after valve replacement. J. Biomech. 23, 181–191. doi: 10.1016/0021-9290(90)90351-3

Ross D. Homograft replacement of the aortic valve. Br J Surg 1967; 54:842–845.

Sacks, M. S., and Chuong, C. J. (1998). Orthotropic mechanical properties of chemically treated bovine pericardium. Annals of biomedical engineering, 26, 892-902.

Sacks MS, Schoen FJ. Collagen fiber disruption occurs independent of calcification in clinically explanted bioprosthetic heart valves. J Biomed Mater Res. 2002 Dec 5;62(3):359-71. doi: 10.1002/jbm.10293. PMID: 12209921.

Schaefer, A. K., Andreas, M., Werner, P., Sassi, C. G., Haberl, T., Kocher, A., ... and Russo, M. (2019). Excessive pannus overgrowth on the aortic side of Trifecta valve causing severe regurgitation. The Annals of thoracic surgery, 108(2), e87-e89.

SCHNEIDER, P. J., and DECK, J. D. (1981). Tissue and cell renewal in the natural aortic valve of rats: an autoradiographic study. Cardiovascular Research, 15(4), 181-189.

Schoen, F. J., and Levy, R. J. (1999). Tissue heart valves: current challenges and future research perspectives. Journal of Biomedical Materials Research: An Official Journal of The Society for Biomaterials, The Japanese Society for Biomaterials, and The Australian Society for Biomaterials and the Korean Society for Biomaterials, 47(4), 439-465.

Schoen, F. J. Evolving concepts of cardiac valve dynamics: the continuum of development, functional structure, pathobiology, and tissue engineering. Circulation 118, 1864–1880 (2008).

Sellers, S. L., Blanke, P., and Leipsic, J. A. (2019). Bioprosthetic heart valve degeneration and dysfunction: Focus on mechanisms and multidisciplinary imaging considerations. Radiology: Cardiothoracic Imaging, 1(3), e190004.

Sellers, S. L., Gulsin, G. S., Zaminski, D., Bing, R., Latib, A., Sathananthan, J., ... and Bouchareb, R. (2021). Platelets: implications in aortic valve stenosis and bioprosthetic valve dysfunction from pathophysiology to clinical care. Basic to Translational Science, 6(12), 1007-1020.

Sénage, T., Le Tourneau, T., Foucher, Y., Pattier, S., Cueff, C., Michel, M., ... and Roussel, J. C. (2014). Early structural valve deterioration of Mitroflow aortic bioprosthesis: mode, incidence, and impact on outcome in a large cohort of patients. Circulation, 130(23), 2012-2020.

Shabbir, S., Satyanarayana, B., and Sreeramulu, K. (2020). Characterization of hyperelastic material by experimental tests and curve fitting. Materials Today: Proceedings, 24, 1670-1679.

Shan, Y., Li, J., Wang, Y., Wu, B., Barker, A. J., Markl, M., ... and Shu, X. (2017). Aortic shear stress in patients with bicuspid aortic valve with stenosis and insufficiency. The Journal of thoracic and cardiovascular surgery, 153(6), 1263-1272.

Juliana Martins de S. e Silva. Three-dimensional non-destructive soft-tissue visualization with X-ray staining micro-tomography.

Song, R., Fullerton, D. A., Ao, L., Zhao, K. S., and Meng, X. (2017). An epigenetic regulatory loop controls pro-osteogenic activation by TGF-1 or bone morphogenetic protein 2 in human aortic valve interstitial cells. Journal of Biological Chemistry, 292(21), 8657-8666.

Spadaccio, C., Mazzocchi, L., Timofeva, I., Macron, L., De Cecco, C. N., Morganti, S., ... and Nappi, F. (2020). Bioengineering case study to evaluate complications of adverse anatomy of aortic root in transcatheter aortic valve replacement: combining biomechanical modelling with CT imaging. Bioengineering, 7(4), 121.

Stalder AF, Frydrychowicz A, Russe MF, Korvink JG, Hennig J, Li K, Markl M. Assessment of flow instabilities in the healthy aorta using flow-sensitive MRI. J Magn Reson Imaging. 2011 Apr;33(4):839-46.

Stanger, O. H. (2019). Challenges and lessons from preoccupation with the stentless aortic valve prosthesis concept. Surgical Management of Aortic Pathology: Current Fundamentals for the Clinical Management of Aortic Disease, 699-717.

Stanová, V., Godio Raboutet, Y., Barragan, P., Thollon, L., Pibarot, P., and Rieu, R. (2022). Leaflet stress quantification of porcine vs bovine surgical bioprostheses: an in vitro study. Computer Methods in Biomechanics and Biomedical Engineering, 25(1), 40-51.

Stein, P.D., and Sabbah, H.N. (1976). Turbulent Blood Flow in the Ascending Aorta of Humans with Normal and Diseased Aortic Valves. Circulation Research, 39, 58–65.

Sturla, F., Piatti, F., Jaworek, M., Lucherini, F., Pluchinotta, F. R., Siryk, S. V., ... and Lombardi, M. (2020). 4D Flow MRI hemodynamic benchmarking of surgical bioprosthetic valves. Magnetic Resonance Imaging, 68, 18-29.

Suh, Y. J., Kim, Y. J., Hong, Y. J., Lee, H. J., Hur, J., Im, D. J., ... and Choi, B. W. (2015). Measurement of opening and closing angles of aortic valve prostheses in vivo using dual-source computed tomography: comparison with those of manufacturers' in 10 different types. Korean journal of radiology, 16(5), 1012-1023.

Sun, W., Sacks, M. S., Sellaro, T. L., Slaughter, W. S., and Scott, M. J. (2003). Biaxial mechanical response of bioprosthetic heart valve biomaterials to high in-plane shear. J. Biomech. Eng., 125(3), 372-380.

Sun, W., and Sacks, M. S. (2005). Finite element implementation of a generalized Fung-elastic constitutive model for planar soft tissues. Biomechanics and modeling in mechanobiology, 4, 190-199.

Sutton III, J. P., Ho, S. Y., and Anderson, R. H. (1995). The forgotten interleaflet triangles: a review of the surgical anatomy of the aortic valve. The Annals of thoracic surgery, 59(2), 419-427.

Tagliari, F., Correia, M. G., Amorim, G. D., Colafranceschi, A. S., Pedroso, J. M., Rodrigues Junior, L. F., ... and Lamas, C. (2022). Clinical Features and Survival Analysis of Patients after Mechanical Heart Valve Replacement, with an Emphasis on Prosthetic Valve Thrombosis. Arquivos Brasileiros de Cardiologia, 119, 734-744.

Tan, T. S., Akbulut, I. M., Kozluca, V., Durdu, M. S., and Dincer, I. (2021). Severe intermittent transvalvular mitral valve regurgitation: serious complication of mitral valve replacement with subvalvular preservation. Case Reports, 3(4), 663-667.

Taylor, P. M., Batten, P., Brand, N. J., Thomas, P. S., and Yacoub, M. H. (2003). The cardiac valve interstitial cell. The international journal of biochemistry and cell biology, 35(2), 113-118.

Teng, P., Xu, X., Ni, C., Yan, H., Sun, Q., Zhang, E., and Ni, Y. (2020). Identification of key genes in calcific aortic valve disease by integrated bioinformatics analysis. Medicine, 99(29).

Ulloa, L. S., Perissinotto, F., Rago, I., Goldoni, A., Santoro, R., Pesce, M., ... and Scaini, D. (2021). Carbon nanotubes substrates alleviate pro-calcific evolution in porcine valve interstitial cells. Nanomaterials, 11(10), 2724.

Unger, P., and Tribouilloy, C. (2020). Aortic stenosis with other concomitant valvular disease: aortic regurgitation, mitral regurgitation, mitral stenosis, or tricuspid regurgitation. Cardiology clinics, 38(1), 33-46.

Vadana, M., Cecoltan, S., Ciortan, L., Macarie, R. D., Tucureanu, M. M., Mihaila, A. C., ... and Manduteanu, I. (2020). Molecular mechanisms involved in high glucose-induced valve calcification in a 3D valve model with human valvular cells. Journal of Cellular and Molecular Medicine, 24(11), 6350-6361.

Vesely, I. (2003). The evolution of bioprosthetic heart valve design and its impact on durability. Cardiovascular Pathology, 12(5), 277-286.

Weese, J., Lungu, A., Peters, J., Weber, F. M., Waechter-Stehle, I., and Hose, D. R. (2017). CFD-and Bernoulli-based pressure drop estimates: a comparison using patient anatomies from heart and aortic valve segmentation of CT images. Medical physics, 44(6), 2281-2292.

Weind KL, Ellis CG, Boughner DR. The aortic valve blood supply. J Heart Valve Dis. 2000 Jan;9(1):1-7; discussion 7-8. PMID: 10678369.

Wells, S. M., and Sacks, M. S. (2002). Effects of fixation pressure on the biaxial mechanical behavior of porcine bioprosthetic heart valves with long-term cyclic loading. Biomaterials, 23(11), 2389-2399.

Werner P, Gritsch J, Scherzer S, Gross C, Russo M, Coti I et al. Structural valve deterioration after aortic valve replacement with the Trifecta valve. Interact CardioVasc Thorac Surg 2020; doi:10.1093/icvts/ivaa236.

Whelan, A., Williams, E., Nolan, D. R., Murphy, B., Gunning, P. S., O'Reilly, D., and Lally, C. (2021). Bovine pericardium of high fibre dispersion has high fatigue life and increased collagen

content; potentially an untapped source of heart valve leaflet tissue. Annals of Biomedical Engineering, 49(3), 1022-1032.

Wilber, J. P., and Walton, J. R. (2002). The convexity properties of a class of constitutive models for biological soft issues. Mathematics and Mechanics of Solids, 7(3), 217-235.

Wilson, W. R., Gewitz, M., Lockhart, P. B., Bolger, A. F., DeSimone, D. C., Kazi, D. S., ... and Baddour, L. M. (2021). Prevention of viridans group streptococcal infective endocarditis: a scientific statement from the American Heart Association. Circulation, 143(20), e963-e978.

Wright, B. E., Watson, G. L., and Selfridge, N. J. (2020). The Wright table of the cardiac cycle: a stand-alone supplement to the Wiggers diagram. Advances in Physiology Education, 44(4), 554-563.

Wu, M. C., Zakerzadeh, R., Kamensky, D., Kiendl, J., Sacks, M. S., and Hsu, M. C. (2018). An anisotropic constitutive model for immersogeometric fluid–structure interaction analysis of bioprosthetic heart valves. Journal of biomechanics, 74, 23-31.

Xiong, T., Han, S., Pu, L., Zhang, T. C., Zhan, X., Fu, T., ... and Li, Y. X. (2022). Bioinformatics and machine learning methods to identify FN1 as a novel biomarker of aortic valve calcification. Frontiers in Cardiovascular Medicine, 9.

Xu, F., Johnson, E. L., Wang, C., Jafari, A., Yang, C. H., Sacks, M. S., ... and Hsu, M. C. (2021). Computational investigation of left ventricular hemodynamics following bioprosthetic aortic and mitral valve replacement. Mechanics Research Communications, 112, 103604.

Yang, P., Troncone, L., Augur, Z. M., Kim, S. S., McNeil, M. E., and Paul, B. Y. (2020). The role of bone morphogenetic protein signaling in vascular calcification. Bone, 141, 115542.

Yap, C. H., Saikrishnan, N., Tamilselvan, G., and Yoganathan, A. P. (2012). Experimental measurement of dynamic fluid shear stress on the aortic surface of the aortic valve leaflet. Biomechanics and modeling in mechanobiology, 11, 171-182.

Yongue, C., Lopez, D. C., Soltesz, E. G., Roselli, E. E., Bakaeen, F. G., Gillinov, A. M., ... and Johnston, D. R. (2021). Durability and performance of 2298 Trifecta aortic valve prostheses: a propensity-matched analysis. The Annals of Thoracic Surgery, 111(4), 1198-1205.

Youssefi, P., El-Hamamsy, I., and Lansac, E. (2019). Rationale for aortic annuloplasty to standardise aortic valve repair. Annals of cardiothoracic surgery, 8(3), 322.

Yu, T., Yang, W., Zhuang, W., Tian, Y., Kong, Q., Chen, X., ... and Wang, Y. (2021). A bioprosthetic heart valve cross-linked by a non-glutaraldehyde reagent with improved biocompatibility, endothelialization, anti-coagulation and anti-calcification properties. Journal of Materials Chemistry B, 9(19), 4031-4038.

Zhang, S., Zhao, X., and Bayyuk, S. (2014). Generalized formulations for the Rhie–Chow interpolation. Journal of Computational Physics, 258, 880-914.

Zhou, L., Liu, Z., Shou, X., Yang, L., Wang, L., and Xiong, Z. (2022, August). Mechanical-electrical Coupling Analysis of Vertical Cage Antenna Electrical Performance under Multi-wind Direction Wind Loads. In 2022 IEEE 5th International Conference on Electronic Information and Communication Technology (ICEICT) (pp. 931-933). IEEE.

Appendix A

Abbreviations

Aortic Root	AR
Aortic Valve	AV
Aortic Valve Replacement	AVR
Arbitrarily Lagrangian-Eulerian	ALE
Ascending Aorta	AAo
Biological Heart Valve	BHV
Bone Morphogenetic Protein	BMP
Computed Axial Tomography	CAT
Computed Fluid Dynamics	CFD
Computed Tomography	CT
Extra Cellular Matrix	ECM
Finite Element Analysis	FEA
Finite Volume Method	FVM
Fluid-Structural Interaction	FSI
Food and Drug Administration	FDA
Glycosaminoglycans	GAGs
Laser Doppler Anemometer	LDA
Left Coronary	LC
Left Ventricular Outlet Tract	LVOT
Major Histocompatibility Complex	MHC
Matrix Gla Protein	MGP
Non-Coronary	NC
Phospho-Buffer Saline	PBS
Preferred-fiber Direction	PD
Pressure-Implicit with Splitting of Operators	PISO
Prosthesis-Patient Mismatch	PPM
Residual Sum of Squares	RSS
Reynolds Number	Re
Reynolds-Averaged Navier-Stokes	RANS
Right Coronary	RC
Semi-Implicit Method for Pressure-Linked Equations	SIMPLE
Shear Stress Transport	SST

Small Angle Light Scattering	SALS
Smooth Muscle Cell	SMC
Structural Valve Degeneration	SVD
Transcatheter Aortic Valve Implant	TAVI
Valve Endothelial Cells	VECs
Valve Interstitial Cells	VICs
Wall Shear Stress	WSS